Calibration of the E and B EXperiment (EBEX), A Balloon-Borne Cosmic Microwave Background Polarimeter

A DISSERTATION
SUBMITTED TO THE FACULTY OF THE GRADUATE SCHOOL
OF THE UNIVERSITY OF MINNESOTA
BY

Daniel Edward Polsgrove

IN PARTIAL FULFILLMENT OF THE REQUIREMENTS
FOR THE DEGREE OF
DOCTOR OF PHILOSOPHY

Professor Terry J. Jones

September, 2009

Acknowledgements

The number of individuals who deserve mention on this page far exceeds the space available. Amongst those who have gone far above and beyond the call of duty, I'd like to thank my advisor, Terry Jones, and my unofficial but functional co-advisor, Shaul Hanany. Their influence on my education is rivaled only by the positive impact they've had on my character, personality, and perspective. They have provided an invaluable demonstration of how to work hard, persevere through the unrelenting challenges and frustrations inherent to experimental astrophysics, and at the same time keep those things of most importance at the top of the priority list.

At the top of that list for me is my wife Kelly. There's simply no chance of listing all she's done to keep me (us) afloat over the past 3 years. I am and will be forever grateful. At least if there's ever an opportunity for one of us to go on a 3-year deployment to Mars, we now know we can handle it.

I'd also like to acknowledge each member of the EBEX collaboration – it's been a true pleasure getting to know and work with such a fantastic group of people. Although I have great appreciation for everyone listed in Appendix B, I must highlight my UMN cosmolab companions – Asad Aboobaker, Chaoyun Bao, Hannes Hubmayr, Jeff Klein, Michael Milligan, Kate Raach, Ilan Sagiv, and Kyle Zilic. Each has played a unique and significant role in my journey and this document would probably be about half its current length without their contributions. I must also make special mention of my fellow veterans of the NA test flight campaign – their camaraderie is without a doubt the only reason I survived Ft Sumner (well, that and Catfish Friday at the Hamburger Stand).

Finally, I must thank the US Air Force Academy and Air Force Institute of Technology for the financial and administrative support that made this experience possible.

Dedication

To the one true God and His Son Jesus Christ; “For since the creation of the world God’s invisible qualities – his eternal power and divine nature – have been clearly seen, being understood from what has been made, so that men are without excuse”. *Romans 1:20*

Abstract

We discuss pre-flight calibration of the E and B EXperiment (EBEX), a balloon-borne telescope designed to measure the B-mode polarization anisotropy of the cosmic microwave background (CMB). EBEX will observe the sky with 8' resolution in each of three bands centered on 150, 250 and 410 GHz. Employing over 1,400 detectors and performing polarimetry through a continuously rotating half-wave plate with fixed wire-grid polarizer, we expect to detect the B-mode signal or set a new upper limit one order of magnitude below the current value. In this thesis we describe a set of ground-based experiments devised for calibrating instrumental response to incident millimeter-wave flux with varying spectral and polarization properties. We chronicle the design, construction and execution of these experiments, along with preliminary results from tests executed prior to our North American (NA) test flight which originated at the Columbia Scientific Ballooning Facility, Ft Sumner, NM in June 2009. A brief review of this inaugural flight is provided, as is a synopsis of our current plan for a comprehensive calibration strategy to be implemented in conjunction with a future long duration balloon (LDB) flight over Antarctica.

Table of Contents

List of Tables

List of Figures

1 Cosmology and the Polarization of the Cosmic Microwave Background

1.1 Introduction

The quest for understanding the origin, evolution, and fate of the Universe likely began soon after the first set of human eyes surveyed the night sky. Over the intervening millennia, a wide variety of cosmological models have passed in and out of vogue. Astrophysical data collected over the past half-century point toward a Universe dominated by dark energy (Λ) and cold dark matter (CDM), had a finite beginning ~14 billion years ago, and is in a current state of accelerated expansion [1,2]. With these data in hand, the scientific community of the 21st century is in nearly unanimous support of the inflationary ΛCDM Big Bang model. The prefix 'inflationary' is a relatively recent amendment to the standard Big Bang model and implies a period of exponential expansion hypothesized to have occurred around the time the Universe reached ~10^{-35} seconds of age. Initially proposed almost 30 years ago, inflation solves the monopole, horizon, and flatness problems which plagued the standard model [3,4,5,6]. Inflation also makes predictions about the statistical nature of the Universe which have proven consistent with all observations. However, there exists no direct confirmation of the inflationary paradigm, and many details remain uncertain.

A number of projects currently in operation and under construction are designed to search for empirical evidence of inflation, and many have focused their efforts on the inflationary gravity wave background (IGB). The IGB is a stochastic background of gravitational waves predicted by many inflation models [7,8,9,10,11]. Technology is being developed to make a direct detection of these gravity waves, but pathfinder projects in operation today are seemingly well short of achieving the requisite sensitivity. However, theory posits that the IGB left an indelible mark on the cosmic microwave background (CMB), a signature that may be within reach using millimeter- and sub-millimeter wave telescopes scheduled for deployment over the coming decade.

1.2 The Cosmic Microwave Background

Emerging ~ 400,000 years after the Big Bang but first detected in 1965, the CMB is a bath of photons originally released as the temperature of the Universe slipped below the ionization energy of the Hydrogen atom. Also known as the surface of last scattering, the CMB provides a snapshot of the Universe at a redshift of z ~1100 when photons for the first time were free to travel the cosmos unimpeded by frequent interactions with electrons. A tiny fraction of these photons have been intercepted by ground-, balloon-, and space-based telescopes over recent years, revealing the CMB as the most perfect blackbody ever discovered (Fig. 1.1) [12,13]. Its temperature across the entire sky is a nearly constant 2.725˚ K, disrupted only by variations at the level of 10^{-5}. However, these miniscule variations, or anisotropies, have revealed much more about the Universe than has been learned from the CMB emission spectrum alone.

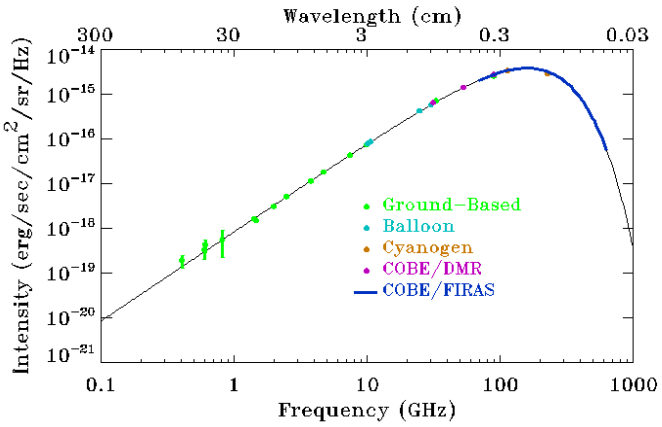

Figure 1.1: A compilation of CMB temperature data from ground-, balloon-, and space-based observations. (Credit: NASA/ARCADE Science Team)

Spherical harmonics are a convenient mathematical tool for representing CMB temperature anisotropy data. After maps are made charting temperature as a function of sky position, the data are decomposed with

$$\frac{\Delta T(\theta,\phi)}{T_0} = \sum_{l-0}^{\infty} \sum_{m=-l}^{l} a_{lm} Y_{lm}(\theta,\phi) \qquad (1.1)$$

where T_0 is the average signal over the entire sky and the a_{lm}'s contain the information of most interest – temperature deviation as a function of angular scale on the sky. Averaging the a_{lm}'s over many realizations gives us the multipole moments C_l using

$$C_l = \left\langle |a_{lm}|^2 \right\rangle = \frac{1}{2l+1} \sum_m |a_{lm}|^2 \tag{1.2}$$

which serves as the basis for plotting the temperature auto-correlation, or TT, angular power spectrum. As shown in Fig. 1.2, the TT spectrum contains a main peak at l ~ 200 (~ 1˚ on the sky), followed by several more peaks of waning magnitude at higher multipoles. The theory explaining these features is robust: having an energy density greater than the binding energy of Hydrogen over the first 400,000 years of its existence, the Universe was dominated by a plasma of free electrons and protons. Photons at this time experienced nearly constant scattering off the free electrons, creating a cosmological fluid and rendering the Universe virtually opaque. Bulk movement of this fluid was driven by a non-uniform gravitational potential field, seeded by quantum fluctuations arising shortly after the Big Bang itself. The fluid's response to peaks and valleys in the field caused standing waves of varying magnitude at different physical scales. The scale with the greatest amplitude at a particular epoch was the one corresponding to the comoving size of the sound-crossing horizon at that epoch. When scattering for the last time off free electrons, photons carried away with them an imprint of the scale(s) with greatest amplitude (temperature anisotropy) at the epoch of recombination. This imprint is clearly seen as the largest spike in the TT spectrum, referred to as the first acoustic peak, as it reveals the size the comoving size of the sound horizon (~300 Mpc) at z ~ 1100.

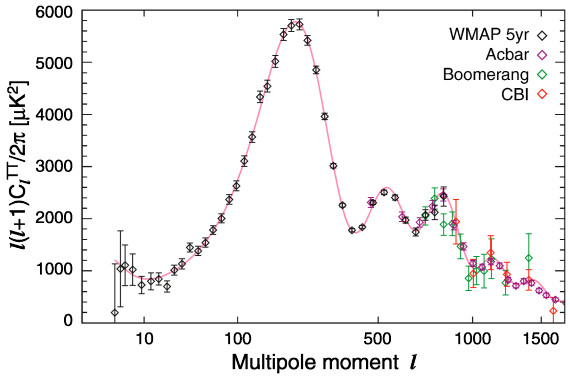

Figure 1.2: CMB temperature auto-correlation angular power spectrum (TT). Solid red line is theoretical model assuming inflationary ΛCDM cosmology; data at large angular scales are derived from 5-year WMAP observations [1], and at small scales from observations by ground-based (Acbar, CBI) and balloon-borne (Boomerang) instruments. (Credit: NASA/WMAP Science Team)

1.3 Polarization of the CMB

Having confirmed the existence of temperature anisotropies as anticipated given the scenario of last scattering, theory immediately predicts the presence another signal in the CMB: linear polarization. An individual electron in the cosmological fluid moving toward or away from a density perturbation will observe a quadrupole radiation field [14]. Photons scattered by this electron (Thomson scattering) will be linearly polarized at a fraction proportional to the magnitude of the field's anisotropy. Whereas the scientific community typically views and reports linear polarization in terms of the Stokes parameters Q and U, cosmologists employ a platform-independent convention that decomposes CMB polarization into two mathematically orthogonal components: a curl-free component and a divergence-free component. Inspired by terminology used in electromagnetism, the label E-modes is used to indicate the curl-free component and B-modes refers to the divergence-free component.

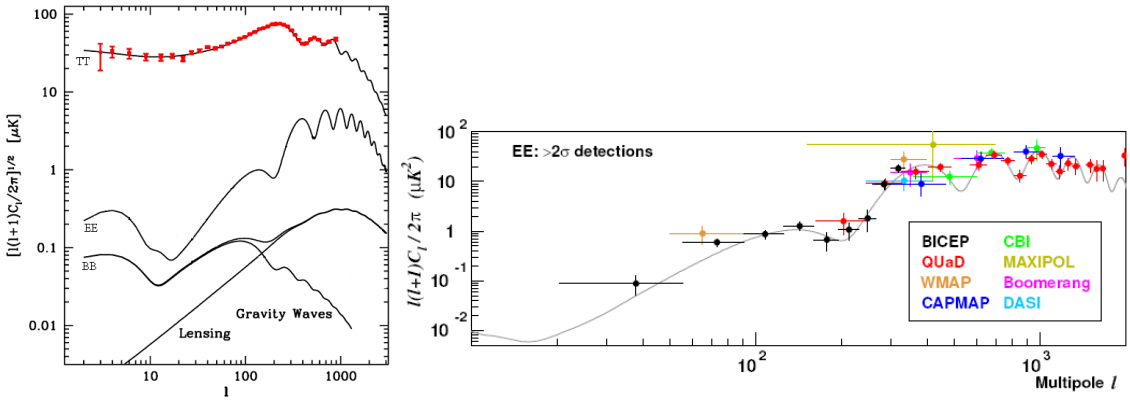

Figure 1.3: Left - Temperature and polarization auto-correlation spectra predicted by ΛCDM model (solid black lines). Red TT data points are from WMAP alone, identical to black diamonds shown in Fig. 1.2. Gravity wave component of BB model assumes $r = 0.1$ (Credit: EBEX Science Team). Below: E-mode spectrum as measured through ground-based (BICEP, Quad, CAPMAP, CBI, DASI), balloon-borne (MAXIPOL, Boomerang) and space-based (WMAP) observations. (Credit: BICEP Science Team)

The E-mode auto-correlation, or EE spectrum, is developed through a pipeline similar in most ways to that used in deriving the TT spectrum. Before the first observation of CMB polarization was ever made, the EE spectrum was robustly predicted to include peaks above l ~100 with ~10x lower amplitude and out of phase with the TT spectrum as shown in Fig. 1.3. It is also important to note that polarization from electrons moving in response to perturbations in the

gravitational potential field (scalar perturbations) can *only* generate E-modes [14]. As shown in the lower panel of Fig. 1.3, E-modes have recently been detected by a number of experiments and are consistent with theoretical expectations assuming the ΛCDM model.

Theory predicts two mechanisms capable of producing B-modes as indicated in the figure above: the IGB (dominant at large angular scales), and gravitational lensing of E-modes (dominant at smaller angular scales). Given the EE spectrum, B-modes are robustly predicted to exist at small angular scales from the gravitational lensing of E-modes by large scale structure (galaxy clusters) [16,17]. Detection of the lensing B-mode signal seems assured once sufficient instrument sensitivity is achieved [18,19]. The gravity wave signal is a different story; its magnitude remains unknown to within 12 orders of magnitude and even with the most optimistic assumptions resides another order of magnitude below the E-mode spectrum as depicted in Fig. 1.3.

A useful convention exists to compare energy in primordial density (scalar) perturbations and gravity wave (tensor) perturbations. The relation is based on their temperature quadrupoles (C_2^{GW}/C_2^{S}) and known as the tensor-to-scalar ratio, labeled *T/S* or *r*. The value of *r* depends directly on the epoch at which inflation occurred, which is in turn directly related to the energy scale of inflation. The equation $V^{1/4} = 3.7 \times 10^{16}\, r^{1/4}$ GeV relates the energy scale of inflation ($V^{1/4}$) and the tensor-to-scalar ratio. Although *r* and $V^{1/4}$ are largely unconstrained at this point, popular 'simple' models of inflation predict $T/S \sim 0.1$ [20]. At the present, astrophysical data have set a 2σ upper limit of $r < 0.22$, giving $V^{1/4} < 2.5 \times 10^{16}$ GeV [1]. Another relationship exists that allows the energy scale of inflation to be extracted directly from the BB spectrum: $V^{1/4} = 2 \times 10^{16}\, (B_{peak}/0.1\ \mu K)^{1/2}$ GeV, where B_{peak} is the value of the B-mode peak at l=90 (in μK). A B-mode detection at l <150 would provide direct observational evidence of inflation. But as Fig. 1.4 reveals, no CMB experiment to date has achieved the sensitivity required to accomplish this task.

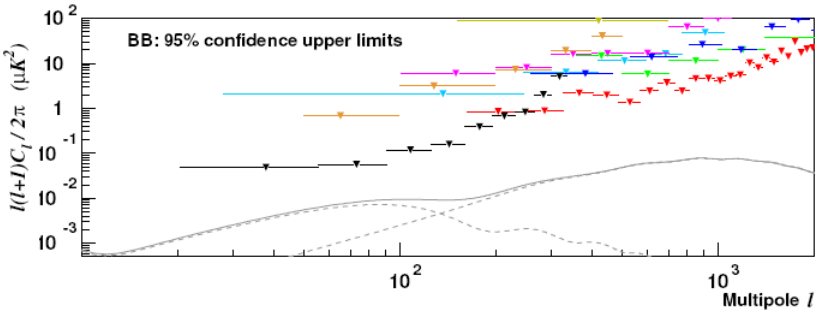

Figure 1.4: Upper limits on B-modes from recent CMB measurements. Colors correspond to the same experiments listed in Fig. 1.3. (Credit: BICEP Science Team)

This thesis is centered on the E and B EXperiment (EBEX), a balloon-borne polarimeter designed to probe the polarization of the CMB with unprecedented sensitivity. Chapter 2 provides the goals of EBEX and an overview of the instrument. Chapter 3 summarizes the calibration strategy, including benchmarks required to achieve our target sensitivity as well as a description of critical hardware components developed specially for characterizing the instrument. The ground-based experiments introduced in Chapter 3 are expounded on in Chapter 4, where we also report preliminary results gained by executing a majority of these experiments in the spring of 2009 prior to the North American (NA) test flight. Chapter 5 offers a brief synopsis of the NA test flight and reviews key calibration issues to be addressed in preparation for the planned long duration balloon (LDB) flight.

2 The E and B EXperiment

The EBEX collaboration began in 2004 and today includes over 40 members (Appendix B). Collecting mm- and sub-mm-wave light in three frequency bands near the peak of the CMB spectrum, the EBEX telescope exploits a combination of well-tested and novel features to attain high sensitivity and prodigious systematic error mitigation. The project is intended to culminate with a 14-day science flight over Antarctica. The proceeding discussion outlines the science goals of EBEX and provides an overview of the instrument being assembled to achieve those goals.

2.1 Science Goals

EBEX has four primary science goals:

1. Detect the inflationary B-mode signal in the CMB polarization, or set a new upper limit on the energy scale of inflation that is an order of magnitude more stringent than the current constraint.
2. Discover the robustly predicted yet still undetected weak gravitational lensing B-mode signal.
3. Characterize the polarized dust emission and determine its angular power spectra in both E- and B- mode polarizations.
4. Improve constraints on various cosmological parameters by making a cosmic-variance-limited measurement of the CMB E-mode power spectrum.

As stated in Chapter 1, the current upper limit on the energy scale of inflation is 2.5×10^{16} GeV ($T/S < 0.2$). This bound is ascertained from CMB, baryon acoustic oscillation, and supernovae data, and is a factor of two higher than the approximate lower limit predicted by *classic* inflationary models (ref). If T/S is indeed close to 0.1 and EBEX meets all performance specifications, we will make a high signal-to-noise ratio (S/N) detection of the IGB B-mode signal in the multipole moment range $20 < l < 150$. If T/S is significantly lower than 0.1, EBEX will establish a new 2σ upper limit of 0.02 which would lower the current bound by a factor of 10 and have conspicuous theoretical repercussions. Figure 2.1 captures our goals and expectations

for EBEX, and also highlights the challenges that nature imposes on the next generation of CMB polarimeters in search of the IGB signal.

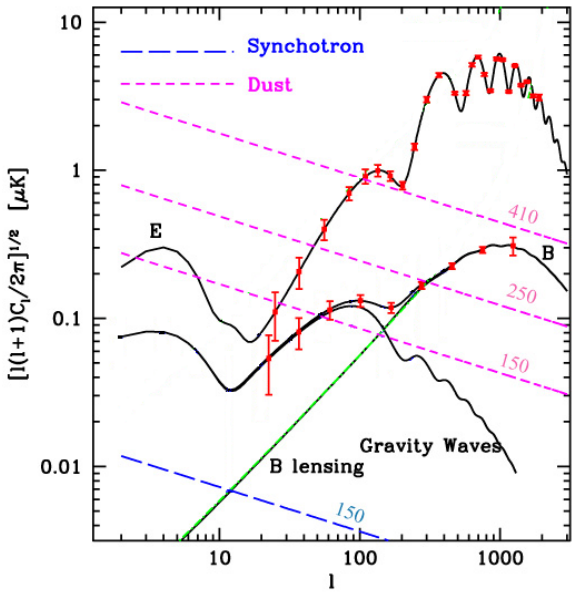

Figure 2.1: Solid black lines are theoretical E- and B-mode auto-correlation spectra, identical to those shown in Fig. 1.3. Red data points represent expected EBEX results (with 1σ error bars) assuming a 14-day flight. Dashed pink and blue lines are expected dust and synchrotron BB spectra (respectively) at the frequencies listed (in GHz) assuming the LDB scan region, extrapolated from WMAP observations [21].

Regardless of the energy scale of inflation or existence of the IGB, EBEX should make a high S/N detection of the lensing B-mode spectrum. As Fig. 2.1 illustrates, the lensing spectrum dominates the IGB at *l*'s above 200, and the model shown is predicted with approximately 20% uncertainty [18,19]. If detected where predicted, the lensing signal will provide a consistency check for other results. A non-detection would be even more significant as it would undermine confidence in the currently accepted cosmological model.

The third goal is to make an accurate determination of polarized dust foregrounds. Little data in the frequency range of interest for CMB polarimetry currently exists (especially at high galactic latitudes), and although theoretical predictions about foregrounds are available, surprising deviations between theory and reality have been reported at other wavelengths [22]. This goal is of critical importance because the dust B-mode is expected to be nearly as strong as the IGB signal at 150 GHz for $r = 0.1$ (and stronger in the case of 250 and 410 GHz bands) [21]. As such, we must characterize and subtract the foreground dust signal to have any hope of

extracting the inflationary B-modes. Characterizing dust is not only imperative for EBEX, it is necessary for any and all future B-mode experiments. Therefore, the polarized foreground information gathered during the EBEX LDB flight will provide the community with data crucial to the success of future missions.

We also anticipate making a high S/N determination of the EE spectrum. Taken alongside our expected TT and lensing BB results, the EBEX E-mode data should promote a factor of two improvement on various cosmological parameters including the density of dark energy (Ω_Λ), total matter density ($\Omega_m h^2$), baryonic matter density ($\Omega_b h^2$), the Hubble constant, the slope of the primordial density fluctuations spectrum, and the running of the spectral index.

2.2 Instrument Description

EBEX is designed to detect B-mode polarization using a large number of detectors over a long integration time, mitigating systematic errors through the use of half wave plate (HWP) polarimetry, observing a low dust emission region of the sky, and performing accurate foreground discrimination. Operating at an altitude of 120,000 feet, atmospheric emission is decreased by more than two orders of magnitude compared to observing from the ground, and allows for observation at frequencies unavailable from the surface due to atmospheric absorption. During the LDB flight, EBEX will cover a 420 deg^2 patch of sky at high galactic latitudes, revisiting most pixels in that patch over 10 million times. Accepting incident radiation over much of the spectrum between 133 and 450 GHz, EBEX delivers the widest frequency range of any past, present or proposed suborbital CMB experiment. A broad range of frequencies provides a strong lever arm on making an accurate determination (and subtraction) of the polarized dust emission spectrum.

2.2.1 Optics

Light is collected with an f/1.7 Gregorian Dragone telescope which includes a 1.5 m primary mirror and 1 m ellipsoidal secondary. After reflecting off the primary and secondary, light enters the cryostat where it encounters several lenses, filters, a rotating HWP, wire-grid polarizer, conical feed horns and waveguides before arriving at the focal planes. The beams generated by this optical system are independent of wavelength and predicted to be Gaussian with 8’ FWHM

for each bolometer. The mirrors, cryostat, and associated electronics are mounted on the gondola. The gondola and associated attitude control system (ACS) is responsible for pointing control, employing several moving parts (pivot and flywheel for azimuth control, linear actuator for elevation control) and a variety of complementary sensors (star camera, sun sensor, magnetometer, gyroscopes, GPS). The optical design is optimized to focus light onto approximately 1400 detectors spread over two orthogonal focal planes. A gold-plated conical feed horn and waveguide are mounted just above each detector; the waveguide geometry serves as a high-pass filter and determines the low end cutoff for each of our three bands. A pair of metal-mesh low-pass filters is mounted in front of the feed horn arrays to define the high end cutoff. These elements define the spectral response of the instrument, fiducially spanning 133-173 GHz (the '150 GHz' band), 217-288 GHz (the '250 GHz' band) and 355-450 GHz (the '410 GHz' band).

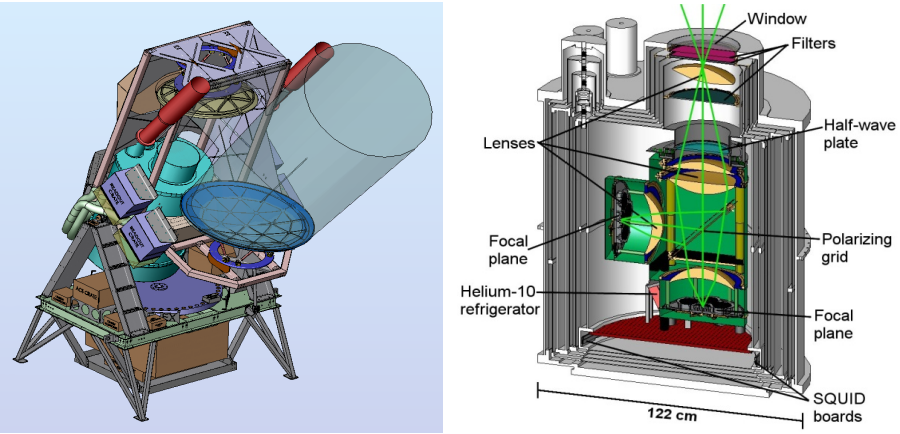

Figure 2.2: Left - Partial schematic diagram of EBEX gondola highlighting the path light takes from primary mirror (dark blue) to secondary mirror (beige) and finally into the cryostat (turquoise). Star cameras (used for pointing reconstruction) shown in red. Various electronics crates, paneling and baffles are excluded in this view. Right - Cutaway view of EBEX cryostat in LDB configuration.

2.2.2 Polarimetry

EBEX measures the polarization of incident radiation with a rotating HWP and fixed wire-grid polarizer, a technique with strong heritage in experimental astrophysics [23,24]. This strategy was first employed for CMB observations by the MAXIPOL experiment [25] and the basic principle is illustrated in Figure 2.3. The HWP is made of a birefringent material which has

different indices of refraction (n) along its two axes, labeled ordinary [o] and extraordinary [e]. The HWP is an inherently monochromatic device; the wavelength at which it works is entirely defined by the thickness of the material. Between entering and exiting the device, an incident electromagnetic wave of the appropriate wavelength oriented parallel to the o (e) axis will experience a $\pi/2$ phase delay relative to an incident wave arriving parallel to the e (o) axis assuming $n_o > (<) n_e$. If the incident light is completely unpolarized, the HWP has no net effect. If the incident light is fully polarized, the HWP will rotate the orientation of the output polarization vector relative to the input vector by 2α, where α represents the angle between the incident vector and the o (e) axis. If the HWP is rotating while illuminated by polarized light with a fixed incident polarization vector, the output polarization will rotate twice for each single revolution of the HWP. Given that polarization is a spin-2 tensor (redundant at orientations separated by 180˚), placing a polarizing grid after the HWP followed by a detector generates a sinusoidal signal with a frequency 4 times the HWP rotation rate ($f_{detector\ signal} = 4f_{hwp}$). If multiple detectors populate a focal plane behind a HWP/grid system as is the case for EBEX, each detector makes an independent measurement of the incident Stokes parameters. This configuration offers an advantage over alternative approaches where Q and U are measured by separate detectors - e.g., polarization sensitive bolometers (PSBs) – because PSBs are susceptible to systematic effects that can only be overcome with high precision inter-detector calibration.

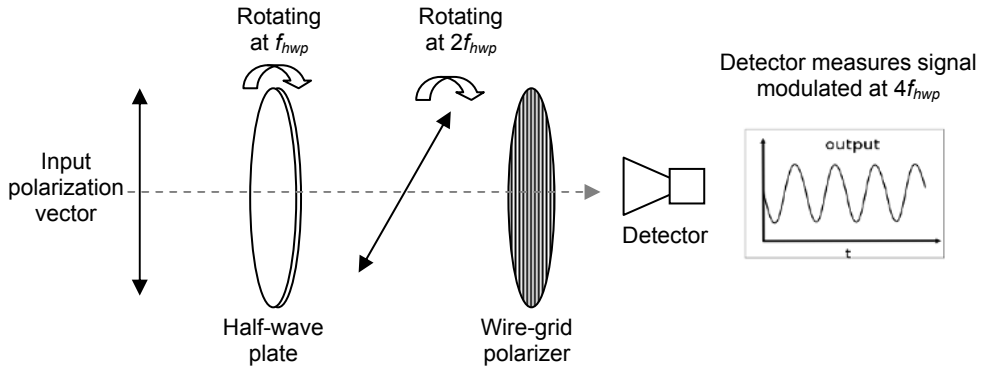

Figure 2.3: Polarimetry with HWP and fixed polarizing grid. Assuming constant polarized illumination of HWP spinning at frequency *f*, the polarization vector exiting the HWP rotates at *2f*. Then passing through a wire-grid polarizer before reaching the detector, measured intensity varies sinusoidally at *4f*.

For the Antarctic campaign we plan to use f_{hwp} = 6 Hz, placing the polarized signal at 24 Hz. To date, the EBEX system has demonstrated continuous stable rotation at 2 Hz over several

consecutive days. As outlined in the next subsection, we plan to operate ~1,400 detectors at a sampling rate of ~191 Hz for the LDB mission - over 14-days we anticipate accumulating almost 2 Terabytes of data.

Based largely on lessons learned from the MAXIPOL project, EBEX implements two significant upgrades in the HWP subsystem: an 'achromatic' half wave plate (AHWP) and a superconducting magnetic bearing (SMB). The AHWP is a 'stack' of 5 individual sapphire plates which are glued together with their birefringent axes aligned at particular offsets to achieve (amongst other advantages) polarization modulation efficiency above 98% across virtually the entire range of frequencies admitted by the instrument [26]. Modulation efficiency and other performance parameters are discussed more extensively in Chapters 3 and 4. MAXIPOL employed a conventional mechanical bearing for HWP rotation and eventually deemed this component largely responsible for significant systematic error in the polarization signal discovered in the flight data [27,28]. Rotating the wave plate on a SMB is expected to reduce friction by more than 4 orders of magnitude compared to the MAXIPOL system [29].

2.2.3 Detectors

EBEX exploits two relatively recent developments in millimeter-wave technology and is the first non-terrestrial platform to employ this type of detection system: transition edge sensor (TES) bolometers read out by Superconducting QUantum Interference Devices (SQUIDs) [33,34]. Each TES is physically coupled to a spider web-shaped absorber, much like the neutron transmutation doped (NTD) Germanium bolometers deployed in many past and present CMB experiments. The basis for TES operation is sketched in Figure 2.4 - over a small range of sub-Kelvin temperatures, resistance varies steeply as a function of temperature. The cryogenic refrigerators and optical filters inside the EBEX cryostat are intended to ensure that the detectors would thermalize at a temperature below their critical temperature (T_c) under only the ambient radiative load at float. With the application of electrical current, the TES can then be biased into transition between its normal and superconducting regimes. While in the transition regime, minute changes in radiative flux (P_{rad}) will generate minute variations in temperature which correspondingly result in macroscopic changes in resistance (ΔR).

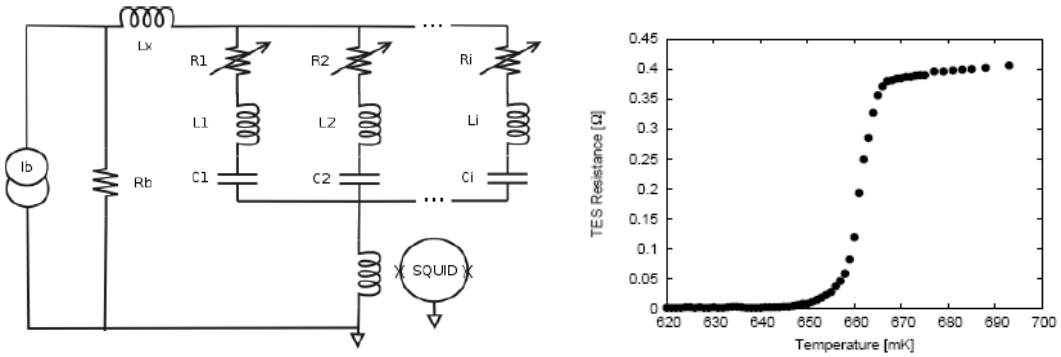

Figure 2.4: Left - Basic circuit diagram for TES bolometer readout. Ib is bias current, Rb the bias resistance, and R# the bolometers. Inductor and capacitor in series with each detector define AC bias frequency which is different for each bolometer, facilitating our digital frequency multiplexed (DfMUX) readout scheme. Up to 16 bolometers can be read out with a single SQUID, which responds to magnetic field variations generated by changing current in the adjacent inductor. Lx represents parasitic inductance due to cold wiring. Right - Example of *R(T)* curve for a TES bolometer with $T_C \sim 660$ mK.

While a typical NTD readout system extracts P_{rad} by measuring changes in current or voltage across the bolometer (which is a function of ΔR), the TES is a null detector – total power on the device is maintained at a constant value by applying variable electrical power to compensate for changes in P_{rad}. In practice we use a constant bias voltage and read out the varying bias current. $P_{electrical} = I_{bias} \cdot V_{bias}$ reveals the electrical power being applied to the bolometer in each data sample. Changes in $P_{electrical}$ from sample to sample are therefore a direct measure of varying incident radiative load. Readout is accomplished through SQUIDs which act as a flux to voltage transducer, responding to the varying magnetic field generated by the varying current present in the wire leading to the bolometer circuit. The voltage across the SQUID is then digitized and logged by a suite of warm electronics as a function of time. These time-ordered data (TOD) are eventually converted into physical units and combined with telescope pointing information to reconstruct a map of millimeter-wave brightness on the sky.

Analysis and map-making are accomplished long after TOD have been collected. However, there is often much to be gained by viewing data in real-time, especially when executing ground-based calibration experiments. We use the software package *kst* to read and display bolometer data as it is being recorded, choosing to view it in the time and/or frequency domain [60]. In the time domain, bolometer response is displayed in digital counts, where each count represents some unit of bias current. The conversion between counts and current depends on the system settings at the time, but these are well known quantities. Counts are abbreviated on

time domain plots as *ADC*. Though this use of the acronym is inconsistent with its standard definition (analog-to-digital conversion), we will use it throughout this thesis to conform with kst. Since the system maintains constant *total* power across a bolometer and ADC is a reading of *electrical* power applied at any given moment, higher ADC = lower mm-wave flux. As the reader will discover in Chapter 4, we applied a modulated input signal for many of our pre-flight calibration tests which made the bolometer response easiest to interpret (and at highest S/N) in the frequency domain. An example of bolometer data as displayed in both domains is shown in Fig. 2.5.

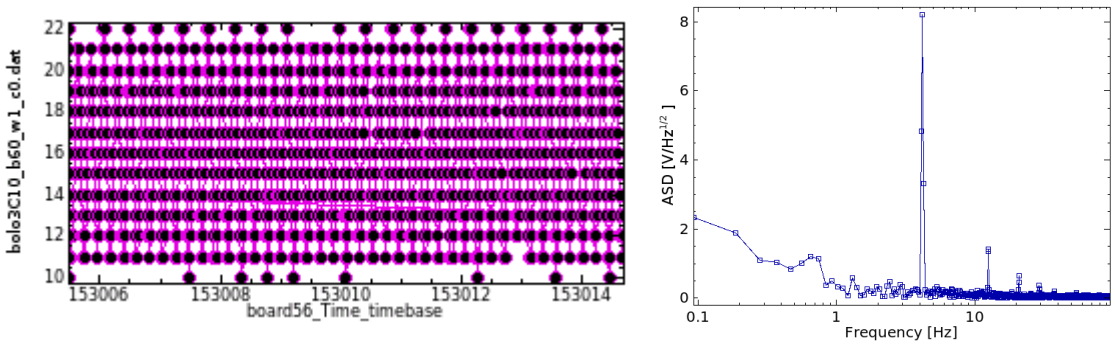

Figure 2.5: Example bolometer time-ordered data (TOD) as displayed in real-time with kst software. Left – 10 seconds of bolometer data in time domain; y-axis units are ADC and label designates bolometer (b60 = readout board #60, w1 = wire #1, c0 = channel #0). Signal being measured is modulated at ~4 Hz with a magnitude of ~ 10 ADC peak-to-peak. The x-axis is timestamp in seconds, sample rate = 190.73 Hz. Right - Frequency domain view (FFT); y-axis units *ASD* are measure of spectral density based on ADC. The *V* in $V/Hz^{1/2}$ stands for *vector*, *not* volts.

The exchange of electrical signals between bolometers and SQUIDs required us to design a new type of microstrip wiring which provides an unprecedented combination of thermal isolation and parasitic inductance suppression. The development and deployment of the EBEX microstrip is covered in Appendix A.

Figure 2.6 shows a single focal plane which is made up of seven decagon-shaped wafers. Each wafer contains 139 bolometers which have been fabricated using standard thin film deposition and optical lithography, for a total of 1,946 detectors over two focal planes [31]. Optics simulations using Zemax and Code V predict that the Gregorian Dragone design produces diffraction-limited performance above a 0.85 Strehl ratio across ~21 cm of each 25 cm diameter focal plane. Approximately 40 bolometers lie beyond this threshold on each of the 12 outer wafers, for a total of 480 detectors. We will exclude the data from these *edge* detectors in the

final science data set, which leaves ~1,440 bolometers. For comparison, there are a total of 40 detectors aboard WMAP.

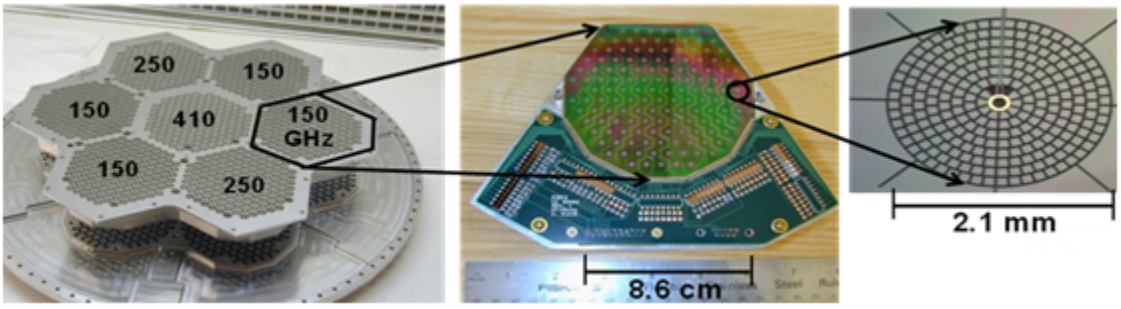

Figure 2.6: Left – Feedhorn array (waveguide array hidden underneath feedhorns in this view). Horns are smooth-walled, conical, and single-moded. Middle - Top view of single wafer with 139 bolometers and attached *LC board*. Right - Microscope view of single detector - TES is small dark rectangle between the two gray lead wires at 12 o'clock and just outside central gold ring. Rest of structure is spiderweb absorber.

3 Calibration Overview & Essential Hardware

3.1 Introduction

To accomplish the goals discussed in Chapter 1 with the instrument described in Chapter 2, we must characterize the instrument's response to a variety of *known* mm-wave input signals so that we can assess and ultimately subtract deleterious systematic effects when setting out to extract *unknown* mm-wave signals from our flight data. Ground-based calibration experiments along with dedicated calibration scan modes performed in flight will provide the information needed to develop a set of tools (models, transfer functions, etc.) that will be incorporated into the flight data analysis pipeline. Achieving our science goals will be in jeopardy if these tools are incomplete or known to insufficient accuracy. The precision required for an instrument's calibration is driven largely by the anticipated experimental S/N. The CMB emission spectrum as measured by the space-borne COBE satellite is a hallmark example of high experimental S/N – the signal of interest for that mission far exceeded the noise floor of the instrument. As elucidated in figures 1.3 and 1.4, this is decidedly not the case for detecting inflationary B-modes from a balloon-borne platform; even assuming the best-case scenario as predicted by classic inflation models, the IGB signal resides precariously close to the noise limit achievable with current technology.

Members of the EBEX science team have performed simulations and calculations to predict the accuracy with which we must know the instrument's performance in many areas. Based on these prescriptions we have designed and constructed a set of ground-based calibration experiments. Many of these tests are based on proven procedures demonstrated in the past on similar instruments, while others necessitated the fabrication of new hardware and the implementation of novel techniques. Sec. 3.2 introduces the most important systematic effects and in some cases relay an associated calibration criterion as determined by theoretical analyses. Sec. 3.3 details two key pieces of hardware that were developed specially for EBEX and used throughout the ground-based calibration effort executed prior to our NA test flight which is described in Chapter 4.

3.2 Systematic Effects and Calibration Strategy

Here we briefly survey the suite of performance characteristics and systematic effects to be addressed in the calibration strategy. The *optical efficiency* of the system relates directly to the instrument's fundamental sensitivity and will undoubtedly be less than unity as some fraction of the incident mm-wave flux will be lost to absorption and reflections before it ever reaches the detectors. For those photons that make it through to the focal plane, we must know how to correctly interpret the bolometer signal by defining the *absolute flux response* which converts from detector units (ADC) to physical units (*Watts*, or *Kelvin*). We must model the instrument's in-band *relative spectral response* in order to facilitate proper separation of the celestial emission sources that are expected to dominate our signal (CMB and dust). We also need to verify the level to which more energetic photons are rejected, as *high-frequency leakage* above a certain threshold could lead to overestimating and hence over-subtracting the dust foreground signal. The observing strategy – more specifically the AHWP rotation frequency and gondola scan speed – will be limited primarily by the *bolometer time constants* which must be determined on the ground before flight. The observing strategy is also predicated on the antenna response of the instrument, a trait predicted by optical modeling simulations but requiring empirical validation through *beam mapping* and *far sidelobe* experiments.

Whereas the effects outlined to this point are common to all telescopes past, present and future, polarimeters include an additional suite of systematics. The *polarization modulation efficiency* defines how effectively the instrument preserves and hence measures the polarized fraction of incident light; values below unity mean a loss of S/N in the polarization signal. *Polarization rotation* describes how the instrument changes the orientation of an incident polarization vectors en route from the primary mirror to the focal plane. A failure to determine this property within requisite uncertainty can cause E-B leakage, or misidentifying E-modes as B-modes. Finally, although a polarimeter is designed to characterize polarized light coming from the sky, a portion of the polarized signal measured by the detectors will have originated as unpolarized light, converted into polarized light by the telescope's optics. Appropriately labeled *instrumental polarization*, this effect is due primarily to differential emission, reflection, refraction and transmission within the instrument. The magnitude and orientation of this effect must be subtracted along with polarization rotation to avoid E-B leakage.

Table 1 provides a comprehensive summary of the current EBEX calibration strategy. The criteria (where defined) are derived on the principle that we must quantify the signal coming

from the effect to a level equivalent with what we expect for the IGB B-mode signal if $r = 0.004$ ($r = 0.004$ is a factor of 5 below our 2σ detection goal of $r = 0.01$). For some of these effects, a benchmark doesn't exist simply because it has not yet been studied in enough detail to develop one. Ongoing and future simulations will fill the gaps as necessary. Another subset includes those effects that are more aptly labeled performance characteristics than systematics. These include the rows where the criterion column lists *maximize*, *minimize*, and/or target values. We make a distinction between cryogenic and integrated experiments for clarity; both are ground-based tests that occur at different stages of the telescope integration process. The former are performed using the cryostat alone and the latter are executed after the cryostat has been mounted onto the gondola.

Table 3.1: Comprehensive overview of systematics, characterization criteria, instrument performance goals and calibration experiments.

Systematic Effect	**Criteria (if defined)**	**Cryogenic experiment (cryostat-only)**	**Integrated experiment (entire telescope)**	**In-Flight**
Optical Efficiency (OE)	maximize	Load bolos with 2 blackbody sources of different *T,* measure ΔP, OE = (measured ΔP) / (known input ΔP)	N/A	N/A
High-Frequency Leakage	minimize	Load bolos with modulated signal (chopper) through high-pass thick grill filter, leak = (measured chop ΔP) / (known chop ΔP)	N/A	N/A
Bolometer Time Constants (τ)	minimize (goal: 3 ms)	Load bolos with modulated signal (chopper), increase chop frequency, $\tau = (1/f_{chop})$ where response drops by 1/e	N/A	Extract τ from deconvolution with cosmic ray and/or other impulse events (glitches) in bolo TOD
Antenna Response (Beam Mapping)	8' FWHM (expected)	Step small cold load (aluminum disk) across window, warm load in background (300 K room) measure bolo response vs. disk position, plot/extract FWHM	Load bolos with modulated point source signal from artificial planet (AP), gondola scans, measure bolo response as function of azimuth & elevation, plot/extract FWHM and shape	Scan gondola over bright point source, measure bolo response as function of azimuth & elevation, plot/extract FWHM and shape

Polarization Modulation Efficiency (PME)	required: > 90% (expected: ~98%)	Load bolos with modulated polarized signal (chopper above external grid), HWP stationary, rotate external grid in steps, measure response (I) vs. grid orientation, PME = $(I_{max} - I_{min}) / (I_{max} + I_{min})$	N/A	N/A
Instrumental Polarization (IP)	± 0.05%	Load bolos with modulated unpolarized signal (chopper), HWP spinning, measure unpolarized response at chop freq (S at frequency f_1) & polarized response (S at $f_2 = f_1 - 4f_{hwp}$), IP = $S(f_2) / [S(f_1) + S(f_2))]$	Same method as cryogenic test but with modulated unpolarized source signal from AP, gondola stationary, HWP spinning	Scan gondola many full rotations, measure bolo response as function of RA & Dec, lock-in on CMB dipole signal (S at frequency f_{dipole}), find polarized signal (S at $f_2 = 4f_{dipole}$), IP = $S(f_{dipole}) / [S(f_{dipole}) + S(f_2)]$
Differential Band-Averaged Polarization Rotation (DPR)	pre-flight goal: 0.03 deg, in-flight goal: 0.1 deg	Method A: Load bolos with stable 300K blackbody (the room), HWP stationary, step external grid, measure response each step for 2 bolos, find which angle gives max response for each bolo, DPR = Δ*(max grid angle)* as function of bolo position in focal plane	Method A: Load bolos with modulated polarized AP signal (AP grid stationary), gondola stationary, HWP stationary, step external grid on cryostat window, measure response each step for 2 bolos, find which angle gives max response for each bolo, DPR = Δ*(max grid angle)*	Gondola scans CMB patch, make polarized CMB map from each individual bolo, extract E/B-modes, assign DPR as necessary to ensure consistent E/B in all maps
		Method B: Load bolos with modulated polarized signal, HWP spinning, measure response as function of HWP angle for 2 bolos, DPR = Δ*phase* between resultant plots for the 2 bolos	Method B: Load bolos with modulated polarized AP signal (AP grid stationary), gondola stationary, HWP spinning, measure response as function of HWP angle for 2 bolos, DPR = Δ*phase* between resultant plots for the 2 bolos	

Absolute Band-Averaged Polarization Rotation (APR)	required: 0.3 deg, pre-flight goal: 0.2 deg, in-flight goal: 0.04 deg	Same methods as cryogenic DPR, but with known absolute orientation of input polarization vector (in telescope coordinates)	Same methods as integrated DPR, but with known absolute orientation of input polarization vector (in telescope coordinates)	Gondola scans CMB, extract E/B-modes from polarized CMB map (all bolos), assign DPR as necessary to minimize (or eliminate) EB cross-correlation
Relative Spectral Response		Load bolos with modulated narrow-band mm-wave signal from Ebert-Fastie monochromator (EFM), step emission through each spectral band in small frequency increments, measure response as a function of input frequency	Same as cryogenic method, but with EFM mounted on AP. Method A: gondola stationary, EFM signal measured by 1 or few bolo(s), HWP stationary, adjust gondola pointing to measure other bolos. Method B: scan gondola	N/A
Polarization Rotation as a Function of Frequency [PR(ν)]		Load bolos with modulated polarized narrow-band mm-wave signal (EFM through external grid), HWP spinning, measure response as function of HWP angle, PR(ν) = *Δphase* as a function of input frequency	Same as cryogenic method, but with EFM mounted on AP (AP grid stationary)	N/A
Far Sidelobe Response	< -85 dB	N/A	Load bolos with modulated high-power mm-wave source (Gunn oscillator), gondola stationary, HWP stationary, measure response (*S*) as function of mm-wave source position, rejection(az,el) = $S(az,el) / S_{main\ beam}$	Scan gondola *near* bright source, measure bolo response as function of source az & el (relative to main beam), rejection = response / known source flux
Absolute Flux Response	± 5%	N/A	N/A	150/250 GHz: gondola scans CMB dipole, absolute flux response = measured dipole peak-to-peak (ADC) / known dipole peak-to-peak (W or K). 410 GHz: TBD (see Sec. 5.3)

3.3 Calibration Hardware

We have designed and fabricated a variety of new hardware for calibrating EBEX. The two most notable and ubiquitous devices, the Ebert-Fastie monochromator (EFM) and artificial planet (AP), are discussed here. Many others are described in less detail and in the context of their experimental application throughout Chapter 4.

3.3.1 Ebert-Fastie Monochromator

As stated in Sec. 2.2.1, the EBEX cryogenic optical system is designed to transmit light in three frequency bands centered on 150, 250 and 410 GHz where upper edge is defined by a pair of metal-mesh low-pass filters (LPFs) mounted near the focal plane and the lower edge is determined by a waveguide that acts as a high-pass filter (HPF). In our daily activities we commonly assume the cutoffs are infinitely sharp and the bands are tophat functions, but we know the true spectral response of the instrument will almost certainly deviate from this ideal model. Relative in-band spectral response is crucial because the two dominant emission sources observed in flight, dust and CMB, have distinctly different spectral characteristics. We must therefore determine a spectral response model for each band to use in the analysis pipeline for component separation.

Several groups have reported successful use of a Fourier Transform Spectrometer (FTS) for assessing spectral response, including MAXIPOL and BOOMERanG amongst many others [28,32]. Using this technique, data is processed and results extracted in the frequency domain after completing the experiment. We sought a different method that would allow us to more rapidly check both the performance of the experimental device and the spectral response of the instrument. The ensuing investigation of alternatives led us to the Ebert-Fastie monochromator (EFM). The following sections report details specific to our implementation, including design and tests performed after fabrication to compare actual vs. predicted performance.

3.3.1.1 Design

The Ebert-Fastie design was first described in 1952 and used for infrared spectroscopy [33,34]. As shown in Figure 1, it includes the components common to all spectrometers while offering the advantage of alignment simplicity that comes with using the same surface (spherical reflector)

both for collimating and focusing the beam. The device operates according the standard grating equation $m\lambda = d(\sin\alpha + \sin\beta)$ where α and β incident and exit angles relative to grating normal, m is the diffraction order, and d is the grating groove spacing.

When used as a spectrometer, the (typically) unknown emission spectrum of a source located at the entrance aperture is linearly dispersed at the exit aperture and measured by a focal plane array. As a monochromator, a source is placed at the entrance aperture and the user has the ability to rotate the grating around the vertical axis which allows him to alter α and β, effectively selecting a particular wavelength to be centered on the exit aperture. The range of wavelengths in the emitted beam depends on the linear dispersion of the system, which depends on various physical attributes of the device and is defined in Eq. 3.1 below. Although truly monochromatic emission would require an infinitesimally narrow exit aperture, this design is commonly referred to as a monochromator. Many examples of EFMs used at IR wavelengths exist, but we find few examples in the millimeter-wave regime and no previous instances of use in the CMB community.

We decided to construct our EFM at 2nd order with the following design goals:

1. Small enough to facilitate manual set-up and rapid maneuverability
2. Resolving power R ($\nu/\Delta\nu$) $\geq$ 40 at all pertinent wavelengths, or equivalently, providing $\geq$10 'monochromatic' data points per EBEX spectral band
3. Given goals #1 and #2, maximize signal-to-noise (S/N) at the EBEX focal plane

Goal #1 was predicated on our desire to maximize operational efficiency in the field (scientific balloon launching facilities) and provided a basic starting point for parameters f and W depicted in Figure 3.1. L_1, L_2, and diffraction grating parameters were then optimized to achieve goal #2 using the optical software package Code V. Further analysis identified the need for three separate diffraction gratings, one for each band. The gratings were cut from blocks of Aluminum 6061 with a wire electrical discharge machine (EDM) and given a blaze angle of 30˚ as shown in Figure 2. The spherical mirror was lathe cut from a block of Al 6061 and has a 1" wide rim around the cut area to facilitate rigid vertical mounting. The surface rms for these articles is < $\lambda_{min}/20$ (λ_{min} = 670 μm) to prevent deleterious scattering, and we polished the mirror by hand to permit laser alignment.

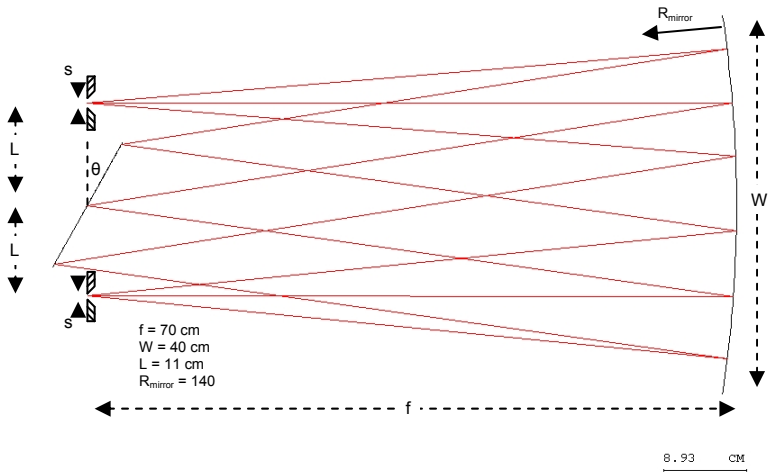

Figure 3.1: Code V simulation of Ebert-Fastie monochromator (EFM). Entrance aperture is on top, exit aperture at bottom. Only moving part is diffraction grating - varying θ changes wavelength centered on exit aperture.

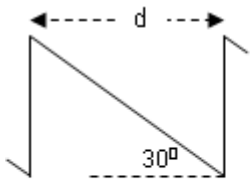

Grating	d	N (# of facets)
150 GHz	4.0 mm	37.5
250 GHz	2.4 mm	62.5
410 GHz	1.5 mm	100

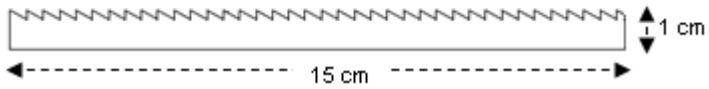

Figure 3.2: EFM diffraction grating design parameters. Gratings made from Aluminum 6061, fabricated by wire EDM at the University of Minnesota.

All hardware components shown in Figure 3.1 are mounted to a 4' x 2' optical bench and surrounded by an enclosure made from 1/16"-thick aluminum plates. The enclosure dimensions are 20" (H) x 20" (W) x 33" (L) and all interior surfaces are lined with eccosorb HR-10 to mitigate stray reflections. The gratings are attached (one at a time) to an aluminum post coupled to a 10-to-1 worm gear, which attaches to a 1/8" diameter cylindrical G10 shaft. The shaft extends out through a small hole in the enclosure and is fixed to the rotation axis of a Newport polarizer mount. This system provides the user manual control of the grating angle to an

accuracy of 0.1˚. With this level of angular certitude, the operator can center an emission frequency on the exit aperture to within ± 0.4, 0.7, and 1.0 GHz for the 150, 250 and 410 GHz configurations, respectively.

Given these parameters, we can predict resolving power ($R = \lambda/\Delta\lambda$) as a function of frequency. The number of facets on each grating (N) provides an initial constraint according to $R = N * m$ [40]. This constraint delivers the following band-dependent limits on R, all of which exceed our goal of $R \geq 40$: R = 75 (150 GHz), 125 (250 GHz), and 200 (410 GHz). A stricter constraint on R exists due to the slit width and magnification of the system. The collimating and camera surfaces effectively image the entrance aperture at the exit aperture and from the grating equation we derive that

$$R = \frac{m\lambda f_{coll}}{sd\cos\beta} \tag{3.1}$$

where f_{coll} is the focal length of the collimating lens (70 cm) and s is the width of the exit aperture. λ and β follow from our choice of grating angle θ given the otherwise fixed dimensions of the instrument. This leaves s as the only remaining variable, allowing us to choose its value for optimal performance.

In choosing the band-dependent values for s we aimed not only to achieve goal #2, but to accommodate goal #3 as well. The relationship between exit aperture width and S/N is explained in the next section. We converged on the following nominal values for s, which ensure R > 60 across all bands: 0.8 cm (150 GHz), 0.8 cm (250 GHz), and 0.7 cm (410 GHz).

Having defined the physical attributes of the EFM, S/N is at this point more a consequence of design rather than a driver. It depends significantly on factors beyond the control of the monchromator such as the optical efficiency of the EBEX cryostat, cryogenic antenna response, and instrument noise. A unique beam (antenna response) exists for each individual detector, all of which are theoretically predicted and modeled as a truncated Gaussian. Truncation is provided by the cold stop located at the AHWP, reducing the antenna response by ~20% in comparison to a full Gaussian. The flux collected in each beam is directly related to the product of cross-sectional area (A) and solid angle (Ω), $A\Omega$. Since $A\Omega_{EBEX}$ is fixed, $A\Omega_{EFM}$ must match it in order to produce an ideal 'image' of the EFM exit aperture on a single EBEX detector. While illuminating a single detector at a time is non-trivial in terms of optical alignment, it must be our goal for two primary reasons: (1) simultaneous illumination of multiple detectors with the EFM beam would decrease S/N in each individual detector due to geometric flux dilution and (2)

make it difficult to assess what wavelengths are actually incident on each individual detector receiving signal since the monochromator signal is spectrally dispersed across the exit aperture, and hence the beam.

We can assess $A\Omega_{EFM}$ for each band using the current design. $A = \pi r_{aperture}^2$ (we use circular apertures), and Ω is derived from f and L. Table 3.2 compares $A\Omega_{EFM}$ with $A\Omega_{EBEX}$ and reveals similarity within a factor of 3 in all cases. We can force $A\Omega_{EFM} = A\Omega_{EBEX}$ with different choices for s, but this would of course alter the range of wavelengths spanning the exit aperture (a.k.a., the 'window function'). Basic design modifications could likely further optimize S/N and resolving power, and should be considered for the future.

Table 3.2: A comparison of the Ebert-Fastie monochromator and EBEX beams. For EBEX we have assumed $A\Omega = \lambda^2$ using the center of the band (150, 250, 410 GHz); for the EFM we have calculated $A\Omega$ from physical design parameters.

band (GHz)	exit aperture (cm)	A (cm^2)	Ω (sr)	$A\Omega_{EFM}$	$A\Omega_{EBEX}$
150	0.8	0.50	0.04	**0.020**	**0.038**
250	0.8	0.50	0.04	**0.020**	**0.015**
410	0.7	0.38	0.04	**0.015**	**0.006**

We are also interested in matching the *f/ratio* of the Ebert-Fastie beam to the EBEX antenna response. We want the monochromator beam entering the EBEX cryostat to replicate the beam that will come from the secondary mirror when the telescope is fully assembled. Otherwise, the monochromator beam will traverse a different path than the integrated beam and potentially introduce systematic effects difficult to identify, quantify, and remove. As designed, the EFM beam emerges from the exit aperture at ~ *f/5.3*, which differs significantly from the *f/1.7* EBEX beam. Additionally, the EBEX cryostat is 'upward-looking', and the monochromator is most naturally 'sideways-looking' (exit beam directed horizontal to the ground). Coupling the two systems thus requires a change in f-ratio and a 90˚ turn.

Again Code V was used to explore the parameter space of possible solutions, and we converged on the design shown in Fig. 3.3. The surface curvatures and positions of the collimating and camera lenses convert between *f/5.3* and *f/1.7*, while the 90˚ turn is accomplished with a simple fold mirror. The lenses are biconvex ($R_{collimating}$ ~ 50 cm, R_{camera} ~ 25 cm), 6" in diameter, have a 1" rim around the edge to facilitate mounting, and are made from ultra-high molecular weight polyethylene (UHMWPE). This is the same material used for the EBEX

cryogenic lenses, measured at Cardiff University to have a constant refractive index of 1.51 between 100 and 500 GHz (ref). The fold is a ¼" (thick) x 7" (W) x 18" (L) piece of Al 6061, the thickness chosen to ensure negligible deflection (< 0.1˚) under its intended mounting conditions. All surfaces have rms < $\lambda_{min}/20$, the UHMWPE lenses are not anti-reflection (AR) coated, and the fold mirror was polished by hand to facilitate laser alignment. Further explanation of the physical mounting scheme for this 3-element 'beam-coupling' system is found in Sec. 4.5.

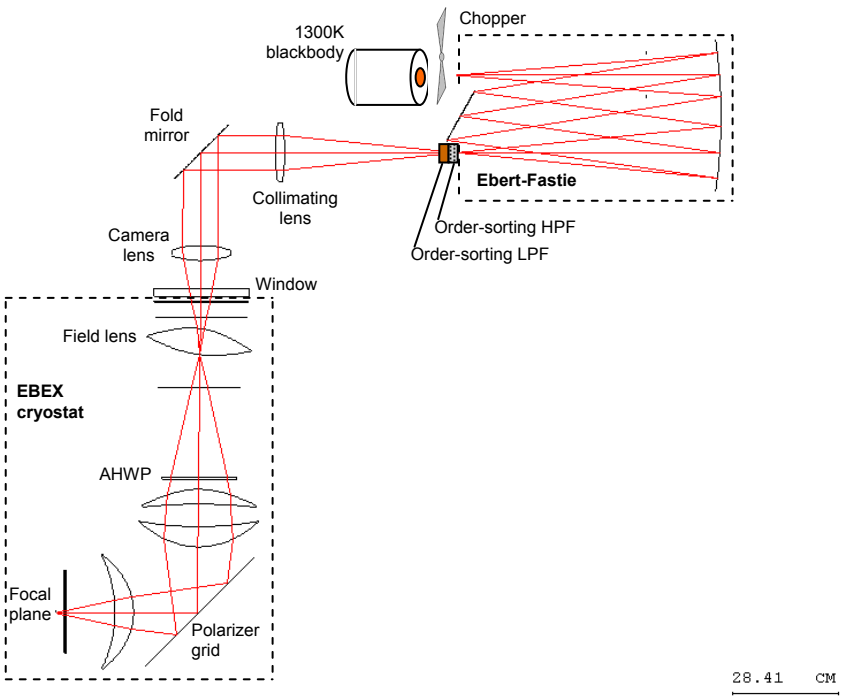

Figure 3.3: Red lines represent 150 GHz light in Code V simulation including EFM, EBEX cryostat, and the 3 coupling elements (collimating lens, fold mirror, camera lens).

The source placed at the Ebert-Fastie entrance aperture also plays a key role in the S/N equation. The monochromator output must be modulated so that its signal is easily distinguishable in the data timestream from ambient optical loading (and variations therein, which should occur on much longer timescales than the monochromator chop frequency). Furthermore, the magnitude of the modulated signal should be maximized since it maps directly to S/N. We therefore use the hottest source at our disposal, a ~1300 K laboratory blackbody source, chopped by a smooth room temperature aluminum blade. This and similar blades were used extensively as

the cold load for signal modulation throughout the initial ground-based calibration program executed in Ft Sumner and described in Chapter 4 - throughout the rest of this document we assume these devices are at room temperature (~ 300 K) and have 5% emissivity for an effective ~15 K load.

The two order-sorting filters shown mounted at the EFM exit aperture in Fig. 3.3 are in place to attenuate flux from diffraction at orders other than $m = 2$. For example, when we have placed the diffraction grating to center 150 GHz 2nd-order flux on the exit aperture, we will have simultaneously dialed in 75 GHz at 1st –order, 225 GHz at 3rd-order, 300 GHz at 4th-order, etc. This phenomenon holds for all bands according to the equation $\nu_{m\neq 2} = (m/2)\cdot\nu_{m=2}$. With the set-up depicted in Fig. 3.3 the order sorters are actually unnecessary because the off-order flux will be suppressed by the band-defining filters inside the EBEX cryostat. However, we intend to perform a separate experiment with a separate detector system in a separate cryostat to independently characterize the spectral emission model of the EFM itself, and for this test we *will* need a pair of order sorters. Otherwise, in that experiment we would expect significant leakage from flux at $m \neq 2$ that would be difficult or impossible to decouple from the 2nd-order peak that we're trying to characterize. And because we can't reliably predict the effect these order sorters will have on the emission curve *within* the EBEX bands, they must remain installed on the EFM during the EBEX spectral response experiments.

For the low-pass order sorters we simply used leftover pieces of the EBEX metal-mesh focal plane LPFs. In the EBEX cryostat there are two LPFs with slightly different cutoff frequencies (ν_c) mounted over each wafer. We employed just one LPF at the EFM exit aperture (a different filter for each band, of course), in each case choosing the one with greater ν_c. Each of the three LPFs used were circular and had a 1" diameter.

For the HPFs we fabricated a set of three thick grill filters (TGFs). Most aptly described as a dense hexagonal pattern of identical waveguides, the cutoff frequency for a TGF is completely defined by the size of its holes and is calculated with

$$\nu_c(GHz) = \frac{1.841x10^{-9}\cdot c}{\pi\cdot d} \tag{3.2}$$

where d is the hole diameter [35]. The sharpness of the cutoff is determined by t/d where t is the filter's thickness. Nt/d is used to approximate transmission below the cutoff which roughly equals $N\cdot(-32dB)$. Experimental data showing steepness at the cut-off as a function of t/d

drove our decision to use $t/d \sim 3$ [36]. At $\nu >> \nu_c$, transmission is approximately equal to the ratio of open area (holes) to total area (holes + metal).

Anticipating a maximum EFM exit aperture diameter of ½", we designed the pattern area as a ½" x ½" square to simplify the drilling process. The TGFs were made of aluminum 6061 and the holes were drilled on a computer-controlled milling machine. Many of the holes retained burrs after drilling, but these were easily removed by placing the pieces in a sonicator tank followed by lightly sanding both surfaces. The 150 GHz HPF design is presented as an example in Fig. 3.4, which also includes manufacturing specifications for the other three filters. The holes above and below the pattern area were included for mounting – screws passing through these holes couple the TGF to the exit aperture plate while 'sandwiching' the metal-mesh LPF in-between as pictured on the right side of Fig. 3.4. The transmission spectra for all filters are shown in Fig. 3.5. The bottom panel of Fig. 3.5 captures the intent of the order-sorting scheme pictorially.

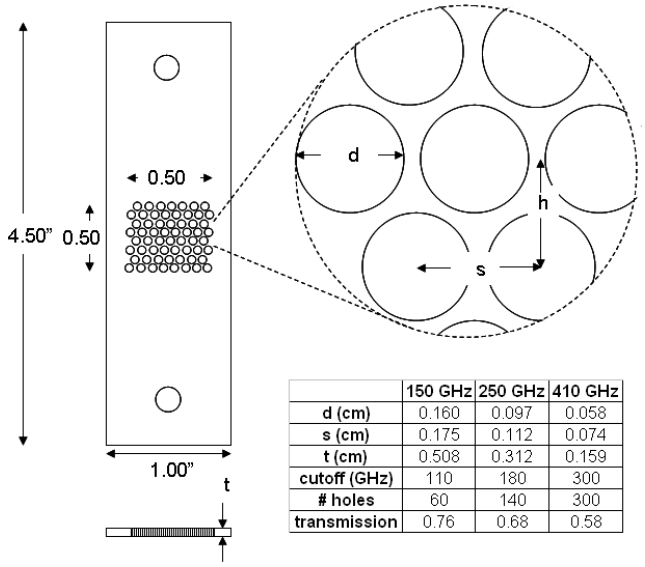

	150 GHz	250 GHz	410 GHz
d (cm)	0.160	0.097	0.058
s (cm)	0.175	0.112	0.074
t (cm)	0.508	0.312	0.159
cutoff (GHz)	110	180	300
# holes	60	140	300
transmission	0.76	0.68	0.58

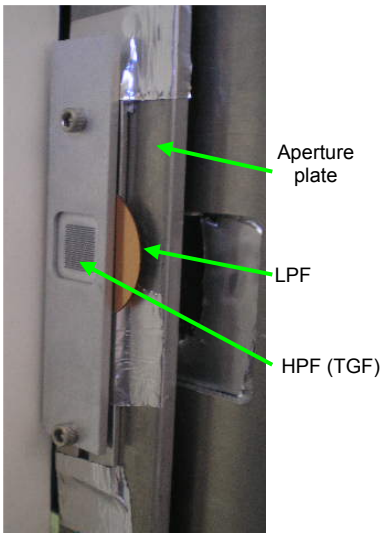

Figure 3.4: Left – Design scheme and manufacturing specifications for each of three thick grill (high-pass) EFM order-sorting filters along with expected transmission at $\nu >> \nu_c$. Right – Photo of 410 GHz order-sorting HPF and metal-mesh LPF (copper colored disk) mounted at EFM exit aperture.

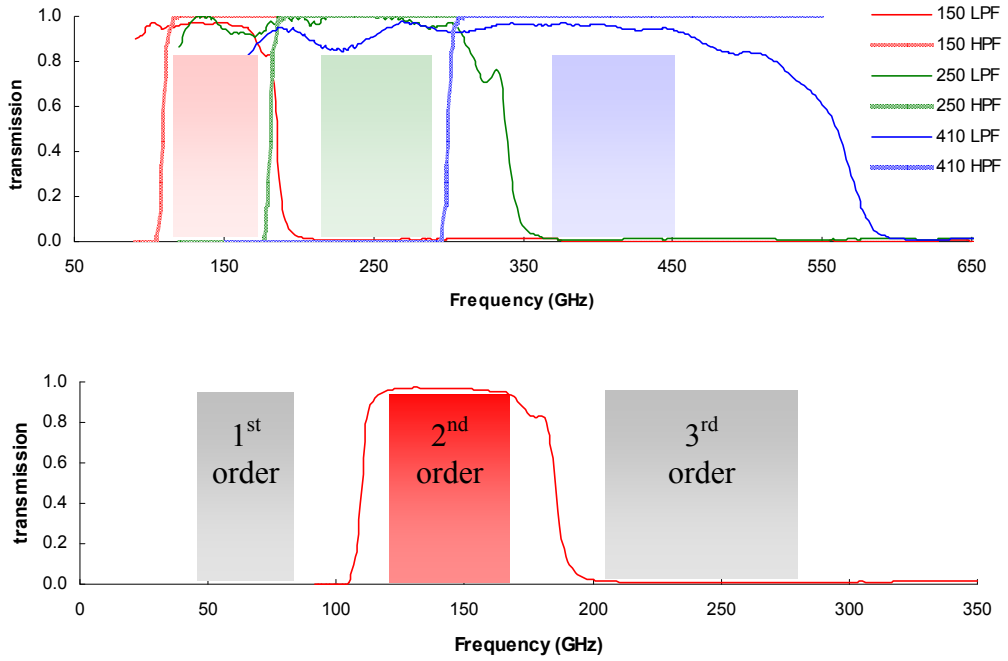

Figure 3.5: Top – Transmission spectra for high- (shaded line) and low-pass (solid line) EFM order-sorting filters. LPF spectra measured by FTS at Cardiff University; HPF spectra predicted from waveguide theory. Shaded areas are predicted EBEX bands. Bottom –Red shaded area is predicted 150 GHZ band. Grey areas indicate spectral range of 1st and 3rd order flux correlated with grating angles used for intended 2nd order flux. Solid line is combined 150 GHz order-sorting filter transmission spectrum.

Noise is the final component to consider in our S/N prediction. The TES bolometer fabrication specifications imply detector noise ~1 x 10^{-17} W/√Hz - although this value has not yet been achieved, we adopt this value as our baseline assuming the detectors will meet specifications in the near future. To verify our expectation of photon-noise limited performance, we assume the optical efficiency of the instrument will be significantly lower than unity and proceed to calculate correlated photon noise using

$$P_{rms} = \sqrt{2h\nu\langle P_b\rangle\left(1+a\varepsilon\left(\frac{KT}{h\nu}\right)\right)} \quad \text{W/}\sqrt{\text{Hz}} \tag{3.3}$$

where $\langle P_b \rangle$ is the average power in the background, a is the optical efficiency, and ε is the background emissivity [37]. This form assumes $h\nu << KT$ and $a\varepsilon << 1$,both of which are assumed true in our case. At this point a is likely predictable to no better than an order of magnitude; here we use $a = 0.005$ which is likely pessimistic but aligns closely with preliminary measurements made prior to the NA test flight as outlined in Sec. 4.1. Assuming an ideal 150

GHz spectral response (133-173 GHz tophat) and $T_{background}$ = 300 K with ε = 1, P_{rms} = 2.7 x 10^{-16} W/√Hz. With similar assumptions, P_{rms} = 4.5 x 10^{-16} and 7.4 x 10^{-16} W/√Hz for the 250 GHz and 410 GHz bands, respectively. We therefore conclude the instrument will indeed be photon noise limited during ground-based testing and use photon noise for our S/N projections.

The modulated signal ΔP (in *Watts)* absorbed at the focal plane is estimated with

$$\Delta P = A\Omega * a * \left(\varepsilon_1 \int_{\nu_1}^{\nu_2} \frac{2h\nu^3}{c^2} \frac{1}{e^{h\nu/kT_1} - 1} d\nu - \varepsilon_2 \int_{\nu_1}^{\nu_2} \frac{2h\nu^3}{c^2} \frac{1}{e^{h\nu/kT_2} - 1} d\nu \right) \; W \qquad (3.4)$$

where we for now assume perfect optical coupling between Ebert-Fastie and EBEX, T_1 = 1300 K (lab blackbody source), T_2 = 300 K (aluminum chopper blade), ε_1 = 1, ε_2 = 0.05 and $A\Omega$ represents the frequency-dependent antenna response. The limits of integration, ν_1 to ν_2, represent the spectral window function, which is defined by the linear dispersion of the EFM (dependent on grating angle and exit aperture width). In this largely ideal framework, we predict S/N ($\Delta P/P_{rms}$) ≥ 100 over 1 second of integration at each monochromator setting and across each band.

3.3.1.2 Validation Testing

After completing construction of the Ebert-Fastie, we executed a set of tests with a discrete Spacek Labs 110 GHz Gunn oscillator to assess the spectral performance of the system. As previously discussed and illustrated, the 150 and 250 GHz gratings are built to center the 2nd order diffraction peak across their bands on the exit aperture when sweeping through grating angles of approximately 30 ± 5˚. Though 110 GHz is below the intended spectral range of the Ebert-Fastie and the grating designs are not optimized for this wavelength, there are nonetheless certain grating angles at which 110 GHz diffraction peaks should be seen at the exit aperture. These angles are easily predicted with the grating equation. With the 150 GHz grating installed, the 1st order peak should be seen with the grating at 19.9˚ and the 2nd order peak at 43.0˚. With the 250 GHz grating, the 1st order peak is the only one available and should occur at 34.6˚. No 110 GHz peaks are accessible with the 410 GHz grating.

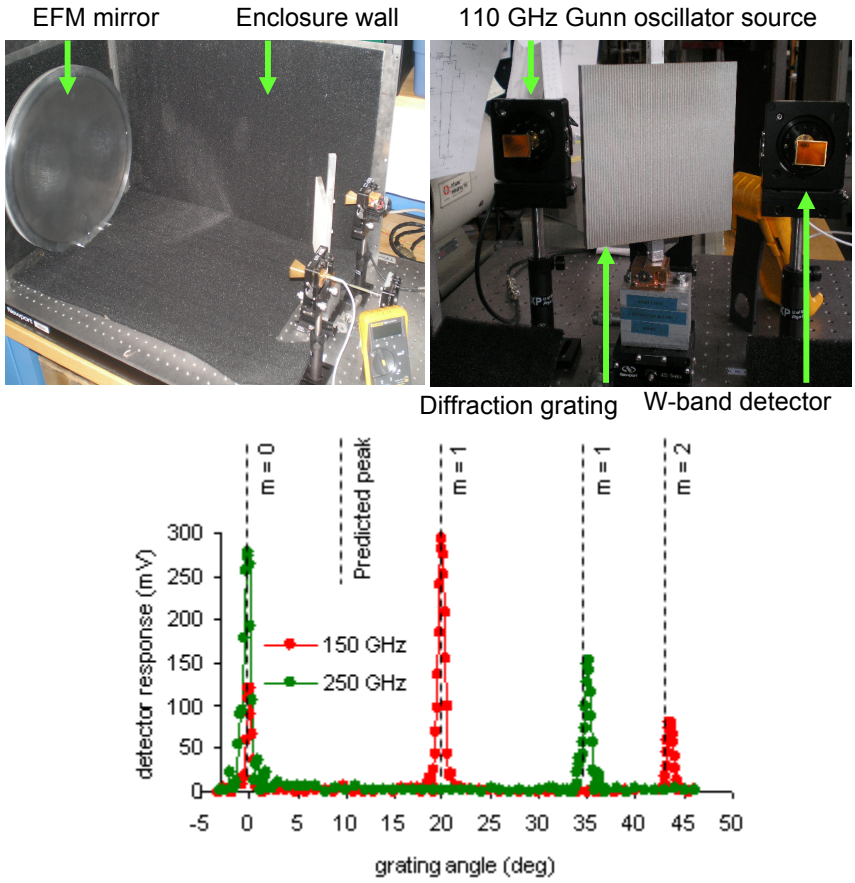

Figure 3.6: Top - Set-up for EFM validation test using 110 GHz Gunn oscillator source and broad W-band detector. Left – Data and results. Diffraction peaks measured/predicted at 20.0˚/19.9˚ (150 GHz grating, m=1), 43.6˚/43.0˚ (150, m=2), and 35.1˚/34.6˚ (250. m=1).

Figure 3.6 shows the experimental set-up with the 110 GHz source placed at the entrance aperture and W-band detector at the exit aperture. The detector converts mm-wave flux into an electrical signal, easily read out with a standard voltmeter. First we stepped the 150 GHz grating from -2˚ to 45˚ and recorded the signal at each step. The procedure was repeated after replacing the 150 GHz grating with the 250 GHz grating. Results are plotted in the bottom panel of Figure 3.6, verifying that the expected diffraction peaks were measured at grating angles consistent with predictions.

Perhaps the most obvious feature is the variance in the magnitude of the peaks. We learn nothing from the absolute values on the y-axis since they depend wholly on the power generated by the source and response function of the W-band detector. However, the *relative* magnitude of the two peaks implies a systematic effect not included in our current S/N prediction where we

implicitly assumed unity transmission at all frequencies. Figure 3.6 implies that losses within the device are at minimum order-dependent, which is not surprising, considering the presence of a blazed grating. The literature concerning diffraction grating transmission efficiency confirms this result and indicates that grating behavior is frequency dependent as well [38]. It also implies that predicting grating efficiency analytically represents a significant computational challenge which exceeds our present means and motivation.

However, in Loewen [38] we find plotted a set of theoretical and experimental efficiency curves for several grating shapes and spectrometer designs. One pair of curves in this paper represent a situation analogous to our own EFM (Fig. 3.7). Table 3.3 compares and contrasts Loewen's design parameters and those true for our monochromator. The most conspicuous discrepancies are in wavelength and angular deviation (A.D. = $|\alpha - \beta|$, or *off-Littrow* angle). Concerning wavelength, the authors warn to proceed cautiously if extrapolating their results to shorter wavelengths as surface roughness and dimensional uncertainties become more likely to degrade efficiency in unpredictable ways. At millimeter wavelengths, we expect no such effects. As for angular deviation, Loewen presents efficiency curves (Figures 12, 16, and 17) for 3 separate cases where the only difference is A.D. These curves show that absolute efficiency is a weak and inverse function of A.D., but the shape and peak location (along the $m\lambda/d$ axis) are virtually unaffected. We therefore retain confidence in the model here as well since we are only concerned with relative efficiency for our current application.

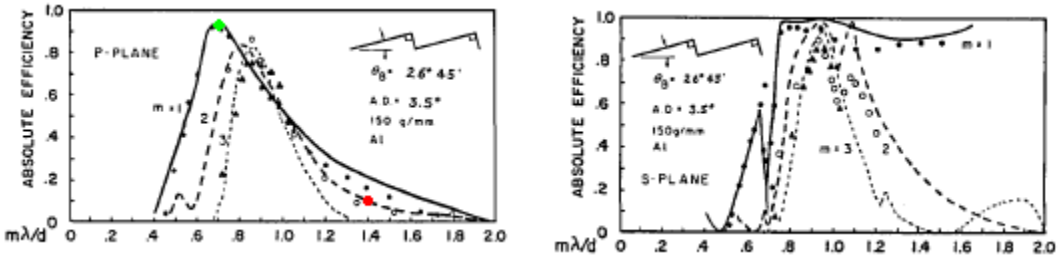

Figure 3.7: Transmission efficiency for blazed, aluminum diffraction gratings from [38]. Theoretical predictions for orders m=1,2,3 depicted as solid, dashed, and dotted lines, respectively. Experimental data are plotted as points. The two panels describe two orthogonal polarization states, P and S, referenced to the plane of the grating. 110 GHz source and detector were oriented in P plane during EFM validation testing. Green dot indicates the point on the x-axis corresponding to our 150 GHz 1st order peak; red dot marks the 2nd order peak.

Table 3.3: Comparing spectrometer design parameters assumed in [38] for predicting theoretical diffraction grating efficiency vs. our EFM. We contend (and argue in the text) that discrepancies will introduce negligible errors when using grating efficiency curves shown in Fig.. 3.7 in deriving an EFM relative flux model.

	grating material	**blaze angle**	**blaze peak angle**	**groove spacing (d)**	**wavelength (λ)**	**off-Littrow angle (A.D.)**
Loewen	Alum.	26.75 deg	90 deg	0.007 mm	IR	3.5 deg
EBEX	Alum.	30 deg	60 deg	4 mm	2.72 mm	22 deg

Based on the content of Table 3.3 and the arguments outlined in the previous paragraph, we contend that to first order, directly using Loewen's efficiency curves as a basis for interpreting our results is warranted.. For our experiment, λ = 2.72 mm and d = 4 mm so that $m\lambda/d$ = 0.7 and 1.4 for m=1 and m=2, respectively. In Fig. 3.7, 1st-order is marked with a green dot and 2nd-order is marked with a red dot. With these points we read off the predicted efficiency ratio (1st order/2nd order) ~ 0.9/0.1 ~ 9. In our 110 GHz measurements we see the ratio of peak magnitudes as (1st order/2nd order) ~ 300mV/80mV ~ 3.5. While the theoretical peak ratio is a factor of three greater than what we measured, there is clear agreement on the 1st order peak being significantly greater than the 2nd order peak. On this basis we suspect that grating efficiency is largely responsible for the difference in measured peak heights. We therefore use Loewen's results to derive a grating efficiency curve for our EFM which we will then include in our final theoretical model of relative flux as a function of frequency. We assume the Ebert-Fastie is unpolarized and hence use both plots shown in Fig. 3.7, calculating the mean of the 2nd-order P- and S-plane curves over $0.7 < m\lambda/d < 1.2$. The resultant EFM grating efficiency model is illustrated in Fig. 3.8.

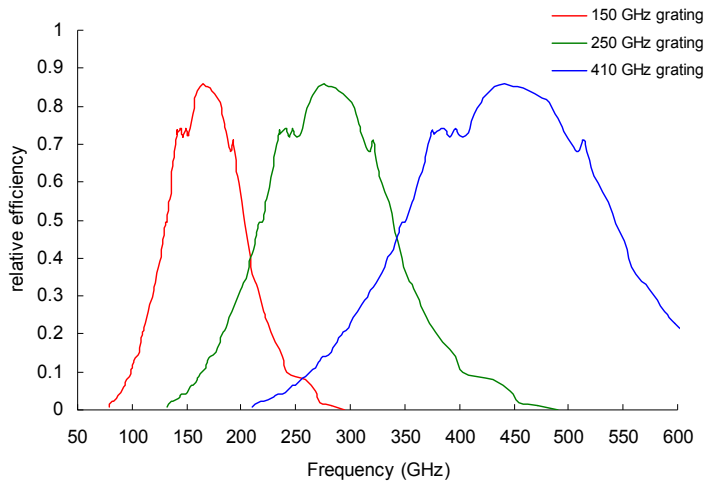

Figure 3.8: Theoretical diffraction grating efficiency curves derived for our EFM from Fig. 3.7.

A more subtle but equally interesting aspect of our 110 GHz data is the slight inconsistency between predicted and measured peak grating angles – the angles at which we measure the diffraction peaks are consistently greater than predicted. With the 150 GHz grating, the 1st and 2nd order peaks appear 0.1˚ and 0.6˚ later than expected, respectively. With the 250 GHz grating, the offset of the 1st order peak is 0.5˚. Though small, these offsets would alias the expected center frequency emitted by the Ebert-Fastie at a particular grating angle. For example, during typical operation in the 150 GHz band, the Ebert-Fastie sweeps through ~4 GHz/deg so a 0.7˚ error would introduce a 2.8 GHz shift in the expected central emission frequency. At ~7 GHz/deg in the 250 GHz band, a 0.5˚ offset would cause a 3.5 GHz shift. Since no criterion yet exists for EBEX spectral response calibration (see Table 3.1) it is difficult to quantify the consequences of this effect or determine whether it is significant enough to address further. However, it seems prudent to consider potential causes and make corrections if the culprit is easily identified and can be resolved mechanically or procedurally.

We present here the three most viable of many phenomena identified as possible causes for the observed discrepancy between theory and data:

1. The Gunn oscillator source was emitting at a frequency other than 110 GHz.
2. The actual grating groove spacing is different than that specified for machining.
3. The assumed worm gear ratio in the grating rotation mechanism was incorrect.

According to test data from the manufacturer, ν_{source} is a function of bias voltage and ranges from 109.8 to 110.2 GHz. Taking source frequency as the only free parameter, the measurements can be rectified if ν_{source} = 109.6 GHz for the 150/1st order peak (20.0˚), 108.5 GHz for the150 GHz/2nd order peak (43.6˚), and 108.7 GHz for the 250 GHz/1st order peak (35.1˚). Since a different frequency is needed to account for each of the 3 data points and each observed peak requires ν_{source} < 109.8 GHz, this explanation seems highly unlikely.

The systematic peak shifts could also be explained if the actual grating groove spacing (*d*) is lesser than the value specified for machining. The required deviation varies significantly from peak to peak and is in all cases > 13 μm. The machining tolerance was ± 3 μm, and caliper measurements made after fabrication indicate that each grating was machined to spec.

The growing discrepancy between predictions and measurements with increasing grating angle implies the idea of a wrongly assumed gear ratio. A true gear ratio of 10.14-to-1 would rectify the measurements to within 0.1˚ in each case. However, we performed an independent assessment of the gear ratio using the same set-up shown in Fig. 5 and determined it to be (10 ± .005)-to-1.

Therefore, with no apparent explanation for the observed discrepancies at this point, we will simply include the effect as an uncertainty in the current analysis pipeline.

3.3.1.3 Conclusions

With the theoretical predictions, experimental validation, and assumptions discussed above, we plot in Fig. 3.9 a theoretical model of relative flux as a function of frequency. It incorporates the source (blackbody/Planck function), grating efficiency (Fig. 3.8), and spectral resolution (window functions). We use this model in our preliminary assessment of the instrument's spectral response in Sec. 4.5. We ultimately intend to determine this model empirically. That effort is underway and is discussed in Sec. 5.2.

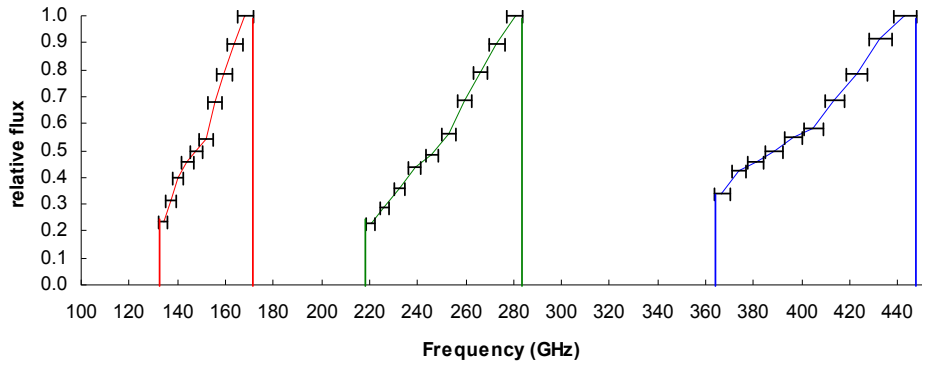

Figure 3.9: Theoretical EFM relative flux model calculated from monochromator design, source emission spectrum, and analytical diffraction grating efficiency model. Horizontal error bars represent window functions for each diffraction grating angle assuming our baseline plan to collect 10 data points per band.

3.3.2 Artificial Planet

In Table 3.1 we state that 7 of the 12 systematic effects can and/or will be probed at least partially through experiments with the fully integrated telescope. Ideally these tests would be accomplished with the use of a bright, stable, polarization-controlled, modulated emission source at infinite distance from the gondola. Unfortunately no celestial objects meet these criteria, so we must construct a device to simulate an astronomical source with the aforementioned characteristics. Though impossible to truly place at infinity, the telescope's far-field would suffice. Using the standard definition $2D/\lambda$, the far-field regime for EBEX begins at ~ 1 km. At this distance, a beam-filing source spans a diameter of ~ 2.5 m assuming the predicted 8' beams.

Constructing a stable, unpolarized, bright modulated source with a width on the order of tens of centimeters at a distance of 1 km would suffice as a point source to allow ground-based beam mapping and instrumental polarization experiments. Not only is building this type of device mechanically feasible (e.g., an eccosorb-filled cooler of LN_2 chopped with a 300 K eccosorb-covered blade), a quick calculation shows that it would permit high S/N results for both of the aforementioned instrument characteristics. Building a polarized source of similar or greater size would be necessary to investigate polarization rotation (PR) and presents a steeper technological challenge. Although mm-wave polarizing grids of that size do exist, the EBEX attitude control system (ACS) places a lower elevation limit of 15˚ on telescope pointing, requiring that a calibration source at 1 km away be > 270 m above ground level. Past

experiments employing far-field calibration sources have accommodated similar altitude constraints by way of natural terrain or man-made device: Archeops mounted a modulated source on a nearby hillside while BOOMERanG suspended an unmodulated source underneath a remote-controlled blimp. Unfortunately, no appropriate terrain features exist at any location where EBEX is scheduled to be fully assembled, and the prospect of suspending a *modulated* and *polarized* source was deemed technologically prohibitive. We were therefore compelled to abandon the far-field approach in favor of an alternative with a strong heritage in ground-based astronomical instrument calibration: the artificial planet.

Our artificial planet (AP) is an adaptation of the apparatus used by MAXIPOL, modified to accommodate experiments and calibration goals specific to EBEX. Although its primary purpose is to provide coarse pre-flight beam mapping, it can also be configured as a polarized source (point or extended). In this section we describe its design, anticipated performance, and initial experimental results.

3.3.2.1 Design

The MAXIPOL AP centered around a copper-coated aluminum parabolic mirror with a 96 cm outer diameter, 18 cm-wide circular central aperture. An ~ 8" (L) x 8" (W) x 4" (H) enclosure containing a halogen lamp, chopper blade and Winston cone served as the modulated emission source and was mounted at prime focus with 3 struts. No record of the mirror's focal length could be found, so we measured it with a Microscribe coordinate measuring machine (CMM). Recording 20 surface coordinates across the diameter of the mirror and fitting to the parabolic equation $f = x^2/4y$, we determined the focal length to be 89 ± 1 cm.

The MAXIPOL prime focus design is sufficient for beam mapping, but we suspected that diffraction from the source enclosure and odd number of struts along the optical path to EBEX would introduce polarization effects difficult to account for if using this device to assess IP and PR. We therefore adopted only the primary mirror from the MAXIPOL AP and converted from prime focus to a classical Cassegrain design for EBEX. This change places a spherically symmetric secondary mirror in the path of the outgoing beam instead of an asymmetric enclosure box, theoretically eliminating the diffraction-related PR expected from the latter.

Diffraction around struts is also known as a potential source of PR in certain antenna geometries. By symmetry arguments alone we expect complete cancellation of polarized diffraction effects in the modulated AP signal if using an equally spaced, even number of struts

instead of an odd number. Therefore we mount the secondary mirror with four struts instead of the three employed in the MAXIPOL configuration. This reasoning is corroborated by theoretical analyses of antenna strut geometry and polarization [39]. Not only is cross-polarization a factor of 10 lower for an otherwise identical antenna that has four struts instead of three, but given the geometry of our AP the equations predict the presence of any polarization at no greater than -50 dB compared to the main beam. This value implies that the AP signal should be unpolarized to a level of 0.01% when operated in its unpolarized configuration (assuming the modulated source itself is similarly unpolarized), which is a factor of 5 below our criterion of 0.05%.

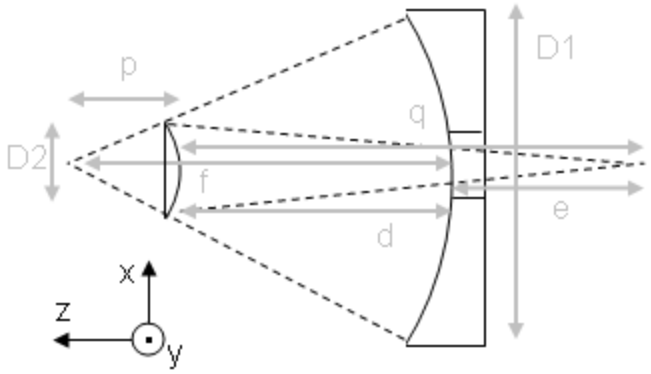

D1	96 cm
R1	89 cm
K1	-1
D2	25 cm
R2	58.7 cm
K2	-2.78
f	89 cm
e	20 cm
d	68 cm
p	22 cm
q	88 cm

Figure 3.10: EBEX artificial planet Cassegrain telescope design. R1 and R2 are radii of curvature for primary and secondary mirror, respectively. K1 and K2 are conic constants. Effective focal length is *f1* * *m* = 356 cm.

The Cassegrain design parameters are shown in Figure 3.10. With *D1*, *R1*, and *f* already known (MAXIPOL primary), *e* remained the only free parameter. Defining *e* = 20 cm was an arbitrary choice based on mechanical feasibility, simply representing a reasonable distance at which to mount a chopped mm-wave source behind the primary mirror. The hyperbolic secondary mirror design parameters are found with

$$R2 = \frac{2pM}{M-1} \text{ and } K2 = \frac{-4M}{(M-1)^2} \qquad (3.5) \text{ and } (3.6)$$

where *R2* is the radius of curvature, *K2* is the conic constant, and *M* is the magnification of the instrument *M* = *q*/*p* [45]. The secondary was cut on a milling machine to surface rms < $\lambda_{min}/20$, then hand-polished to near optical quality for alignment purposes. The secondary mount assembly was designed and built in-house with a 3-axis spring-based mechanism for fine tilt

control, ensuring the secondary is parallel with the primary in the x-y plane to within 0.05˚. The struts are hollow aluminum tubes with 1/16”wall thickness and 5/8” outer diameter. Slots cut near one end of each strut provide coupling to the secondary mount assembly along with coarse position control in the z-direction (± 1 mm). Struts are fastened to the outer edge of the primary mirror by individual mounting blocks, each with a hole cut at the appropriate angle (~27˚ from horizontal) and fitted with a set screw to hold the strut in place. From the nominal design values we can derive the parameters summarized in Table 3.4 which drive our choice of source aperture size (based on plate scale) and alignment procedure (positioning tolerance) [40].

Table 3.4: Artificial planet performance and tolerance parameters; *q*, *p* and *R2* refer to dimensions shown in Fig. 4.10. Effectively, *dq/dR2* = -4.5 means that an error in machining the radius of curvature of the secondary mirror by ±1 mm will place the focus of the AP at z = ± 4.5 mm from its expected position. We have measured *R2* and confirmed it meets spec to within ± 0.1 mm. *dq/dp* = 16 implies that a secondary mirror positioning error of ±1 mm will offset the focal plane by z = ±16 mm.

Parameter	Equation	Value
Plate scale	$s = 1/f_{eff}$	**9.5 arcmin/cm**
Defocus tolerance (as a function of R2)	$dq/dR2 = \frac{p}{R2-2p} - \frac{p \cdot R2}{(R2-2p)^2}$	**- 4.5**
Defocus tolerance (as a function of p)	$dq/dp = \frac{R2^2}{4p^2 - 4pR2 + R2^2}$	**16**

In an effort assess the validity of our AP design, we investigated optical coupling between the AP and EBEX telescopes through simulation in Code V. In the limit of ray optics as shown in Figure 3.11, EBEX responds identically to the AP beam as it would a point source on the sky. We place a 1300 K laboratory blackbody source chopped with an aluminum blade at the AP focal plane to provide a bright modulated signal at the focal plane. Mechanically, we constructed a box from 1” x 1” aluminum beams to secure our source, chopper, and control electronics to the back side of the primary as pictured in the right panel of Figure 3.12. The blackbody source has a dial on the front allowing us to control the aperture diameter between 0.1” and 1.0”, which, given the AP plate scale, corresponds to an angular span of 2.4 to 24 arcminutes in the EBEX focal plane.

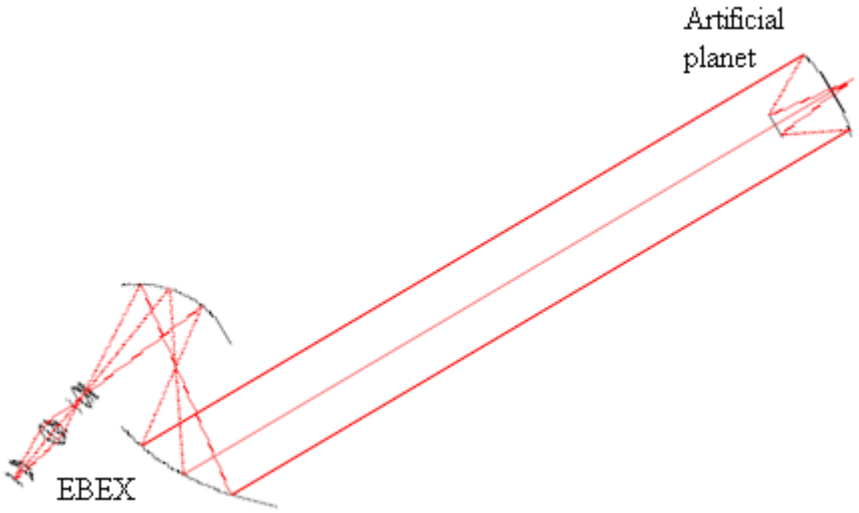

Figure 3.11: Code V simulation of AP coupling with EBEX. Separation assumed is 10m based on anticipated distance available in high bay facilities where integration and calibration most likely to occur.

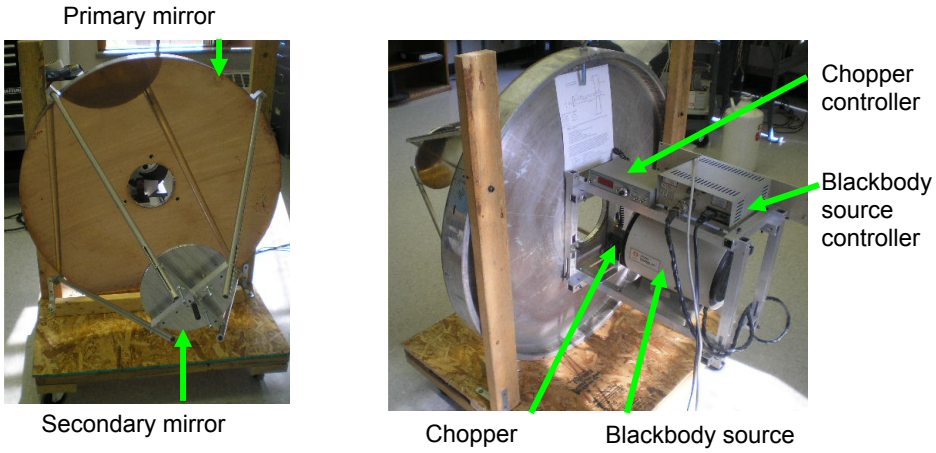

Figure 3.12: Preliminary configuration of EBEX artificial planet as used at Nevis Lab, Dec 2008.

3.3.2.2 Preliminary Experimental Results

EBEX was fully integrated for the first time in Nov 2008 at Columbia University's Nevis Lab in Irvington, NY. An initial attempt at beam mapping was executed in this facility which we summarize here for comparison with results from similar testing performed in May 2009 prior to the NA test flight (Sec. 4.5). At Nevis the AP was mounted on the railing of a balcony approximately 8 m above the floor and at an elevation angle of ~20˚ to the gondola. A calibrator

scan was performed with an azimuth throw of 5˚, azimuth slew rate of 0.4˚/sec, elevation throw of 2˚, and 2’ elevation steps taken after every scan (one scan = once down and back) . The AP modulated signal was measured by several 250 GHz bolometers at high S/N in both the time and frequency domains (the 250 GHz wafer was the only one installed on the focal plane during this exercise). Several more scans were executed with the AP blackbody source aperture adjusted to various diameters between 1.0 and 0.2 inches. Contrary to expectations, the magnitude of the signal remained consistent regardless of aperture size. Furthermore, the temporal extent and shape of the modulated signal convolved with the known azimuth slew rate implied a beam FWHM on the order of 2˚; 15x greater than the expected 8’.

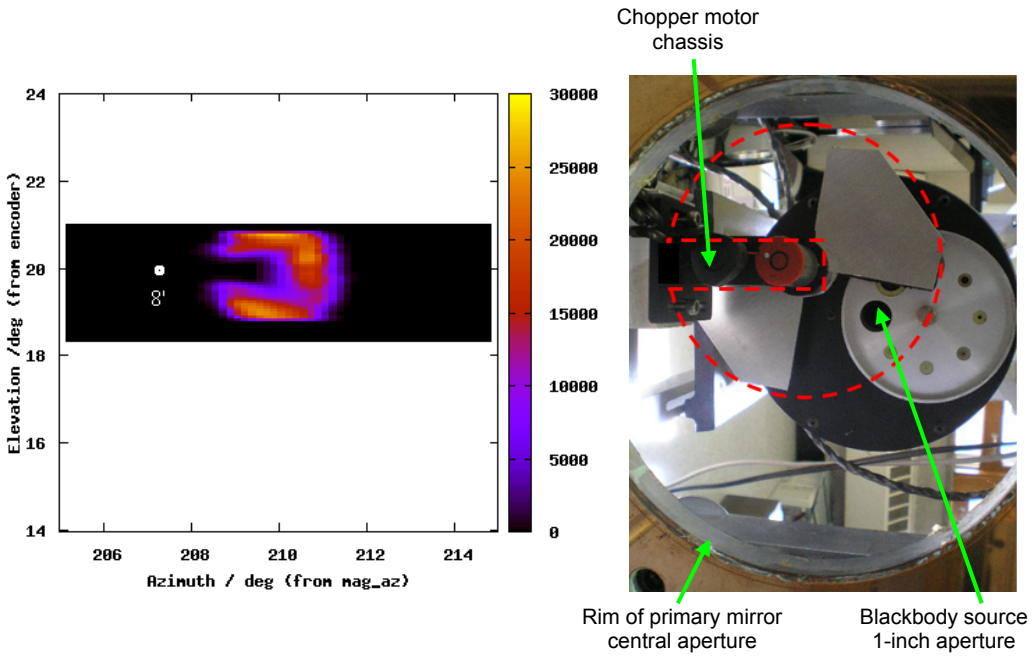

Figure 3.13: Left – Example beam map from data collected at Nevis Lab, December 2008. To scale, white circle represents footprint of expected 8’ FWHM beam. Right – Pictorial description of *pac-man* model. Model posits that although intended to only cover the extent of the 1-inch-wide blackbody aperture, modulated signal is measured in EBEX focal plane across entire 6-inch-wide area highlighted by red dashed line.

The bolometer and pointing TOD were then binned in azimuth and elevation to generate beam maps for six different detectors. All six gave nearly identical and initially inexplicable results, a representative example of which is shown in the left panel of Fig. 3.13. We soon developed a model to explain the ~2.5˚ *pac-man* beams: with the chopper exposed, the EBEX

beam was convolved over a modulated source not only spanning the intended ≤ 1-inch-wide blackbody aperture, but over the entire area covered by the spinning blade.

This *pac-man model* rectifies two key features: (1) the *mouth* is well-explained as the area where the modulated signal was blocked by the chopper motor chassis, and (2) the ~2.5˚ angular diameter of the image is consistent with the AP plate scale and physical diameter of the chopper blade $\left(9.5'/cm \cdot 16.5cm = 2.6^{\circ}\right)$.

Having attributed the erroneous results to our design blunder, we modified the AP payload to hide the blade behind a plate except for a small adjustable aperture at the focal point as shown in Fig. 3.15. However, we explored a technique to extract at least a rough estimate of the beam width from the pac-man data. The top and bottom edges of the mouth are hypothetically generated by a convolution of the EBEX beam with an approximately sharp edge. Though not perfectly sharp because the motor chassis was offset from the focal plane by ~ 5 cm, we can analyze the shape of the beam map in vicinity of the edges to hypothetically place an upper limit on the EBEX beam width.

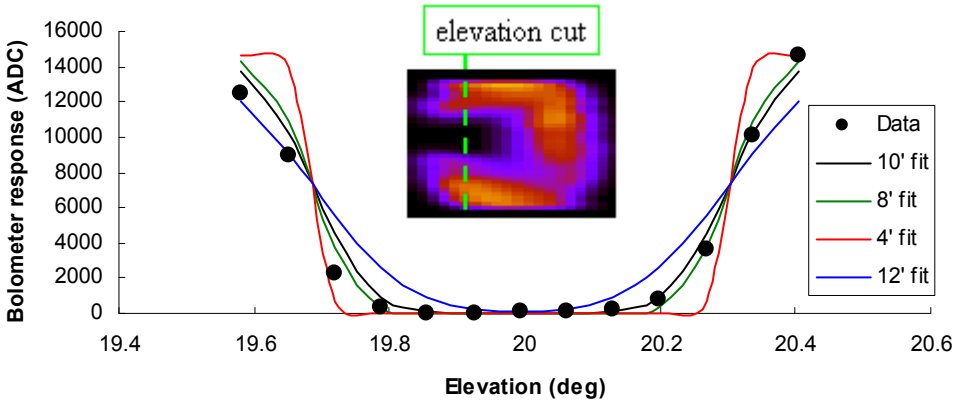

Figure 3.14: Elevation cut across Nevis pac-man beam map (data) with best-fit beam FWHM derived by convolving theoretical Gaussian beams of varying FWHM with sharp edge (analytical results = solid lines). Best fit FWHM = 9' ± 1'.

We took a simple elevation cut at an azimuth of 209˚. Assuming a perfectly sharp edge and fitting for the FWHM of the convolved Gaussian beam, we found the best fit is 9' ± 1' (Fig. 3.14). As an upper limit and essentially consistent with the expected beam width, this implies no major misalignment or other anomalies in the EBEX optical system. Although unintended, this exercise may reveal a new and potentially useful approach to beam mapping. One could imagine

intentionally placing an aperture with sharp edge(s) at the focal plane of the AP instead of the traditional small circular aperture (point source). With a cross-shaped aperture, for example, the presence of both horizontal and vertical edges would allow an analysis of FWHM in two dimensions with a single data set. The point source approach is of course superior as it reveals the full 2-D beam shape, but is seemingly more susceptible to misinterpretation as a function of greater sensitivity to AP misalignment and pointing anomalies. This relatively less demanding sharp edge technique may therefore serve a role in providing a first-look or as a consistency check on point source results.

Applying our lessons learned at Nevis, we moved the aperture selector dial from the blackbody source to an aluminum plate which is placed in *front* of the chopper. The new design is pictured in Fig. 3.15. This was the configuration used for ground-based beam mapping at Ft Sumner in May 2009 which is discussed in Sec. 4.4.

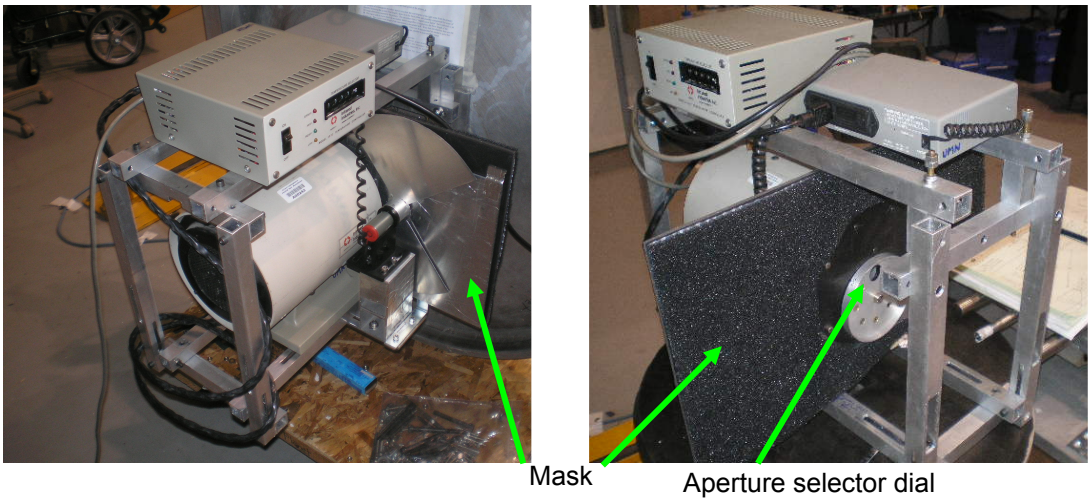

Figure 3.15: Modified artificial planet design; chopper now hidden behind eccosorb-covered plate (mask).

4 Ground-Based Calibration: Experiments & Results

4.1 Introduction

In this chapter, the experiments listed in Table 3.1 are explained in greater detail and we report preliminary results obtained during our initial attempt at a comprehensive ground-based calibration of EBEX performed at the Columbia Scientific Balloon Facility (CSBF) in Ft Sumner, NM from 17 Apr – 28 May 2009. The calibration tests were executed as the instrument was being assembled and integrated in preparation for the North American (NA) test flight, which took place 11 Jun 2009 and is addressed in Chapter 5. The NA test flight goals did not demand the instrument possess all the functionalities proposed for the LDB mission, and many upgrades will be accomplished between the test flight and Antarctic campaign. Listed here are the most noteworthy aspects of the NA configuration based on their impact to calibration:

- Only a minor subset of the cryogenic optical elements were anti-reflection (AR)-coated; all will be AR-coated prior to the LDB flight. This change will have a significant impact on many of the systematic effects discussed in this chapter, most notably instrumental polarization (IP) and optical efficiency (OE).

- ~200 bolometers of the planned 1,440 were operational, occupying portions of 3 of the planned 14 wafers, located on 1 of the 2 planned focal planes (the H plane). Furthermore, bolometer fabrication is a work in progress - no wafers made to this point have fully satisfied EBEX specifications for heat capacity and thermal conductivity. All will be replaced before Antarctica.

- The AHWP, installed in the cryostat for the first time, had no provision for absolute positional encoding referenced to the cryostat or any other coordinate system. Absolute polarization rotation and IP orientation angle are indeterminable without this capability which should be added in the near future.

Given the status of the instrument, the full complement of experiments accomplished in Ft Sumner must be repeated before the Antarctic campaign since the results discussed here will be largely if not wholly inapplicable to the telescope in its LDB configuration. Therefore, the New Mexico experience serves mainly as a calibration pathfinding exercise, in rare cases assessing important instrumental characteristics expected to change little before LDB, but of primary use in identifying experimental successes, failures, oversights and potential procedural improvements. Note that all results discussed in this chapter are properly classified as *preliminary*, due primarily to the brief temporal separation between the data collection and composition of this thesis. The analysis effort is in progress and includes an ongoing development of analytical tools unique to EBEX calibration which will undoubtedly be used in future months to corroborate some conclusions proposed below, modify others, and completely undermine still others.

Chapter 4 is organized according to individual systematic effects and follows this basic outline: phenomenological explanation, experimental procedure, results and conclusions. In some cases we posit ideas for improvement at the end of the section, while more global lessons learned are reserved for the end of the chapter (Sec. 4.10).

A thorough understanding of optical design and bolometer functionality proved critical during the calibration effort in New Mexico, will be essential for achieving greater operational efficiency in future campaigns, and is generally applicable throughout many parts of this chapter. Working from the bottom of the cryostat outward to the CMB, the left panel of Fig. 4.1 provides an overview of the three wafers installed during the NA campaign along with our chosen cryostat coordinate system. The right panel shows the wafers in more detail, highlighting the classifications of bolometers wired up for flight. Classification describes the configuration of each individual feedhorn: *open* bolometers had unobstructed feedhorns (i.e., open to light), *eccosorb* indicates those which had a pyramidal plug made of eccosorb MF110 inserted in the feedhorn to provide ~ 98% attenuation (intended to prevent saturation during ground-based experimentation), and *dark* bolometers were covered with a piece of aluminum tape to hypothetically block *all* light (which we quickly discovered was not entirely effective). In Fig. 4.2 we depict the projection of the focal plane at two key points: at the cryostat window (which is just a few cm above an image plane at the field lens), and on the sky.

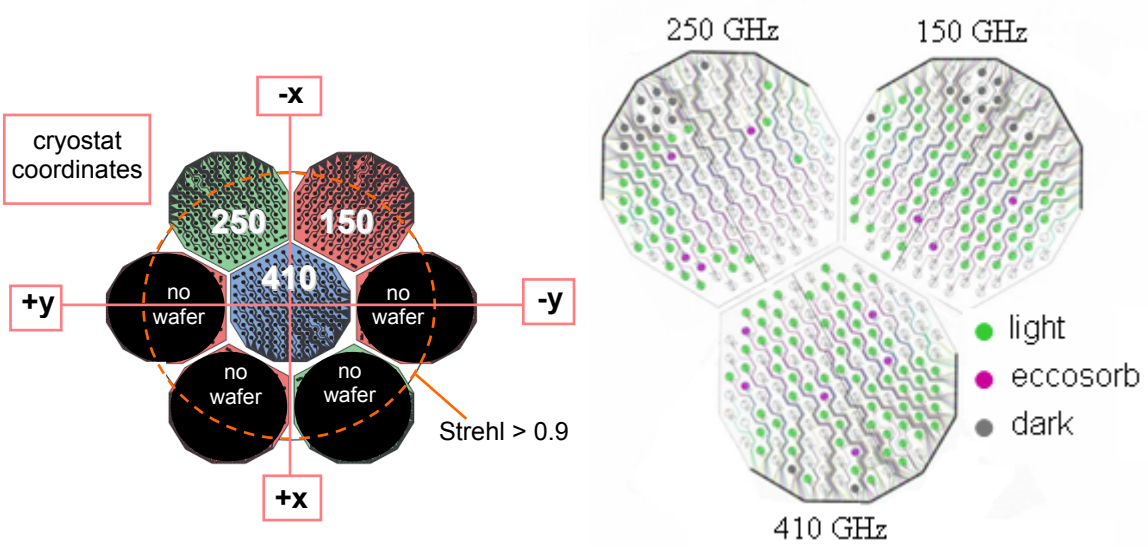

Figure 4.1: NA wafer configuration as viewed looking down on the focal plane (e.g, from the top of the cryostat). The plate scale here is slightly dependent on position (x and y), but on average is ~ 18.0'/cm. The average plate scale of the focal plane when projected on the cryostat window is ~ 17.7'/cm.

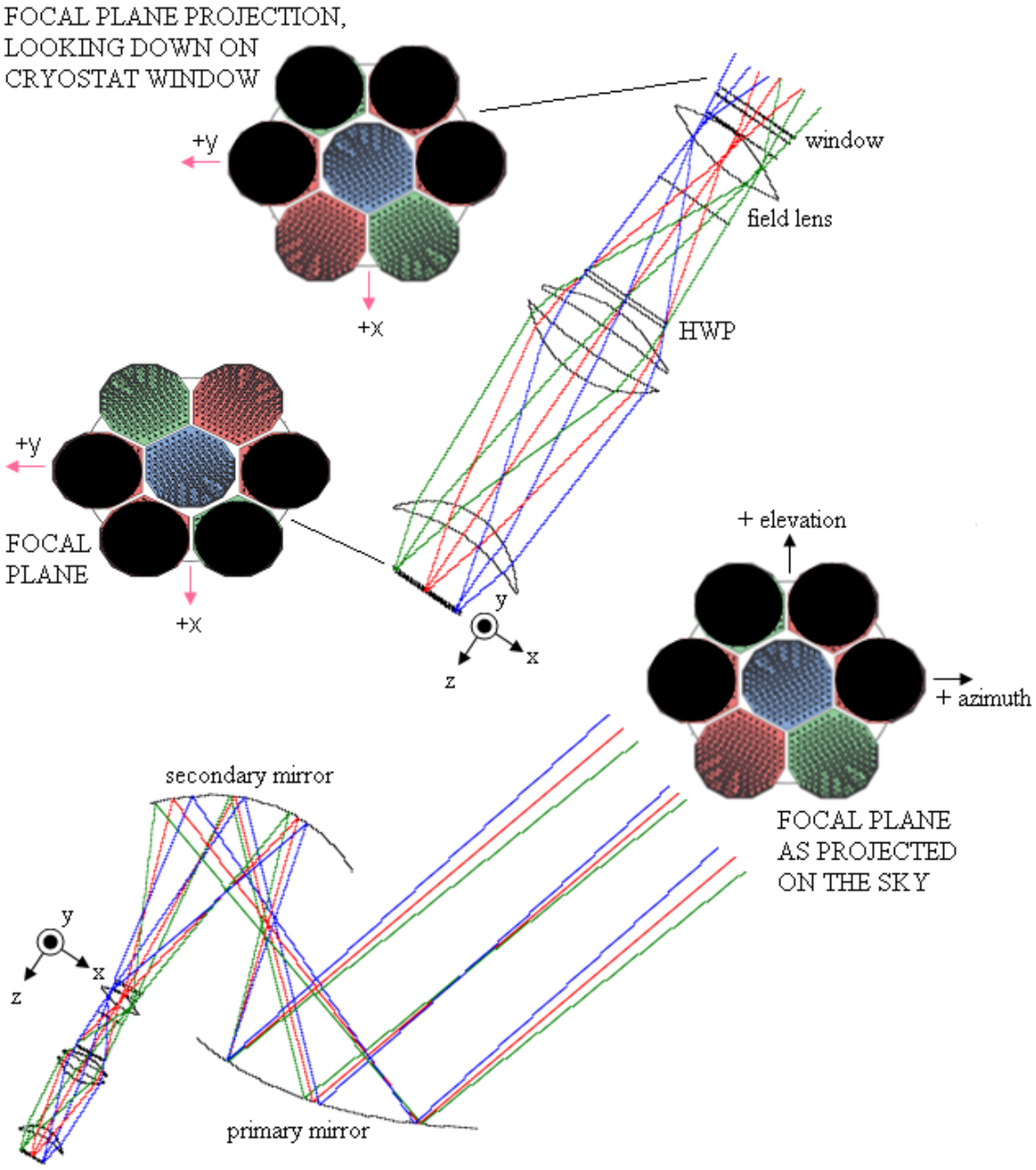

Figure 4.2: Focal plane projections at key points in the optical path. Beam colors are *not* related to or correlated with wafer colors. For clarity, an example: imagine a stationary point source on the sky. If the source is located at a higher elevation than the focal plane FOV and we slew the gondola straight up in (i.e., in the direction of + elevation); the source will first come into view of the 410 GHz wafer, followed by the 150 GHz wafer (or 250 GHz wafer, depending on the source's azimuth position). Then imagine we point the gondola so the 150 and 250 GHz wafers sit at the same elevation as the source. If we then slew the gondola from left to right (i.e., in the + azimuth direction), the source will first be seen by the 250 GHZ wafer, followed by the 150 GHz wafer.

4.2 Optical Efficiency

The instrument's optical efficiency indicates what fraction of flux incident on the telescope produces signal at the focal plane. For EBEX, since the two mirrors are virtually lossless, it essentially describes how many photons are discarded (absorbed or reflected) en route from the cryostat window to the bolometers. For this reason and because devising a way to test this effect on the integrated telescope presents a significant technical challenge, we perform the experiment described below on the cryostat alone. Optical efficiency has significant implications for our science goals - every polarized photon lost between the primary mirror and focal plane weakens our leverage on the primordial B-mode signal and increases the uncertainties in our other anticipated results. We can assess this quotient experimentally by illuminating the cryostat with two mm-wave sources of different but well-characterized magnitude, in our case a 273 K blackbody vs. a 298 K blackbody. For each detector we record the difference in *measured* power under the two loads (ΔP_m) and then compare this value to the *known* difference in power incident at the window assuming spectral and antenna response models (ΔP_i).

We mounted a large polystyrene container lined with eccosorb CV-3 (egg crate) submerged in ice water ~15 cm above and overfilling the cryostat window as illustrated in Fig. 4.3. Under this 273 K 'cold load' we recorded ~ 30 seconds of bolometer data. Another 30 seconds were recorded after placing a window-filling piece of CV-3 underneath the polystyrene container, providing a 'warm load' measured with a thermocouple at 298 K.

The container was initially filled with LN_2, but we discovered that the load variation between 77K and 298 K exceeded the available linear dynamic range of the bolometers. This non-linearity was identified by flashing a set of LEDs inside the cryostat, once with the 77K load and once with the 298 K load. The magnitude of the response should be consistent during the two flashes if the detectors are operating within their linear regime. However, we saw an obvious discrepancy. Repeating the procedure at 273 K and 298 K after re-tuning the bolometers, the response appeared nominally equivalent between the two flashes for most of the detectors being viewed in real-time.

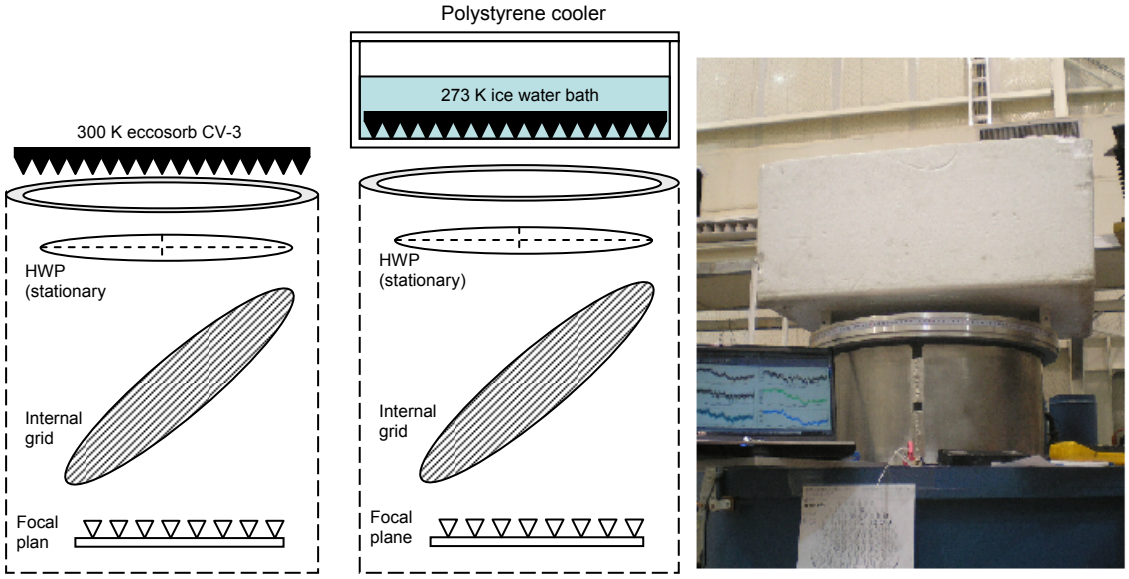

Figure 4.3: Optical efficiency experiment. Conceptual design showing both steps – (1, left) illuminating detectors with warm load and (2. middle) cold load. Right – Implementation in high bay at CSBF, Ft Sumner.

A thorough discussion of the following analysis is presented by Hubmayr in [42]; we briefly summarize the methodology and results here. Converting ADC to Watts, ΔP_m was calculated for each bolometer. 120 of the 196 operational bolometers were then eliminated from consideration due to evidence of saturation or non-linearity (the latter surmised if the LED flash response varied by > 10% under the two different external loads). This left 76 for analysis: 7 on the 150 GHz wafer, 8 at 250 GHz, and 61 at 410 GHz. ΔP_i is estimated by integrating the Planck function for each loading condition (T = 273 K, 298 K), assuming a top hat spectral response model (133-173, 217-288, and 366-450 GHz) and multiplying by the assumed antenna response, $A\Omega \sim \lambda^2$. Using this approach, ΔP_i = 29, 50 and 58 pW for the 150, 250 and 410 GHz bands, respectively. The optical efficiency for each bolometer is then calculated as $\Delta P_m/\Delta P_i$. Hubmayr provides a histogram for each class of bolometer (light, dark, eccosorb-plugged), highlighting the fact that there is an apparently random distribution of results within each class except for the 410 GHz bolometers open to light (which show evidence of being normally distributed, as would expect for all classes given a sufficient sample size). Taking a simple average for all open bolometers, the results imply optical efficiencies of 5.4, 0.5 and 0.5 % for the 150, 250 and 410 GHz bands, respectively.

These diminutive values inspired a more rigorous effort to calculate the expected optical efficiency given the NA cryostat configuration. This exercise basically involves quantifying radiation loss as a function of absorption and reflection in the cryostat's 16 individual optical elements. Absorption and reflection were calculated from refractive indices, loss tangents and physical properties (thickness, temperature). In some cases these were based on experimental measurements and in others on theoretical predictions. A summary of the major contributors is found in Table 4.1.

Table 4.1: Approximation of cryogenic transmission expected during NA campaign. Column labeled *eccosorb film* refers to a pair of thin MF110 sheets mounted above the 250 and 410 GHz wafers, installed based on pre-flight calculations implying bolometers in these channels may be in danger of saturation.

Band	LPFs	Teflon filter	UHMWPE (window, lenses)	AHWP	Polarizing grid	eccosorb film	bolometer coupling	TOTAL
150	0.64	0.91	0.65	0.58	0.5	N/A	0.5	**6%**
250	0.65	0.88	0.63	0.57	0.5	0.75	0.5	**4%**
410	0.63	0.86	0.62	0.57	0.5	0.75	0.5	**4%**

A comprehensive explanation remains elusive for why theory and measurement seem consistent for the 150 GHz channel but diverge by nearly an order of magnitude for the other two bands. We suspect that some combination of the following factors may contribute to these results:

Bolometer coupling – 50% efficiency for all bands is probably optimistic considering the current maturity of the wafer design and manufacturing process. This value could easily be 2x lower, possibly even below 10%, and almost certainly varies from wafer to wafer, perhaps even detector to detector (although the latter is likely a small effect). If we have accurately assessed the losses in all the other elements, consistency between theory and measurement in all bands could be achieved with bolometer coupling values of 45, 6, and 6% (150, 250, 410 GHz). Independently testing for this factor before installing wafers in the EBEX cryostat would be a useful addition to the pre-flight bolometer characterization pipeline.

Cold load – If the eccosorb CV-3 hadn't yet thermalized with the ice water bath inside the polystyrene cooler and was actually warmer than 273 K, our calculations of input power would overestimate ΔP_i . This would cause our optical efficiency results to be lower than their true

values. When executing this experiment, approximately 20 minutes transpired between filling ice water and taking measurements. With no data available on the pertinent thermal properties of eccosorb CV-3 it is difficult to quantify the potential magnitude of this effect. A temperature sensor should be embedded in the ice water eccosorb during future iterations of this experiment. Another influence (if present) is liquid water condensing on the bottom surface of the cooler; this too would make the cold load appear warmer than 273 K from the cryostat's perspective. We had a fan blowing across this surface in an attempt to mitigate the effect, but have little means for measuring success beyond visual inspection (no noticeable condensation was observed). It is also true that polystyrene is not perfectly transparent to mm-waves. A variety of absorption values in the EBEX bands can be assumed from the materials data found in [43], although a reasonable band-averaged mean seems to be ~3% per cm of thickness. At 3.8 cm thick we would therefore expect ~ 11% absorption in the bottom wall, rendering the cold load ~ 11% warmer than assumed in our calculations above. The overarching problem with using cold load uncertainty to explain our results is that this effect should impact all bands more or less equally and we see a significant inconsistency between the 150 GHz band and the 250/410 GHZ bands.

AΩ – As mentioned previously, the Lyot stop at the AHWP truncates what would otherwise be Gaussian beams for each bolometer. Therefore, assuming $A\Omega \sim \lambda^2$ overestimates the beams at the window and artificially inflates ΔP_i. However, we estimate this effect to be negligible in the higher frequency channels and only on the order of 20% at 150 GHz.

The basic experimental method described here has been used on many occasions preceding EBEX and should be considered reliable for future implementation. A more conscious effort to control and monitor cold load temperature may be advisable, as well as a more robust approach to preventing condensation on the bottom of the cooler. Another marginal advantage may be realized if the cold load is chopped at a constant frequency with a 300 K window-filling blade, as this would mitigate any low-frequency response drift.

4.3 Bolometer Time Constants

The bolometer time constant (τ_b) is a measure of the thermal link between detector and bath, essentially indicating how quickly the bolometer can dump heat generated by incident

radiative flux. If bolometer *A* has a smaller τ_b than bolometer *B* but the two are otherwise identical, bolometer *A* will provide higher S/N than *B* at a given sample rate. Alternatively, *A* can be sampled at a higher rate without loss of signal (thus providing the advantage of collecting more information per unit time). For a balloon-borne polarimeter with spinning HWP, τ_b also serves as a primary driver for choosing the waveplate rotation velocity and gondola scan speed. Its value is a direct consequence of physical design, namely $\tau_b = C/G$, where *C* is the heat capacity and *G* is thermal conductance. We can also extract τ_b from an experiment where we measure response as a function of modulated input frequency,

$$R(f) = \frac{A}{\sqrt{1+\omega^2\tau^2}}, \tag{4.1}$$

where *R* is the bolometer response(either peak-to-peak in the time domain or the peak at f_{chop} in the frequency domain), $\omega = 2\pi f_{chop}$, and A is the response when $f_{chop} = 0$ (DC signal). While *C* and *G* are challenging to measure, the second option provides a straightforward way to determine τ_b with the bolometers residing in their true operational environment.

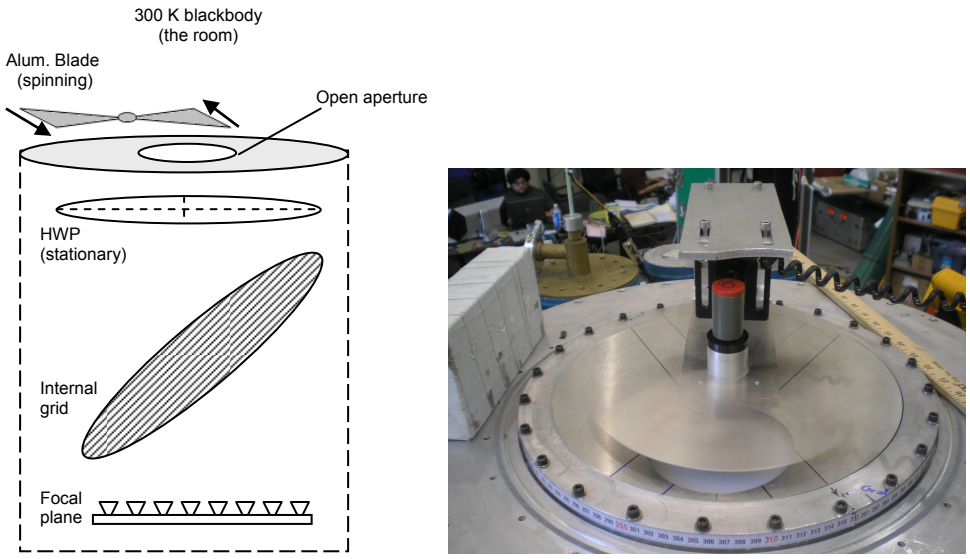

Figure 4.4: Bolometer time constant experiment. Conceptual design (left) and implementation (right).

We positioned our SRS chopper above the cryostat window, resting on an aluminum 'window mask' such that the blade spun just above the surface of the mask and fully occulted the 4-inch-wide aperture as seen in Fig. 4.4. As described in Sec. 3.3.1.1, we assume that chopping between the room with an aluminum blade provides an approximately 300 K (room) vs. 15 K

(blade) modulated optical load, a large signal easily seen in the bolometer TOD which provides even higher S/N in the frequency domain. Based on our knowledge of the focal plane as projected on the cryostat window (as captured in Fig. 4.2), we roughly aligned the mask aperture with the center of whichever wafer was being tested at the time. Though this position maximizes the signal for only those detectors located near the middle of the wafer, we anticipated from optical simulations that the beam footprint at the window would be wide enough to ensure that even those located at the outer edge would measure high S/N. This was confirmed in real-time as we observed the time domain readout for several bolometers and identified a clear modulated response at f_{chop} in each. After choosing an arbitrary representative bolometer to monitor in the kst display, we increased f_{chop} from 1.6 to ~ 60 Hz incrementally, recording the FFT peak at each step. We have plotted the data we recorded in real-time for our representative bolometers in Fig. 4.5. These plots also include a one pole fit to the data which have been used to solve for τ_b.

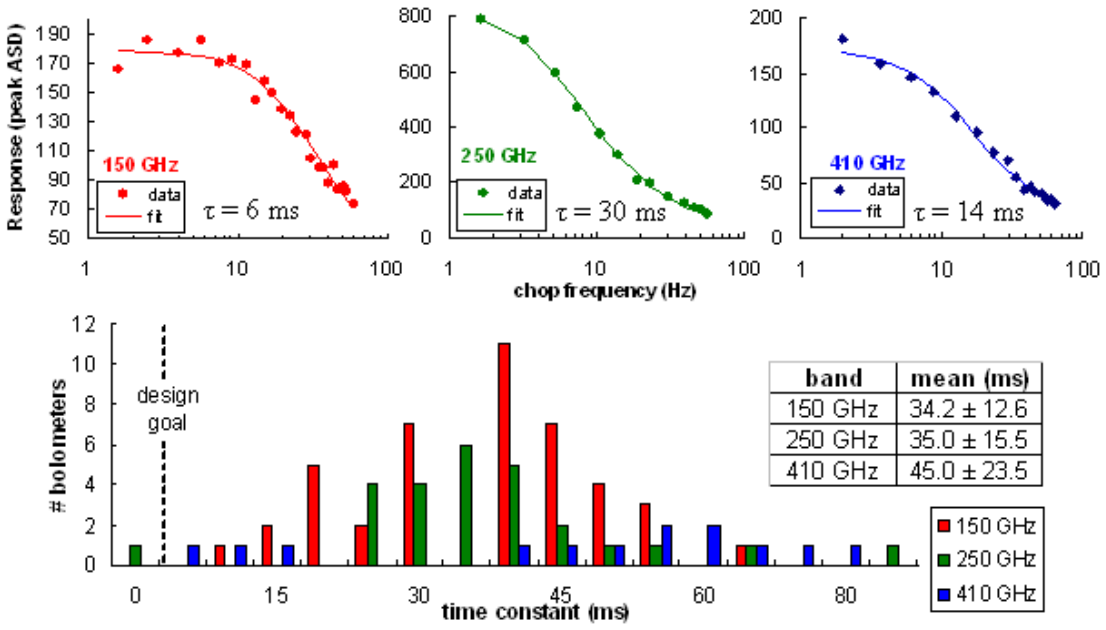

Figure 4.5: Preliminary results from bolometer time constant experiments at Ft Sumner. Top – Data collected in real-time for one detector per wafer (points), along with a one pole fit (solid line) and time constant (τ) extracted from the fit parameters. Bottom – Cumulative distribution for all bolometers deemed functional during the experiment.

Clearly our measured values for τ_b vary by wafer and are in all instances greater than the design goal of 3 ms. This is not a surprising result since the fabrication pipeline remains a

research effort at this stage; these values are a useful part of the feedback loop and we expect significant improvement before LDB. We also notice that while there is indication of a normal distribution in the 150 and 250 GHz wafers (as would be expected), the 410 GHz data are scattered. These results and their implications are discussed further in [42].

The SRS chopper motor failed when we tried to exceed $f_{chop} \sim 60$ Hz. We will most certainly want to probe beyond 60 Hz in testing bolometers with τ_b on the order of 3 ms ($f_{-3dB} = 53$ Hz), and this task will require modifying or replacing our existing hardware. This can be accomplished in one of two ways (or perhaps both): (1) construct a new blade with more fins, or (2) use a different motor. The experiment could also be made more efficient by using a window-filling blade – this way all detectors could be tested simultaneously, avoiding the need to move the mask & chopper between wafers. This would reduce the time required to perform the experiment by a factor of 7 (assuming fully populated focal planes). Given the 14" diameter of the cryostat window, this demands a blade on the order of 1 meter edge-to-edge. We constructed such a device from foamboard with a thin aluminum support bar across the middle and drove it with a 40V/15A DC motor to $f_{chop} \sim 25$ Hz before the motor failed. Blade asymmetry and drag appeared responsible for this limit, both of which could be easily overcome with a more robust design and fabrication effort.

4.4 High frequency leakage

In the NA configuration, a series of 9 filters (4 thermal, 5 LPFs) were installed between the cryostat window and focal plane to prevent radiation at frequencies above the upper edge of each band from reaching the detectors. This light is not entirely rejected but only attenuated to a certain level. At this point Table 3.1 does not contain a criterion for high-ν leakage. An effort to develop such a criterion is underway which will be based on the same benchmark used for the other effects (systematic signal ≤ IGB B-mode assuming r = 0.004). The criterion is being developed with the following framework, using the 410 GHz channel as an example: signal from $\nu > 450$ GHz reaching the detectors will be dominated by dust with unknown polarization properties; if the polarization signal from this radiation represents a non-negligible fraction of the in-band polarization signal, it will introduce error in the foreground model derived from our 410 GHz data (which is our primary channel for dust). The effect could then propagate through the

analysis pipeline into component separation at the lower frequencies and introduce error in our polarization maps, ultimately influencing our reconstruction of any potential B-mode signal.

Though we currently have no benchmark for interpreting any results from ground-based testing, we have a robust set of predictions for high-ν attenuation. Fig. 4.6 shows transmission data collected for each individual filter using an FTS at Cardiff University. The total transmission plot suggests high-ν rejection exceeding -70 dB at 600 GHz and more than -100 dB at frequencies beyond 700 GHz. This filtering scheme was developed primarily for achieving a cryogenic hold time sufficient for the long duration flight.

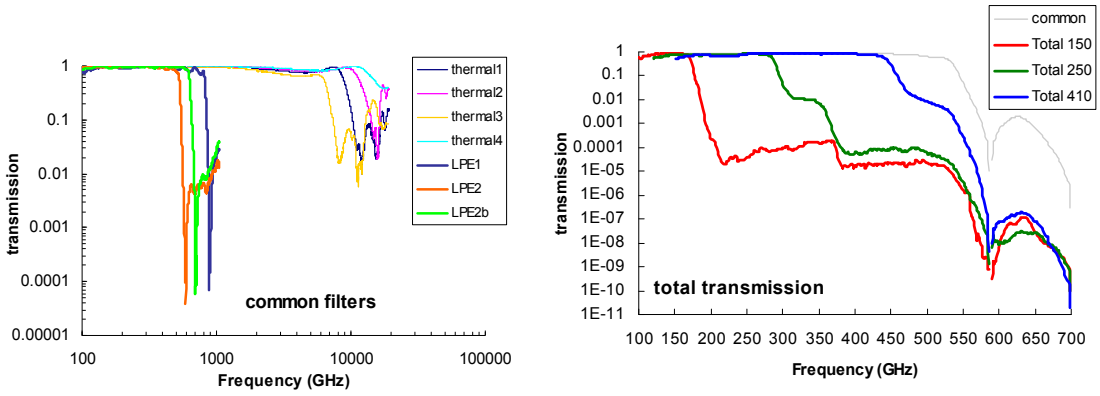

Figure 4.6: Filter transmission spectra measured at Cardiff. Left – For filters along optical path common to all bolometers. Right – Total transmission including focal plane LPFs (2 per wafer).

We have designed and executed an experiment attempting to probe high-ν leakage according to the procedure depicted in Fig. 4.7. The first step is recording bolometer response to a modulated input source visible to the instrument through a 2”-wide circular open aperture within an aluminum window mask. In this case we recorded the magnitude of the peak in the FFT at the known chop frequency, calculated in real-time over 10 seconds of bolometer TOD. We call this signal P_1. Next we installed a high-pass filter (HPF) over the aperture in the window mask, once again recording (if present) the frequency domain peak (P_2). The ratio P_2 to P_1 provides an estimate on high- ν attenuation (or an upper limit if P_2 = noise).

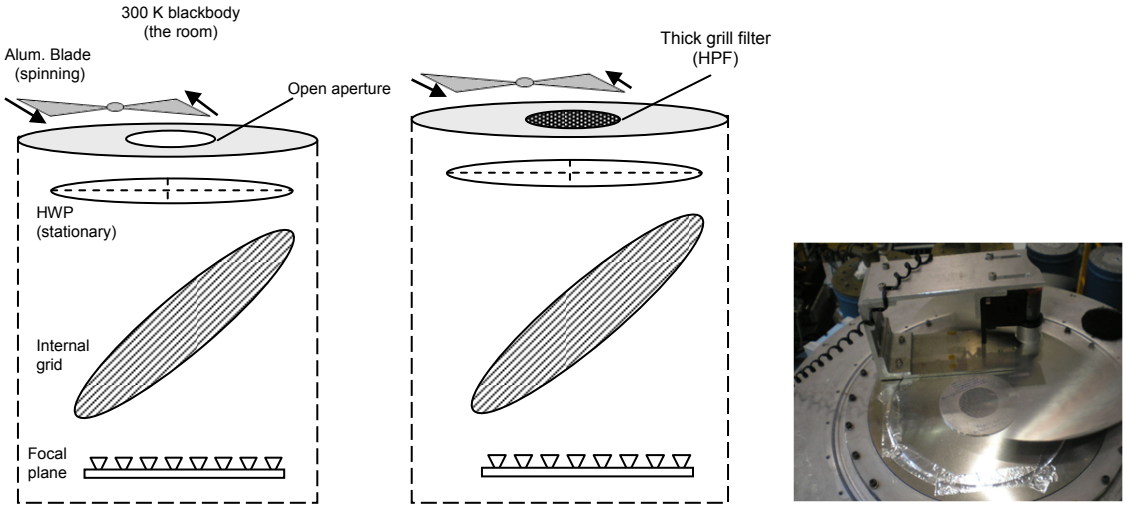

Figure 4.7: High-frequency leakage experiment, conceptual design (left) and implementation (right). Left – Step 1, measuring bolometer response with an unobstructed view of the modulated source. Middle – Step 2, measuring response (if any) with high-pass thick grill filter mounted between source and detectors.

For our HPFs, we used a set of thick grill filters (TGFs) conceptually identical to the EFM order sorters described in Sec. 3.3.1.2 but of significantly greater dimensions. In the absence of financial limitations, we would employ 14-inch-diameter window-filling TGFs to maximize P_1 and with it our lever arm on the measured attenuation level. However, we set our sights lower given budgetary constraints, and fabricated devices with a hole pattern area spanning 2 inches (10 cm) in diameter. We designed a separate filter for each band, each made of aluminum and with the design parameters shown in Fig. 4.8. Each TGF has a spectral buffer between ν_c and the canonical upper edge of the band it is intended to test. The buffer is meant to accommodate potential deviations between the hole diameter specified and hole diameters actually manufactured.

Whereas the relatively small number of holes required for the Ebert-Fastie order-sorting TGFs led us directly to traditional drilling as the preferred fabrication technique, we investigated several possible alternatives in our search for the most efficient and economical approach to making filters spanning several inches and containing thousands of holes. Seemingly viable alternatives included laser cutting, water jet, and chemical etching. The first two proved incapable of producing our desired pattern with the requisite precision and consistency, and we abandoned the etching approach after it quickly became clear that it was beyond our financial

means. So we once again turned to computer-controlled drilling, which proved effective even on this greatly expanded scale.

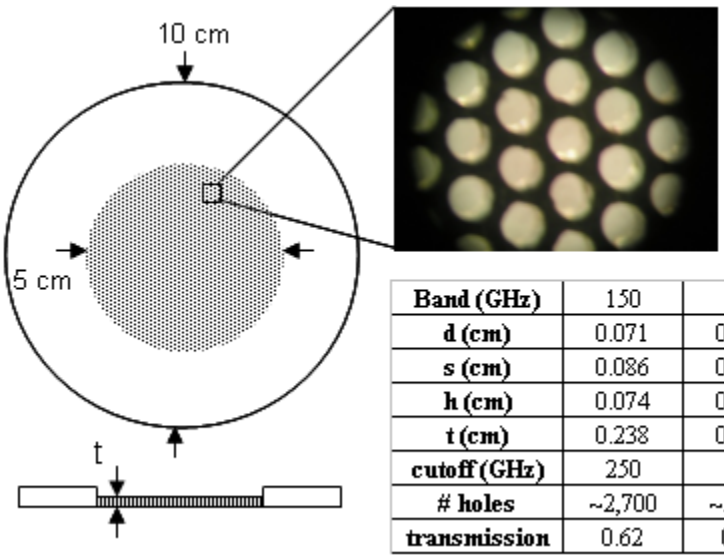

Band (GHz)	150	250	410
d (cm)	0.071	0.044	0.059
s (cm)	0.086	0.059	0.043
h (cm)	0.074	0.048	0.041
t (cm)	0.238	0.140	0.089
cutoff (GHz)	250	400	600
# holes	~2,700	~5,900	~9,700
transmission	0.62	0.50	0.34

Figure 4.8: Thick grill filter design specifications for high-ν leakage experiment. On the right is a photo of the 250 GHz TGF taken through a microscope, highlighting the effectiveness of the drilling and de-burring processes.

At 10 cm across, it was these filters that initially drove us to build the aluminum window masks mentioned in the previous and later sections. We aimed to create a single piece of hardware that would serve as a platform on which to mount the TGFs above the window while at the same time preventing modulated signal from leaking around the filter and into the cryostat.

We first aligned the mask over the center of the 150 GHz wafer as projected onto the window. In real-time we recorded P_1 at $f_{chop} \sim 8$ Hz for an arbitrary representative bolometer which we identified as measuring high S/N compared to the other bolometers displayed at the time. After inserting the TGF, we observed no signal (P_2 = noise) in the frequency domain when calculating the FFT over our standard 10 second integration. We left the chopper running with the TGF installed and recorded bolometer TOD for approximately 10 minutes. This procedure was repeated for the 250 and 410 GHz wafers. From the quick-look data (10 second FFT integration) we calculate upper limits on high-ν transmission in each band as reported in Table 4.2. These results include loss of signal during step 2 due to TGF transmission at high ν, which effectively raises the value of P_2 used in calculating the measured attenuation.

Table 4.2: Preliminary high-ν leakage results, calculated from FFT peaks over 10 seconds of integration.

band	bolometer	P_1 (ASD peak)	P_2 (ASD peak)	attenuation (dB)	transmission (% upper limit)
150 GHz	b60w3c2	170	0.1	> -30	0.1%
250 GHz	b57w0c1	22	0.1	> -20	1.0%
410 GHz	b58w0c0	32	0.1	> -20	1.0%

The values in the *attenuation* column of Tab. 4.2 represent lower limits (or equivalently, upper limits on high-ν leakage). If we analyze the full 10 minutes of data and P_2 remains buried in the noise, we could improve the limits by a factor of ~8 to around -40 dB in the 150 GHZ channel and -30 dB in the higher frequency channels. However, we have thus far been unable to locate the data that was saved electronically for all bolometers during this test which occurred 18 Apr 2009 in Ft Sumner. The following caveats, conclusions and lessons learned should be considered in preparation for future implementations of this experiment:

- The 150 GHz bolometer (b60w3c2) used in this experiment was classified as *dark*. The large magnitude of modulated signal measured in this detector implies either misclassification, leakage of signal through or around the piece of aluminum tape placed over the feedhorn, or leakage from neighboring feedhorns that were open. Since the first two possibilities seem most unlikely and the latter is cause for most concern, this issue should be investigated further with present and/or future data sets.

- If this experiment is performed in the future with a neutral density filter (NDF) temporarily installed in the cryostat to prevent bolometer saturation during ground-based testing, the transmission spectrum of the NDF must be included in data analysis. NDF attenuation typically increases as a function of frequency; failing to account for such spectral dependence would lead to a conclusion of greater instrumental high-ν attenuation than will actually exist in flight after the NDF has been removed.

- While a procedure capable of probing -100 dB is probably out of reach, there are extra measures we did not apply in Ft Sumner which could be taken to improve on the current results. Since the magnitude of P_1 directly affects our upper limit, the bolometers should be tuned for maximum responsivity immediately prior to performing this test. Furthermore, before installing the HPF, a more dedicated effort should be made to identify the bolometer with greatest S/N during step 1 (open modulated signal). Once identified, the window mask can be re-aligned directly on that beam to increase the signal even further.

- Data can be recorded over a longer integration time with the TGF in place. However, since the advantage in this arena is proportional to the square root of time, we would gain only a factor of 3.5 by integrating over 2 hours instead of 10 minutes.

4.5 Beam Mapping

In this section we discuss two experiments aimed at characterizing bolometer response as a function of angle on the sky, also known as beam mapping. The first technique is performed on the cryostat alone and theoretically provides a coarse assessment of the cryogenic optics. The second test occurs after integration and is designed to produce a preliminary 2-dimensional plot of the entire focal plane, indicating the size and shape of each beam as well as their relative angular positions on the sky. The results reported below are preliminary both because the analysis is a work in progress as well as for the fact that ground-based beam mapping has historically served as a diagnostic rather than analytical tool. Beam information derived from pre-flight tests is typically used only for identifying gross optical alignment errors; the models ultimately used in the analysis pipeline will come from scanning a bright astronomical point source in flight.

4.5.1 Cryogenic Experiment

The EBEX telescope contains 7 distinct optical elements, 5 of which are located inside the cryostat (all but the primary and secondary mirrors). Although beam shape on the sky is largely dictated by the mirrors and can only be determined after integration, a coarse assessment of the cryogenic optics can be useful as an early confirmation of proper internal assembly – or an

indication of severe misalignment early enough in the campaign to potentially do something about it.

For several compelling reasons, the EBEX optics were designed so that the beam size (i.e., angular resolution) would be constant and ~ 8 arcminutes across all 3 bands. This effectively demands that $A\Omega$ be independent of frequency. The entrance aperture widths of the conical feedhorns mounted above the focal plane are identical, therefore A is constant for all bolometers. To maintain $A\Omega$ between bands, the solid angle Ω must decrease with wavelength. In other words, the footprint of a 250 GHz beam on the primary mirror is smaller than a 150 GHz beam, and the 410 GHz footprint is smaller still. We estimate the band-dependent effective primary mirror diameter by assuming the central λ for each band and the equation for angular resolution, $\theta = 1.22\lambda/D$.

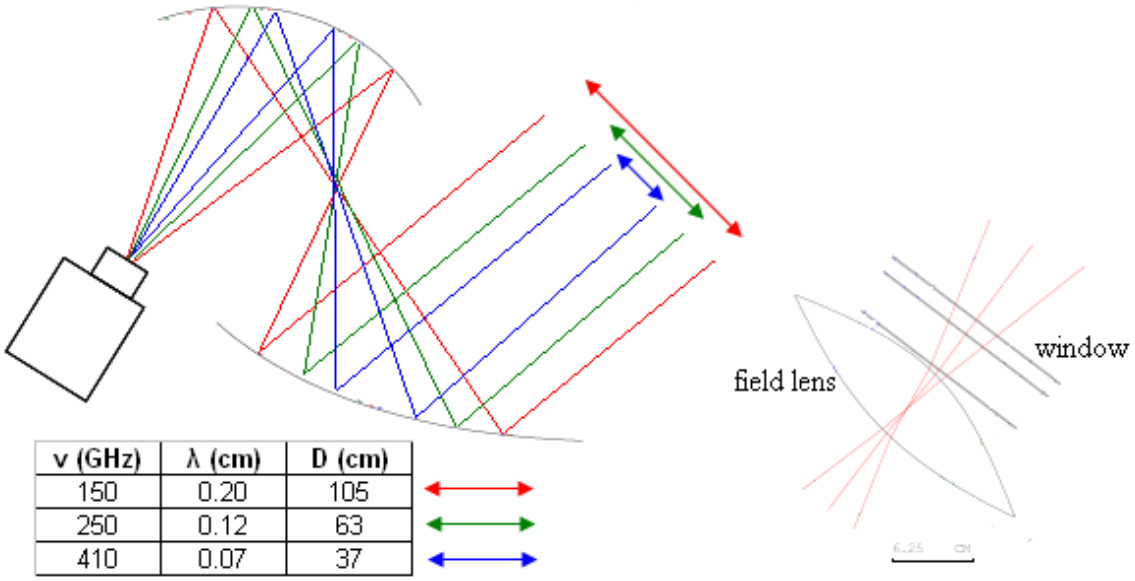

ν (GHz)	λ (cm)	D (cm)
150	0.20	105
250	0.12	63
410	0.07	37

Figure 4.9: Left - To preserve 8' resolution across all bands, 250 and 410 GHz beams underfill the primary mirror. Right – Code V simulation of 150 GHz beam FWHM at cryostat window (~6.6 cm). Scaling linearly with λ gives expected FWHM of 4.1 and 2.3 cm at 250 GHz and 410 GHz, respectively.

A variation in primary mirror fill factor necessarily implies a variation in beam width at the cryostat window. In the ray limit, our Code V model of the optical system predicts beam FWHM at the window according to the analysis described in [60]. The taper associated with of the edge rays shown in Fig. 4.9 is -7.2, -19.4, and -50.1 dB for the 150, 250 and 410 GHz beams, respectively. From these predictions and assuming Gaussian beams we can derive expected FWHM at the window: 4.3, 2.6, and 1.6 cm. In devising an experiment to probe beam width

before gondola integration we chose to perform the test at the cryostat window as a matter of mechanical convenience – it provides a flat surface at known distance from the field lens image plane without requiring the construction of additional hardware.

Two similar but distinct experimental methods were attempted and one (the latter, depicted in Fig. 4.10) proved more effective. Our first step was finding the center of the beam for our representative bolometer. This designation was bestowed on the detector with the greatest peak-to-peak signal when inserting and then removing a flat aluminum plate from over the cryostat window. We then found the beam center using our beam centering tool – a flat aluminum disk with ~4" diameter and a 1/8" hole drilled through the middle. We moved the tool around until finding the spot where signal was maximized, then used a Sharpie pen to mark the window through the tool's center hole.

Having identified the beam axis, our first method involved sequentially placing flat aluminum disks of increasing diameter on the window, each time aligning the disk on the mark made with the centering tool. As a larger and larger effective cold load occulted a greater and greater fraction of the warm background, the bolometer signal correspondingly increased (recall that higher ADC = lower mm-wave load). However, it was soon realized that for beams near the outer edge of the outer wafers (150 and 250 GHz), the larger disks soon overlapped the cryostat window clamp ring. The anticipated systematic error introduced by this complication motivated us to abandon this technique.

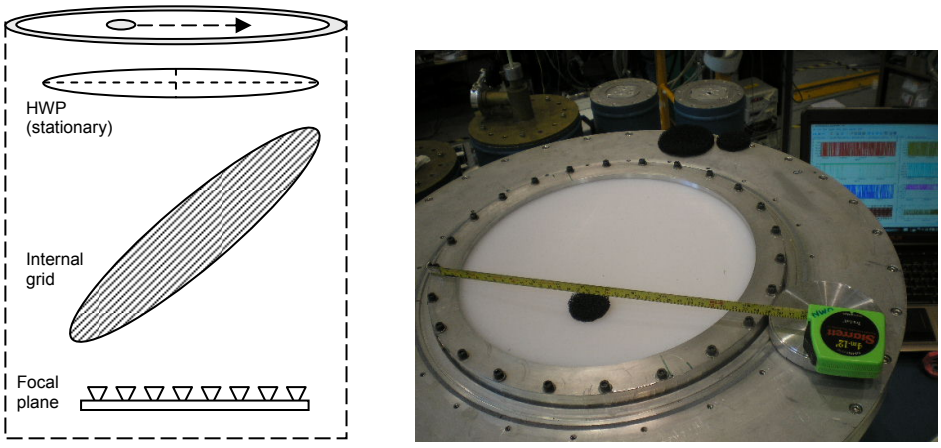

Figure 4.10: Cryogenic beam mapping experiment. Conceptual design (left) and implementation (right).

In our second attempt we used a single disk with a diameter of 1.5" (3.8 cm) and stepped it across the width of the window in ½" increments, recording the bolometer signal at each step. Again as expected, ADC increased as the disk approached the center mark and then decreased as the disk continued on to the far edge of the window. We essentially performed a convolution between the disc and the beam, with predicted and measured results for these convolutions shown in Fig. 4.11. Since the convolution is between a Gaussian (beam) and top hat function (disc), we expect a modified Gaussian for both the predicted and measured results. But the deviation from Gaussianity should be small and for simplicity we have fit these data with a pure Gaussian. Within uncertainties, the Gaussian fit is consistent with all data points in all three plots. Comparing expected vs. measured FWHM, the measured 150 GHz convolution is 20% wider than predicted, at 250 GHz the discrepancy drops to 17%, and the 410 GHz measurement is 13% smaller than expected.

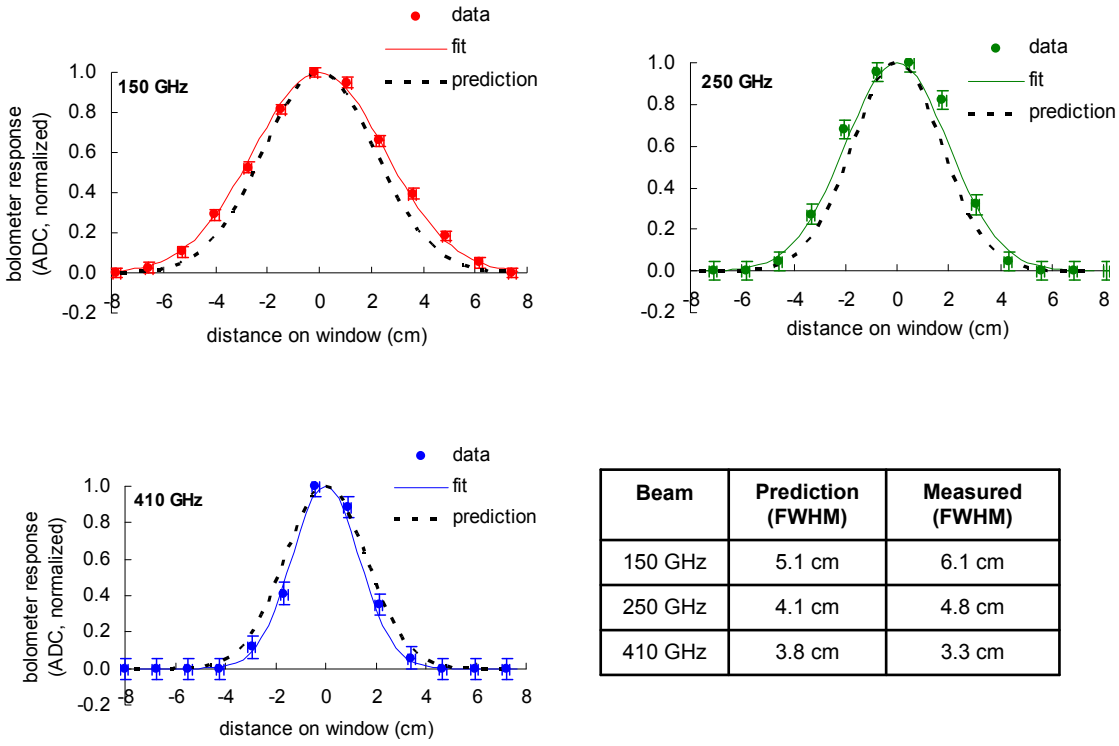

Beam	Prediction (FWHM)	Measured (FWHM)
150 GHz	5.1 cm	6.1 cm
250 GHz	4.1 cm	4.8 cm
410 GHz	3.8 cm	3.3 cm

Figure 4.11: Cryogenic beam mapping, experimental results. Fits are Gaussian, predicted FWHM at the cryostat window based on Code V simulations reported in [60].

While we do not yet have the means to make a quantitative statement about now closely the cryogenic optics matched specifications based on these results, the fact our measurements are well fit by the expected shape and agree with our FWHM predictions to within 20% implies the absence of major alignment issues. Ideas for improving this experiment for the future include:

- Using a flat reflective disc as the cold load may cause spurious reflections and hence introduce error in the data. The fact that all our data points are consistent with a Gaussian fit indicates this effect is likely minor, but replacing the aluminum surface with an absorptive material is recommended. The simplest choice would be a disc of eccosorb HR-10, which would require altering the background since the contrast in optical load between 300 K eccosorb and the 300 K room is negligible. A 273 K or 77 K background load could be implemented by mounting a polystyrene cooler above the cryostat window, lined with eccosorb in an ice water or liquid nitrogen bath. The latter is preferred to maximize S/N during the experiment.

- Use a smaller disc. The 3.8 cm version used in Ft Sumner accounted for a significant fraction of the expected convolution width at all frequencies. Because of this, the measurements became increasingly sensitive to the assumed size of the disc and less influenced by the actual beam width at the higher frequency channels.

- Devise a mechanism to ensure the disc is stepped in a straight line across the window. A wandering disc will introduce random error into the data. This could be accomplished by laying a thin string or piece of transparent tape on the window along the correct path.

- Make a second (orthogonal) cut, which will allow a 2-D assessment of the beam shape.

- Probe several bolometers on each wafer with maximum spatial dispersion. This will increase our statistical lever arm in general and reveal any dependence of beam shape on detector position in the focal plane.

4.5.2 Integrated Experiment

While the cryostat was being integrated onto the gondola, we assembled the artificial planet as pictured in Fig. 3.15. We aligned the AP secondary and focal plane aperture using our Microscribe CMM, verifying their positions within an estimated ±2 mm of design specifications (the dominant source of error was identifying the z position of the primary mirror apex which lies in empty space in the middle of the central aperture). We also verified that the plane of the secondary mirror was oriented to within 0.1˚ of parallel with the AP primary. We constructed a support structure of steel beams to hang the AP at ~ 35 feet above the high bay floor and just above the hangar doors. This location provided the greatest possible distance between the AP and EBEX given the physical constraints of the facility. The support structure and AP were assembled in place after ascending piecewise with the use of a mechanical boom lift (a.k.a. 'cherry picker'). Although initially somewhat unstable, after adding a suite of support straps this apparatus proved rigid and remained solidly perched above the doors throughout the remainder of the NA campaign.

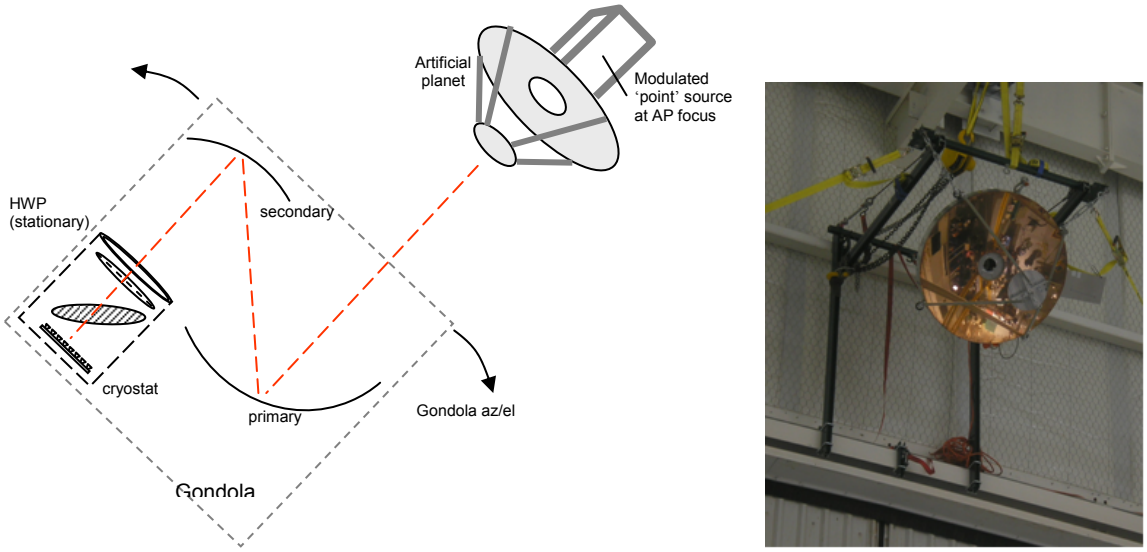

Figure 4.12: Integrated beam mapping experiment. Left - Conceptual design. Right - Artificial planet mounted in high bay at CSBF, Ft Sumner.

Beam mapping was the first integrated calibration experiment executed after gondola integration. Fig. 4.12 includes a schematic diagram of the technique and a photo of the AP as

viewed from the high bay floor in Ft Sumner. The first step was aligning EBEX with the AP. We mounted a small red pen laser to the secondary mirror mounting bracket, roughly indicating the optical axis of the planet. While hanging from the crane, the gondola was moved laterally (N/S/E/W) as well as in azimuth and elevation using ACS go-to commands until the laser beam was observed to land at or near the center of each of the 3 exposed optical elements – the primary mirror, secondary mirror, and cryostat window. We then executed a sequence of test scans to identify the orientation of the focal plane field of view relative to the AP beam. This was accomplished by viewing the bolometer and ACS data in real-time, correlating the rise and fall of modulated AP signal in the detector timestream with the associated azimuth and elevation coordinates.

Following this coarse alignment exercise, a series of calibrator scans were performed, culminating in three separate tests nominally intended to sweep over the full FOV of each wafer. A single scan is defined as encompassing a pair of azimuth sweeps (down and back), and in these experiments we stepped the elevation upward by some angle at the end of each scan. The test set-up and scan parameters are summarized in Table 4.3. The magnetometer (for azimuth) and elevation encoder were the only sensors used for pointing feedback and control during these scans.

Table 4.3: Beam mapping scan parameters (values typed in to ACS command software). Angular AP aperture width in the EBEX focal plane assumes perfect assembly and alignment.

Wafer	azimuth slew rate (deg/sec)	azimuth throw (deg)	elevation step (arcmin)	elevation throw (deg)	AP aperture width (spatial / angle in EBEX focal plane)	chopper frequency (Hz)
150 GHz	0.2	6	2’	3	½” / 5’	6.5
250 GHz	0.2	4	2’	2	½” / 5’	6.8
410 GHz	0.1	4	2’	2	¼” / 2.5’	6.8

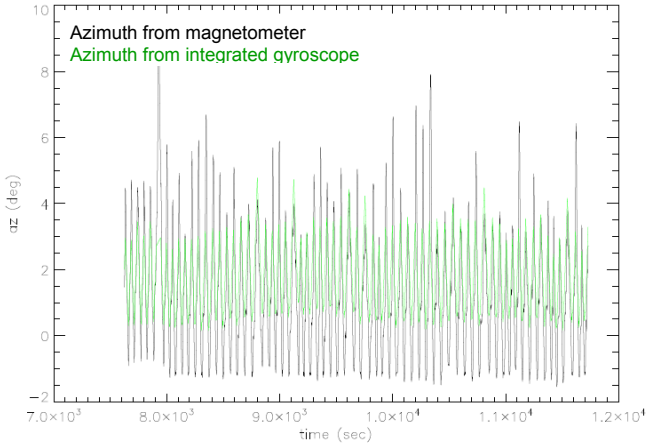

Figure 4.13: Gondola azimuth pointing during the 410 GHz beam mapping experiment as reported by the magnetometer (black) and as derived in later analysis from gyroscope data (green).

The azimuth throw was chosen to double (or triple, in the 150 GHz case) the known ~2˚ FOV of each wafer, intended to overcome an azimuth drift apparent in the ACS data. The drift appeared to exist on the order of ~2˚/hr and has been qualitatively attributed to an anomalous magnetic environment inside the high bay. Besides the magnetometer, azimuth data was recorded by the gyroscopes mounted to the gondola, which we later integrated over the length of each test to attain another (presumably more reliable) assessment of the true azimuth pointing. As shown in Fig. 4.13, the integrated gyroscope data imply that our true azimuth throw was only about half as wide as that reported by the magnetometer. And unfortunately, it was the magnetometer data that the ACS used in real-time to direct the gondola. This caused us to miss several live detectors entirely, and for several others we find that the antenna response is cut off by the scan turnarounds. Combining this effect with bolometer saturation, electrical anomalies and temporarily incapacitated readout boards, we end up with beam information for only 12 total detectors: 1 at 150 GHz, 3 at 250 GHz, and 8 at 410 GHz.

Details on the analysis can be found in [44] by Bao; here we briefly summarize her procedure pictorially in Fig. 4.14 and show a subset of preliminary results in Fig. 4.15. The beam maps shown in the latter figure were generated by binning bolometer response in azimuth and elevation based on the filtered timestream depicted in the upper right-hand panel of Fig. 4.14. The (relative) azimuth information from the integrated gyroscope data was used throughout this analysis.

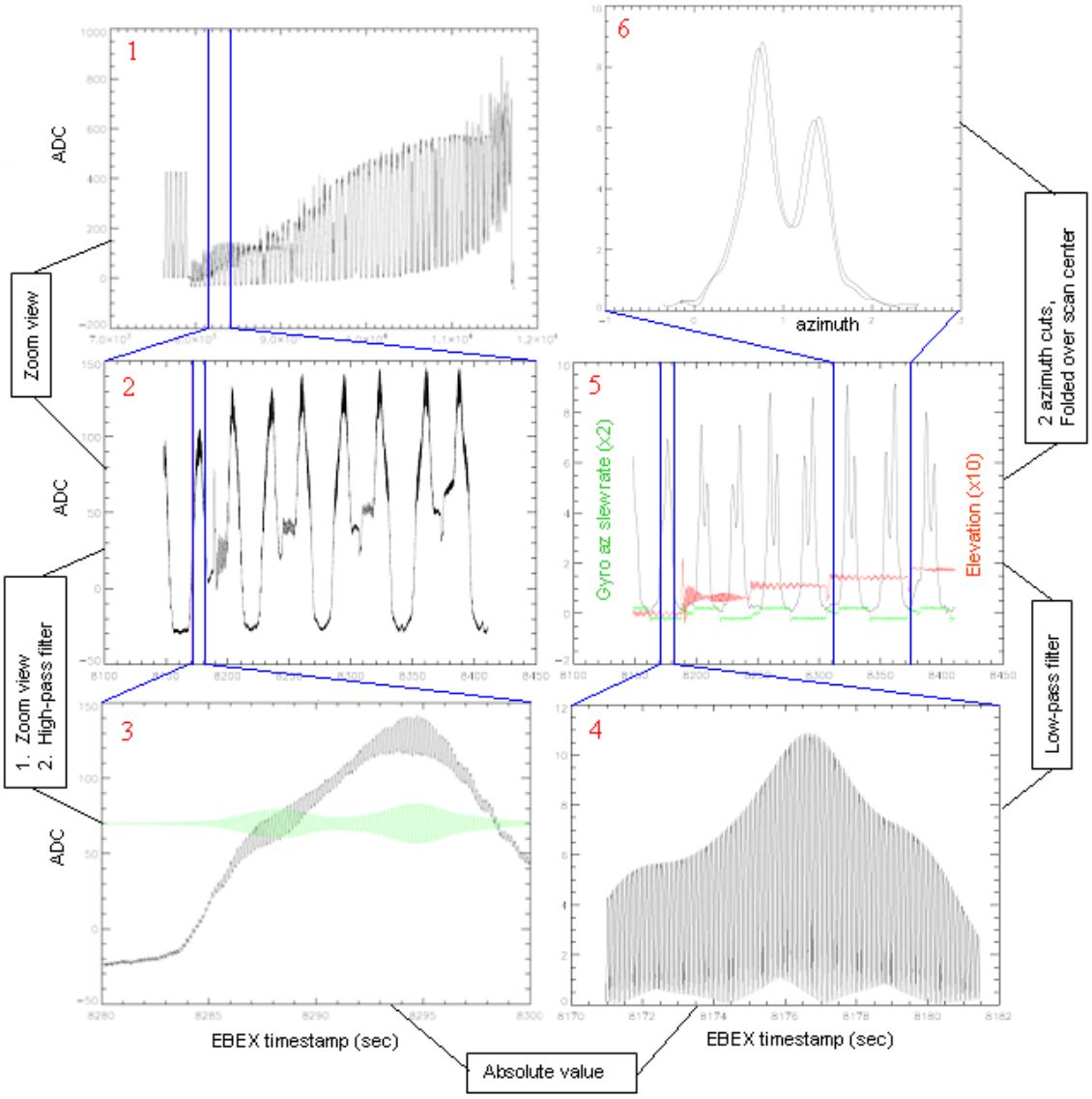

Figure 4.14: Beam mapping analysis pipeline. Panel 1 -Raw bolometer data for entire test (~1 hour). 2 – Zoomed-in view showing 4 scans, strong scan-synchronous signal attributed to structure on high bay wall behind the AP. 3 – Zoomed-in view of ½ scan showing the 6.8 Hz modulated AP signal before (black) and after (green) applying a high-pass filter in the frequency domain. 4 – A small portion of the filtered TOD after taking the absolute value. 5 – Four scans after applying a low pass filter to isolate envelope of the 6.8 Hz AP signal. Elevation (red) and azimuth slew (green) data are included to rectify gondola pointing and bolometer response. 6 – After converting the x-axis from timestamp to azimuth (deg) using gyroscope data, we fold a single scan in half to overlay the pair of spikes generated as the gondola goes down (spike #1) and back (spike #2).

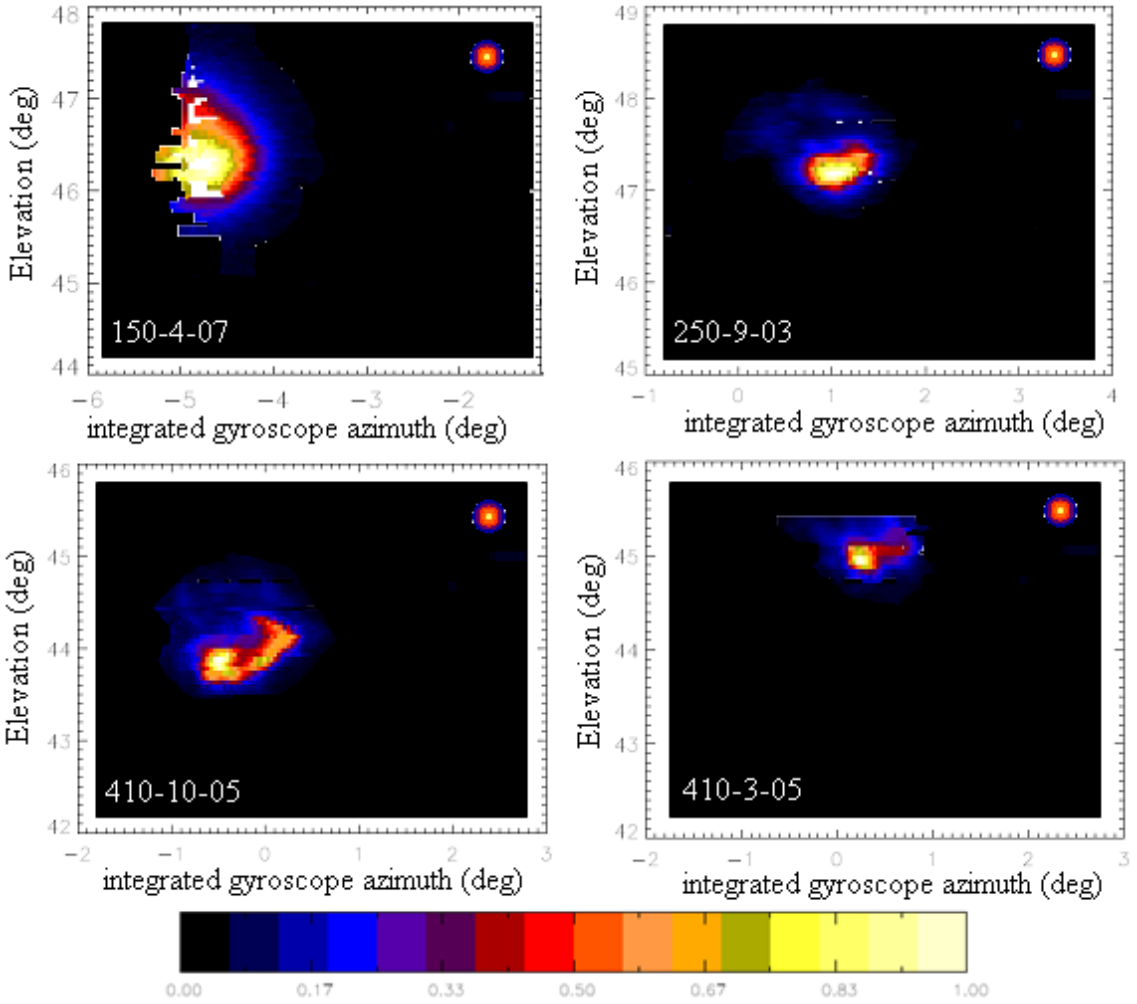

Figure 4.15: 2D beam maps for a representative sample of the 12 total bolometers analyzed. Bin size here is 3' x 3'. To scale we show the footprint of a simulated 8' beam in the upper right corner of each plot. Label in lower left corner indicates band and position of bolometer (band – wafer row – wafer column).

Not only do these results imply beams significantly larger than expected, they all contain unanticipated spurious and asymmetric features. The sidelobe or wisp seen to the upper right of the apparent main lobe is present in all of the 250 and 410 GHz beams, but its prominence appears to wane almost linearly as the elevation coordinate of the main beam increases. If these features were to appear consistently in every map we would be inclined to ubiquitously attribute cause to the source – perhaps due to an unforeseen reflection or some other aspect of the AP set-up. But because the wisp changes between bolometers, it may imply a ghost or other anomaly inherent to the antenna response of the instrument. However, it may be possible that the

phenomenon causing this feature is indeed associated with our modulated source but its magnitude is highly sensitive to viewing angle which will vary between detectors because the AP he extreme near-field.

If we ignore the sidelobes for a moment and focus on the main lobe in each map, the beams nominally appear Gaussian. Taking both an azimuth and elevation cut across each map and fitting a Gaussian, we have derived the FWHM values reported in Fig. 4.16. If we take the mean of the two cuts after averaging over all bolometers, we get FWHM ~ 52', 27' and 18' for the 150, 250 and 410 GHz wafers, respectively. We should note that these values exclude any information on ellipticity; while the 150 and 410 GHz cuts seem relatively symmetric, the 250 GHz beams are far from it. For all three 250 GHz detectors, FWHM in azimuth is a factor of ~1.5 greater than the FWHM in elevation. Ignoring asymmetries for the moment and simply considering mean beam widths, the results in all bands are significantly larger than our design goal of 8'. Furthermore, there appears to be a correlation with wavelength. The ratio of band center wavelengths is 0.74 : 1.19 : 1.96 mm, or 1 : 1.7 : 2.7 . Using the average of results tabulated in Fig. 4.16, the ratio of measured beam FWHM is 1 : 1.5 : 2.9.

bolometer	azimuth FWHM (arcmin)	elevation FWHM (arcmin)
150-4-07	54	50
250-9-03	32	21
250-11-01	33	21
250-6-03	33	19
410-9-03	23	19
410-3-02	17	16
410-4-05	19	19
410-1-03	14	14
410-3-05	16	15
410-5-06	17	17
410-10-05	20	21
410-11-04	19	19

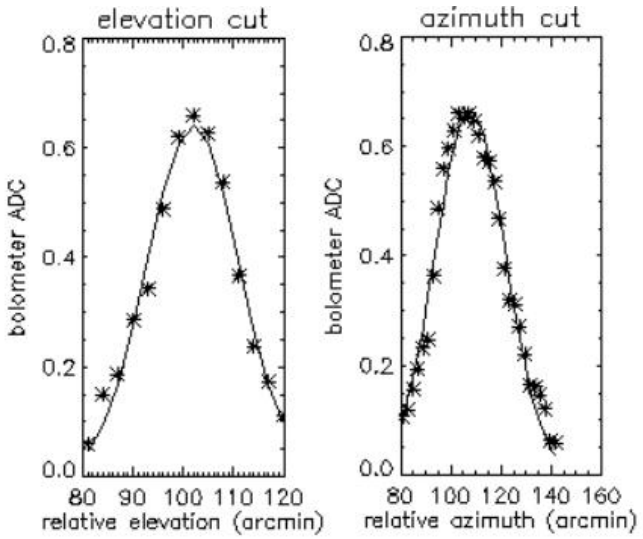

Figure 4.16: Deriving 2D FWHM from elevation and azimuth cuts. Cuts are performed on 2D maps like those shown in Fig. 4.15, taken across row and column containing the the pixel with maximum signal. Right – data (asterisks) and Gaussian fit (solid line), example shown is bolometer 250-11-01.

The results listed in Fig 4.16 are *not* the beam widths, but a convolution between the EBEX beams and the AP modulated source aperture. Only if we know with certainty that the AP

provides a perfect point source in the EBEX focal plane can we attribute the results entirely to the actual antenna response of the telescope. We know to the contrary that the modulated AP signal is not representative of a perfect point source, but in the EBEX focal plane is expected to span 2.5' in the 410 GHz test and 5' in the other two tests. However, applying this factor in a convolution falls well short of rectifying the FWHM values derived above. Hence we consider how much assembly errors and/or misalignment of the AP could have contributed to these results. As outlined in Sec. 3.3, the focus of a Cassegrain telescope depends on the position of the secondary mirror, and in this case, the placement of our modulated source. The former is significantly more important than the latter, as indicated below.

$$FWHM_{eff} = FWHM_{true} + \left|10.2 \cdot \left(0.28 z_{source} + 16 z_{\sec}\right)\right| \ (arcmin) \qquad (4.2)$$

According to equation 4.1, a misalignment of the secondary mirror by just 3 mm could completely account for an 18' 410 GHz beam. However, secondary misalignment cannot simultaneously and fully rectify both an 18' 410 GHz beam and a 52' 150 GHz beam.

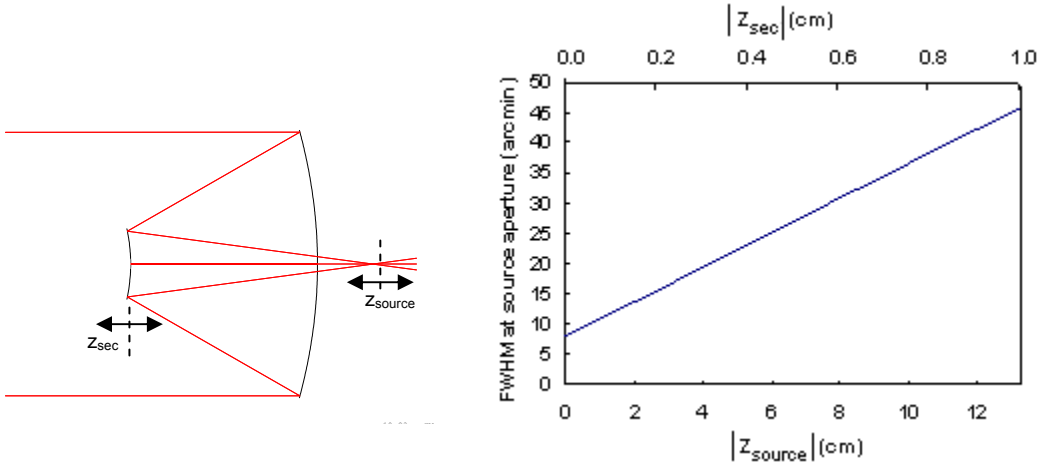

Figure 4.17: Theoretical prediction of EBEX beam defocus as a function of AP secondary mirror (z_{sec}) and/or modulated source (z_{source}) position. The y-axis on the plot represents effective FWHM of an EBEX beam at the AP source, assuming inherent EBEX beam is 8'.

It seems appropriate to also consider earlier and potentially related results – our measurement of beam width at the cryostat window (Sec. 4.5.1) as well as the beam mapping data collected at Nevis in Nov 2008 (Sec. 3.3.2). Although the data for beam width at the window seems to show a slight dependence on frequency, the magnitude of deviation from predictions (20-30%) falls well short of the inconsistencies seen in the integrated data (factor of ~2x at 410 GHz and ~6x at 150 GHz). We have not calculated the propagation of our measurements at the

window to FWHM on the sky, but this should be a topic of further study. One of the goals of such a study should be to determine whether there exists a certain positioning of the primary and secondary mirrors that accommodates our experimental data both at the window and from the AP scans.

We should also consider the fact that the Ft Sumner beams are inconsistent with the 250 GHz results derived from our Nevis data set. Comparing elevation cuts (since this is the only analysis performed on the Nevis data and therefore the only direct comparison available) and assuming the pac-man model is the correct interpretation of our Nevis data, the 250 GHz beams expanded from ~10' in Nov 2008 to ~20' in May 2009. Again, this discrepancy could be entirely caused by a ~3 mm misplacement of the AP secondary mirror according to Fig. 4.17. However, it would be surprising if the AP was almost perfectly assembled at Nevis and not at Ft Sumner - we consider the set-up procedure performed in Ft Sumner to be more robust than the procedure employed at Nevis. The only major configuration change between the two campaigns was the installation of the HWP – while a connection between HWP and beam width is not readily apparent, it deserves further thought. We have clearly not yet converged on a comprehensive model to explain these preliminary results, but the ongoing investigation should carefully consider potential contributions from both the instrument and the AP.

Finally, we have produced a preliminary analysis of relative beam positioning for the 250 and 410 GHz wafers (Fig. 4.18). In this figure we have extracted from each individual beam map the pixels which lie within the 0.95 boundary on their respective contour plots. Then representing the measured center of each beam as a red cross, we have inserted the measured pattern over the focal plane layout with the corresponding active bolometers highlighted in blue. There is a clear mismatch on the 410 GHz wafer implying a global and/or local discrepancy in rotation, translation and/or scale. Attempting the most straightforward technique first, we applied a simple rotation to the measured pattern about the detector at lowest elevation (bolometer 410-1-03). While no particular choice of angle precisely and comprehensively rectifies the correlation, a 6˚ rotation seems to provide the best overall consistency. There are obviously still problems even after applying this rotation, including evidence of residual scaling and translational offsets. The 250 GHZ wafer provides additional perplexity – the measurements appear to match the predicted layout without any adjustment at all. If we apply a 6˚ rotation to this wafer alone and about the middle one of the three live detectors (bolometer 250-9-03), the situation clearly worsens. However, if we consider the two wafers together, it seems a global rotation about bolometer 250-

9-03 may generate consistency in both channels and require a lesser overall rotation angle. This would be due primarily to the extended lever arm on the 410 GHz wafer provided by the approach. This effort along with a comprehensive model to explain all results presented in this section remain topics of ongoing work within the collaboration.

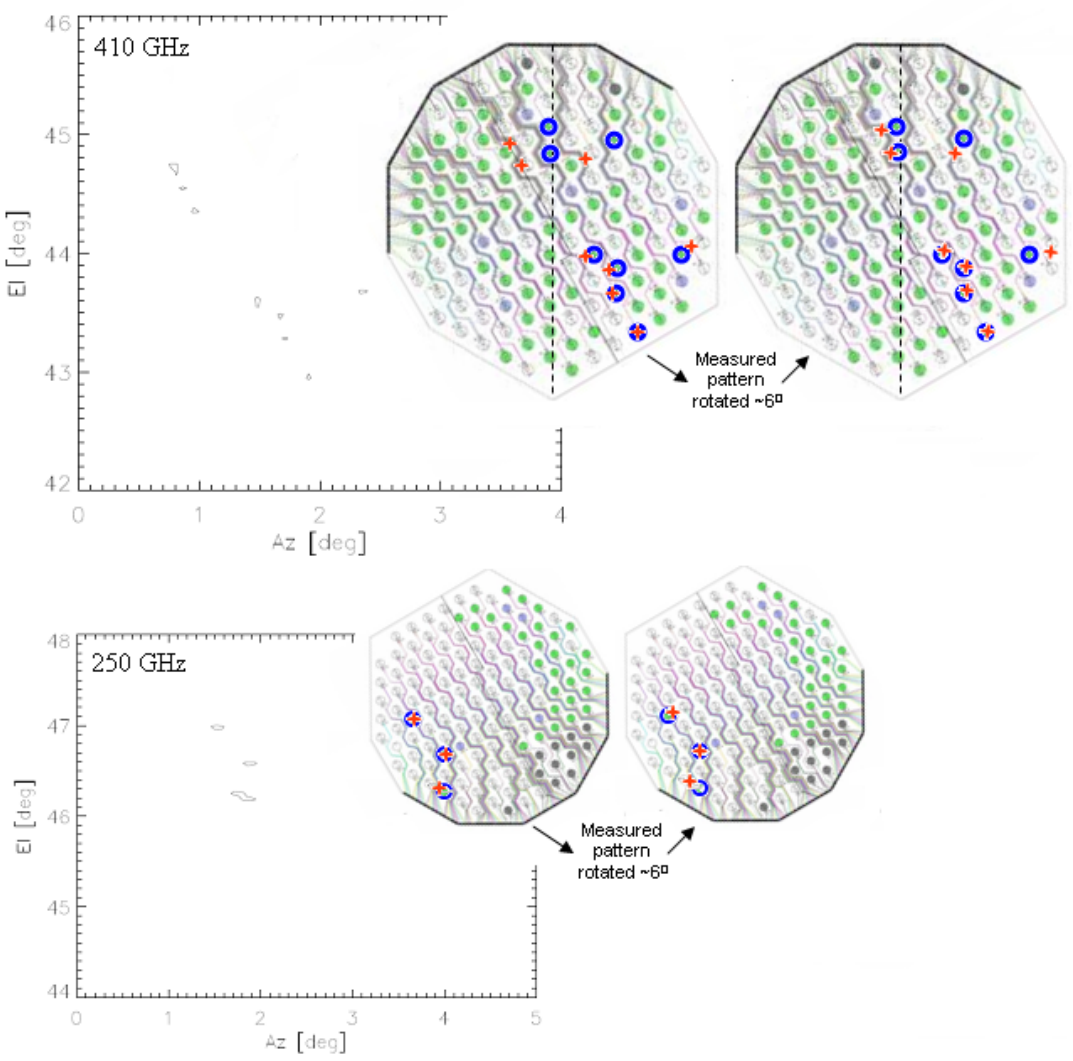

Figure 4.18: Preliminary cumulative beam mapping assessment, co-plotting all beam maps for a single channel on common axes and comparing to expected relative positions in focal plane.

Though final conclusions remain to be determined and will likely amend or expand the proceeding list, we posit the following issues and recommendations for further consideration:

- If we consider only the results of our elevation cuts on the main lobe, we see that the 250 and 410 GHz beams are very similar - average FWHM is within 2' of each other - while the 150 GHz cut is a factor of 2.5 larger. If we deem this cut our most reliable source of information on the true nature of the beams, we would conclude that the 250 and 410 channels must share some physical attribute that is different from 150 and serves as the dominant influence on beam size. Such a physical difference in fact exists – the 150 GHz bolometer probed in this exercise had an eccosorb plug in its feedhorn while all of the other detectors were open to light. Since the feedhorn has a major influence on antenna response, it seems reasonable to believe that altering its configuration could alter the beam. However, if We have not yet fully explored how the eccosorb plugs may vary instrumental response compared to those bolometers which are open to light, so more effort should be devoted to studying this issue. If the results of such a study indicate that the plugs likely have a significant impact on pre-flight calibration which cannot be accounted for during analysis, we will need to find an alternate approach to preventing bolometer saturation on the ground.

- We have not pursued a comprehensive analytical study of the effects related to the AP being placed in the extreme near-field of the telescope. While the device is designed to simulate a source at infinity if perfectly assembled and aligned, we have no quantitative assessment for the nature or magnitude of error introduced by non-ideal assembly or misalignment. Furthermore, with a primary mirror diameter of 96cm, the AP underfills our fiducial 110 cm diameter 150 GHz beam. More thought is required to assess whether or not the anticipated spillover could have contributed to the anomalously large 150 GHz beam measured in Ft Sumner.

- If the magnetometer remains the only azimuth pointing sensor used during ground-based beam mapping, extra care must be taken when designing and commanding the gondola scan parameters so as to avoid missing beams. One option would be to perform a dedicated experiment just prior to beam mapping which compares gyroscope and magnetometer output in real-time to determine offsets and anomalies which can then be accounted for when inputting the AP scan parameters. A simpler but less efficient approach would be to extend

the azimuth throw well beyond the expected field of view of the focal plane (or wafer, if probing only one wafer at a time as we did in Ft Sumner).

- We have not yet probed differential beam size as a function of HWP orientation. If such a difference exists beyond the level of a 0.2% deviation in FWHM between beams at the two orthogonal polarization states, leakage of temperature anisotropy into B-modes could exceed our baseline calibration benchmark (i.e., signal equivalent to IGB B-mode at r = 0.004) [47]. Since we expect such an effect to appear at $2f_{hwp}$, it should have a negligible impact on our signal bandwidth about $4f_{hwp}$. However, for completeness this effect should be probed experimentally according to the following procedure if time allows: after performing an AP scan with the HWP oriented at position angle α - which could be arbitrary or intentionally aligned with one the axes in cryostat coordinates - rotate the HWP to α ± 90° and repeat the scan. Any difference in FWHM between the maps derived from these two data sets should directly measure the influence of HWP orientation on beam shape.

- A more robust method should be devised for focusing the AP. At Nevis we used an optical approach: after placing a flood lamp ~ 30 m away from the AP, we attempted to form an image of the lamp at the appropriate distance behind the primary mirror. Since the flood lamp was in the near-field, we calculated the appropriate image position with $1/o + 1/i = 1/f$ where o is the object distance, f is the focal length of the system, and we solved for the image distance, i. From i we determined that the image should be focused at a point ~ 70 cm behind the primary. This is 50 cm beyond the focal point for an object at infinity. Therefore, held a piece of white paper by hand at 70 cm behind the primary as measured with a meter stick, and adjusted the secondary mirror position to focus the image of the flood lamp on the piece of paper. We identified two potentially significant sources of error in this procedure – (1) there was likely ± 5 cm of uncertainty in the position of the paper, and (2) the flood lamp image was fuzzy throughout the exercise and changes in quality were indistinguishable over a range of approximately ± 5 cm of best focus when moving the piece of paper closer to or further from the primary. Additionally, this method offers no assessment of focus in the x or y directions. In Ft Sumner we abandoned the optical approach, opting instead to align the system mechanically with our CMM. For the future, using the CMM for initial assembly seems appropriate, but optical verification is critical.

This requires either (a) building a structure to mount an imaging surface at the appropriate distance behind the primary mirror, or (b) imaging a source which lies in the far-field. The former will also require a different near-field source for best results. For the latter, a primary candidate is the Sun. While still on its cart, the AP could be rolled outside and pointed upward at the Sun, which should form an image at the same location where the modulated source aperture will then be positioned. Pointing will present a major challenge if this technique is employed, as will the fact the Sun is constantly moving across the sky. However, if done quickly enough, the error introduced should be small and present primarily (perhaps only) in the x-y plane.

- As evidenced earlier in this section, if the experiment produces unexpected beam maps, it is difficult to decouple the contributions from the AP vs. the instrument. We recommend employing the AP in its original MAXIPOL configuration for the next iteration of integrated pre-flight beam mapping. We have in our possession all the necessary hardware, which should be restored to full working order with little effort. The MAXIPOL team successfully employed this apparatus as evidenced by the fact their pre-flight beam maps were generally consistent with the beams as determined in-flight. If two separate sets of beam maps are produced using the AP in MAXIPOL and then EBEX modes, any differences can be attributed to the AP which should in turn allow us to more accurately extract the true instrumental antenna response. As discussed in Sec. 3.3.2, for EBEX we redesigned the AP as a Cassegrain telescope for the purposes of integrated polarization testing, and the AP should continue to be used in this mode for PR and IP experiments.

4.6 Relative Spectral Response

As detailed in Sec. 3.3.1, we are aiming to derive a relative spectral response model for each band to facilitate celestial component separation in the analysis pipeline. To this end, we collected data on each wafer during the cryogenic phase, illuminating the cryostat with a modulated monochromatic input signal from our Ebert-Fastie monochromator (EFM). After integration, we coupled the EFM to our artificial planet and gathered a second set of data on the 410 GHz band, successfully demonstrating for the first time a viable and potentially advantageous integrated version of the experiment.

4.6.1 Cryogenic Experiment

From 22 - 25 Apr 2009 we collected relative spectral response data for each band using the Ebert-Fastie monochromator (EFM) and following the set-up described in Sec. 3.3.1. Fig. 4.19 includes a photograph of the experiment as implemented in Ft Sumner. We began with the 410 GHz wafer, first flashing a sheet of aluminum over the window to identify our most responsive active bolometer as described in Sec. 4.4. This detector's beam axis was then found and marked using the beam centering tool.

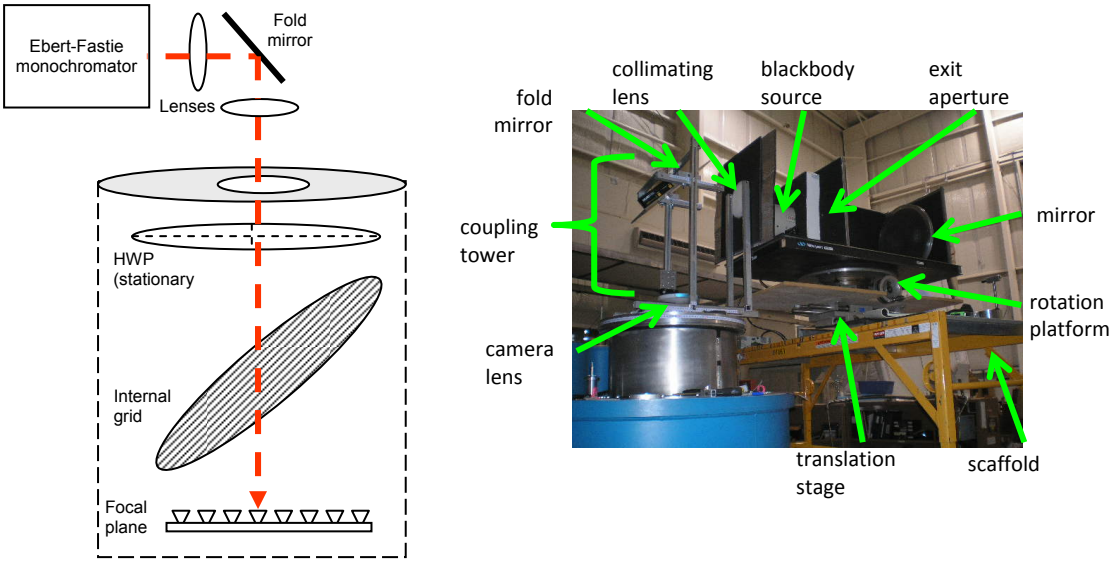

Figure 4.19: Relative spectral response experiment with Ebert-Fastie monochromator (EFM). In the photo, one wall and the roof of the EF enclosure have been temporarily removed.

The support structure holding the camera lens, fold mirror and collimating lens was then mounted onto the cryostat window and each element manipulated to achieve coarse alignment based on the window marking. For finer alignment, we attempted to trace the cryostat beam backwards from camera to collimating lens using a 6"-diameter aluminum disc. We first measured ADC for our target bolometer with the disc placed just above - and filling - the camera lens. We then moved it by hand upward toward the fold mirror and then horizontally over to the front surface of the collimating lens, expecting the signal to remain constant throughout this

motion since the beam should ideally be collimated in this regime. In practice we initially measured a ~10x loss between the camera and collimating lens; 4 hours later and after many adjustments to the coupling elements, we measured a 2x loss. We anticipated that further improvement would likely be marginal and would require extensive additional effort, so we decided to proceed to the next step.

The EFM was on an x-y translation stage and a rotational platform to facilitate x, y, and yaw control of the monochromator beam. The entire apparatus was mounted on a scaffolding to achieve the height required to properly align with the coupling tower. We initially installed a flat aluminum plate where the diffraction grating would be mounted, and rotated the plate to an angle of 0˚ (i.e., parallel to the mirror at the other end of the enclosure). Since there's no frequency selection in the absence of a diffraction grating, this configuration provides maximum flux at the exit aperture as is advantageous for alignment. With the blackbody source and chopper turned on at the entrance aperture, the scaffolding was rolled into place and adjustments in x, y and yaw were made as necessary to maximize the modulated signal as measured in the FFT peak at the known chop frequency, f_{chop} (3.2 Hz). In this configuration we maximized the peak at ~50 over 10 seconds of integration, for S/N ~500. At this point the Ebert-Fastie exit aperture diameter was set to ½".

We replaced the flat plate with the 410 GHz diffraction grating and placed it roughly at an angle of ~ 0˚. Maximizing the 0^{th}-order peak in our target bolometer with fine adjustments to the grating angle, we determined the true 0˚ point to within 0.1˚ and with S/N ~ 30 in 10 seconds. We then dialed the grating to 24˚ and stepped through to 36˚, recording the FFT peak after each 0.5˚ increment. We observed the peak emerge and disappear at approximately the expected cutoff frequencies and measured $30 < S/N < 40$ near the center of the predicted band. The experiment was repeated another three times and the results are plotted in Fig. 4.20. The exit aperture was modified between each sweep as explained in the caption. In the left panel we have plotted signal in the raw units recorded in real-time from kst to highlight the change in signal strength with varying EFM configuration. The first data set shown in blue was taken *without* order-sorting filters installed at the exit aperture and shows a signal magnitude slightly less than twice that measured *with* the order-sorting filters (the data sets in green and orange). Since the HPF order sorter is a thick grill filter with ratio of waveguides (holes) to total area of 0.58 and transmission at $\nu > \nu_c$ is approximately described by this ratio, the factor of ~2 between blue and green/orange curves is consistent with expectations. Between collecting the green/orange data

and the data shown in red, we squeezed the exit aperture down from ½" to ¼". In the ideal limit where the EFM exit aperture is imaged perfectly onto the detector in both cases, we would expect the signal to drop by a factor of 4 given the 2x reduction in aperture width. However, we see the signal in red is only a factor of ~2.5 lower than the green and orange.

We reason that the discrepancy is evidence of imperfect optical coupling between the EFM and EBEX beams, which is not surprising given the nature and preliminary indications of our alignment procedure. We reason that the image of the exit aperture is effectively out of focus at the focal plane. Given this model, a relatively greater fraction of modulated signal will be lost in the ½" configuration than the ¼" case, which is consistent with our measurements. With further investigation we may be able to extract a more quantitative assessment of image quality given the ratio of the signal strengths and perhaps even set a lower limit on the actual angular extent of the image in the focal plane.

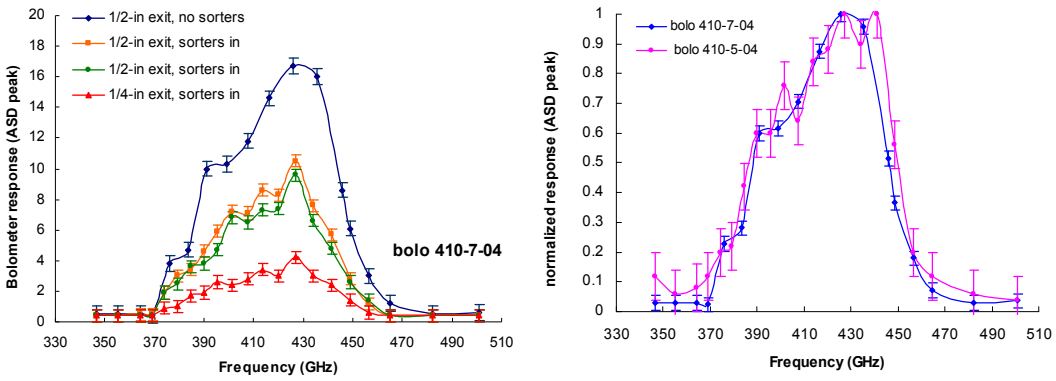

Figure 4.20: Preliminary 410 GHz spectral response. *1/2-in exit* indicates ½" EFM exit aperture, *no sorters* means order-sorting filters were removed in this trial. Left - Four separate data sets with bolometer 410-7-04. Right – Comparing response from two different detectors, 410-7-04 and 410-5-04.

After completing these tests, we re-aligned the apparatus on a neighboring bolometer, 410-5-04, separated in the focal plane by 11.5 mm (~20' in angle on the sky) from the first detector 410-7-04. The two data sets are normalized and plotted together in Fig. 4.20 to highlight their consistency. We observed no signal in bolometer 410-7-04 while collecting the data which is plotted in magenta above. This result implies a ~40' upper limit on the size of the exit aperture image in the focal plane. Further analysis is required to determine if this interpretation is consistent with the coarse lower limit we expect can be derived from the ratio of signal strengths

as proposed in the previous paragraph. Data were then collected for a single 150 GHz detector and a single 250 GHz detector, following similar procedures. Results are plotted in Fig. 4.21. S/N was lowest for the 150 GHz bolometer presumably because its feedhorn was one of those fitted with an eccosorb plug (at the time we avoided all open 150 GHz bolometers based on evidence of saturation).

In practice we used exit aperture sizes and grating steps that were slightly different from the nominal values assumed in Sec. 3.3.1 and used to calculate our theoretical EFM relative flux model. Accounting for these deviations and applying this slightly modified flux model to the experimental data, we derive the relative spectral response functions plotted in Fig. 4.22.

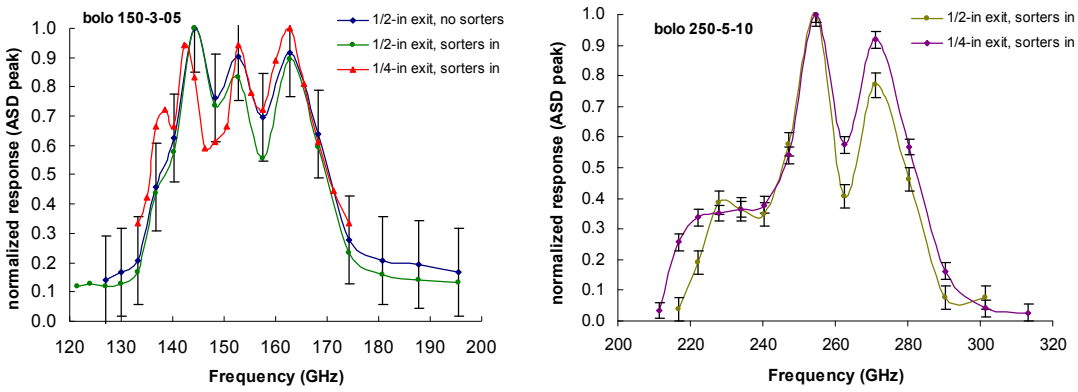

Figure 4.21: Preliminary 150 (left) and 250 GHz (right) relative spectral response. Bolometer 150-3-05 had an eccosorb plug, 250-5-10 was open to light. Error bars only included for 1 data set at 150 GHz to avoid overcrowding the plot (uncertainties were similar in all 3 trials).

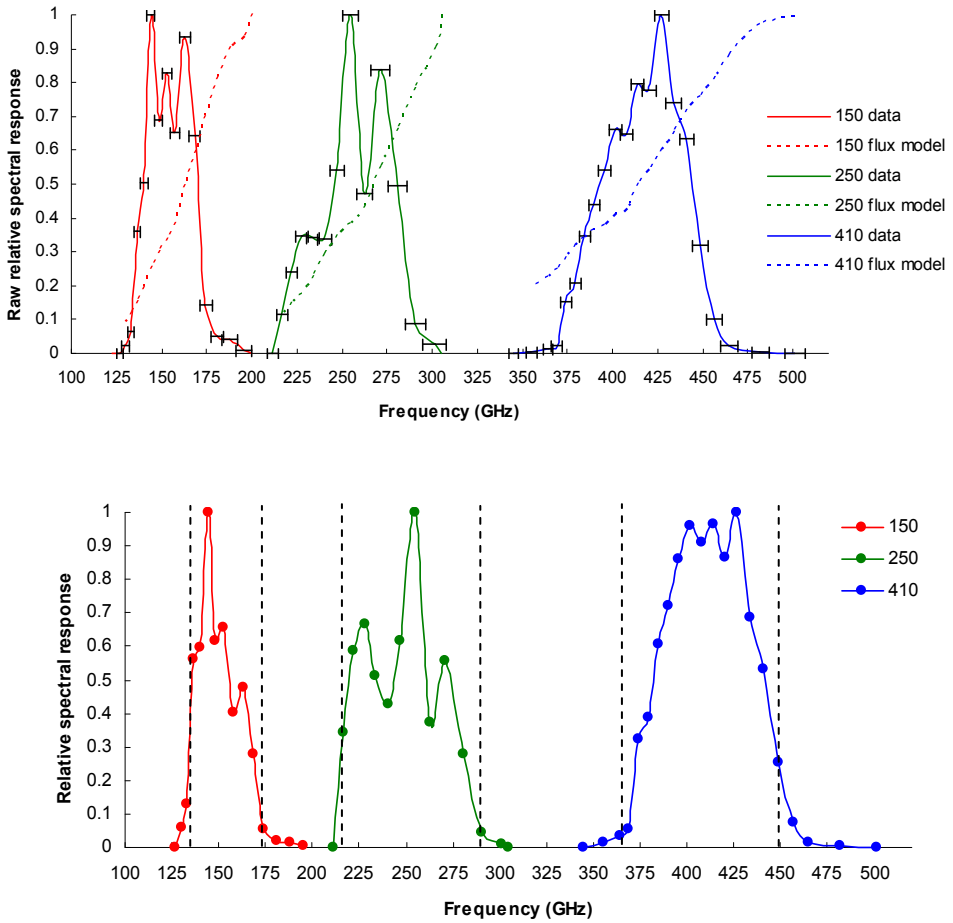

Figure 4.22: Top – Solid lines are raw (normalized) data averaged over all trials. Dashed lines represent relative flux model modified to include actual experimental configuration. Horizontal error bars indicate theoretical window function at each data point collected. Bottom – Comprehensive spectral response after applying EFM relative flux model. Dashed lines represent cutoffs predicted by filter theory and design.

The final models shown in the bottom panel of Fig. 4.22 have three striking features. First, the measured cutoffs very closely match the predicted cutoffs within the uncertainties of the experiment. Only the 410 GHz band may be an exception to this general observation, as the empirical bandpass appears to be shifted (+ 10 GHz) and is not as wide as expected. Second, the high edge cutoff for each band has a noticeably shallower slope than the lower edge, particularly in the 150 and 250 GHz bands. We tentatively attribute this to the fact that the window functions increase in width at higher frequency – convolved with the true cutoff, this inevitable feature of EFM operation could potentially wash out what might actually be a sharper edge. However,

since the high edge is defined by the focal plane LPFs and their transmission spectra seem to show a relatively shallower slope than what we would predict for the waveguide cutoff at the low-ν edge (see in Fig. 4.6), the slow high-ν cutoff may actually be a true property of instrumental response. Third, the 150 and 250 GHz curves show sharp features throughout the band. Our leading hypothesis centers on anomalous optical phenomena inside the cryostat. Pending a more detailed investigation, we attribute these spikes to differential reflection, diffraction, emission, and/or refraction within the cryostat. We will be forced to reconsider this theory if these features persist in data collected after coatings have been applied to the cryogenic optics.

4.6.2 Integrated Experiment

The frustration and difficulty experienced in aligning the cryogenic apparatus motivated a search for more efficient alternatives and led us to consider an integrated approach where the EFM is mounted on the artificial planet. In this configuration the EBEX and Ebert-Fastie beams are coupled by the AP optics. Not only is the AP much easier to assemble and align, but probing different detectors can theoretically be accomplished simply by changing the gondola pointing direction. Herein lays the major advantage, since probing multiple bolometers with the cryogenic technique requires a nearly end-to-end realignment between each test.

In designing a structure to mount the EFM behind the AP primary mirror, we realized that (a) the length of the blackbody source prohibits the exit aperture from residing precisely at the AP focal point and (b) the f/ratio of the Ebert-Fastie beam (f/5.3) doesn't match the f/ratio of the AP secondary-to-focus beam (f/3.5). Deciding to proceed and assess the impact of these non-idealities later, we constructed a mounting mechanism from steel beams which placed the Ebert-Fastie exit aperture ~34 cm behind the AP primary surface (14 cm beyond the focal plane). This design is captured in Fig. 4.23 along with the overall experimental et-up and a photo of the system as deployed in Ft Sumner.

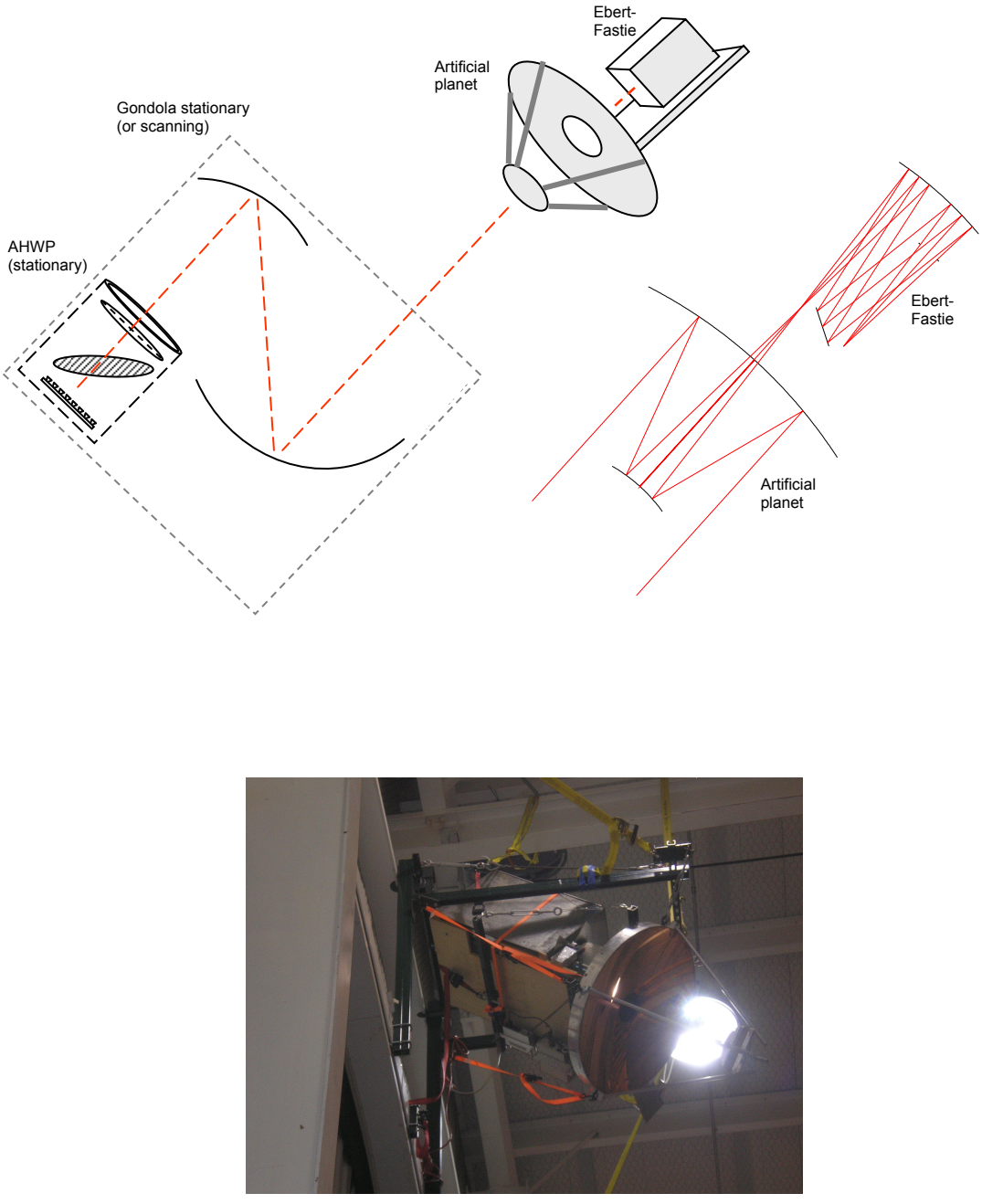

Figure 4.23: Integrated relative spectral response experiment with Ebert-Fastie monochromator mounted on the artificial planet (EFM on AP). Upper left – Conceptual design. Upper right – Code V simulation at 150 GHz. Right – EFM on AP as implemented in Ft Sumner.

With the Ebert-Fastie successfully mounted to the rear of the AP at 35' above the high bay floor, we installed our aluminum plate on the grating mount and dialed the exit aperture to ¼". The gondola was set on the ground and aligned to a 410 GHz target bolometer by adjusting azimuth and elevation to maximize the modulated signal seen in the FFT at the known monochromator chop frequency. Then replacing the plate with our 410 GHz diffraction grating, we found the 0th-order peak angle and proceeded to collect data while sweeping through grating angles 26˚-34˚. During this test we noticed a peak not only in our target bolometer, but also in a neighboring bolometer separated by 12' in the focal plane. The next day we repeated the experiment after aligning on a different 410 GHz bolometer, we used a ½" monochromator exit aperture and this time swept the grating from 23˚ to 37˚. The data are presented in various forms in Fig. 4.24.

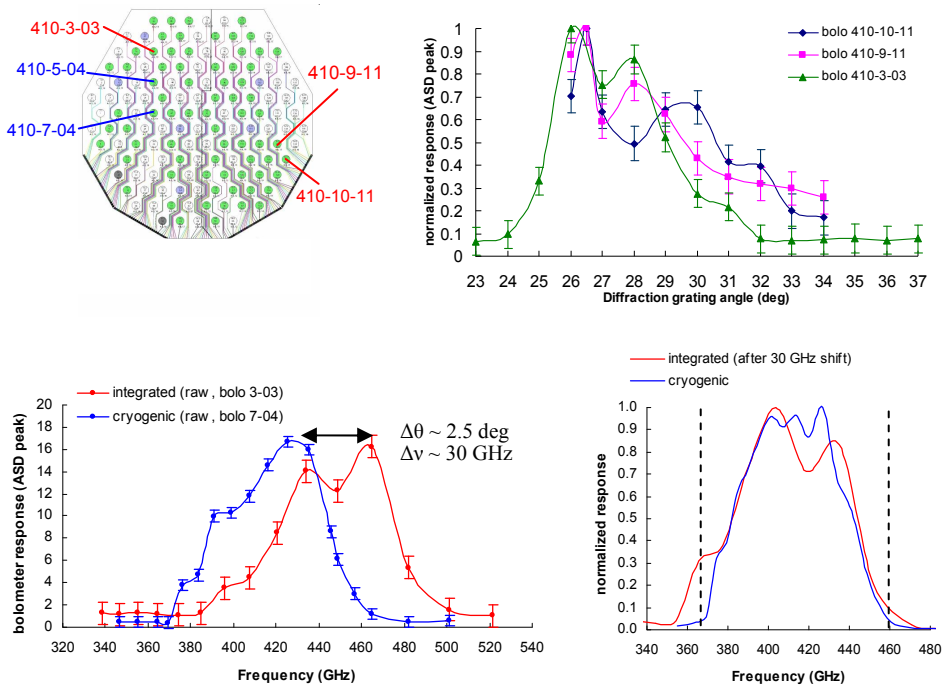

Figure 4.24: Relative spectral response results with EFM on AP. Upper left – focal plane positions of each 410 GHz bolometer probed over course of both cryogenic and integrated testing (cryogenic in blue, integrated in red). Upper right – Raw (normalized) response as a function of grating angle for all 3 bolometers measured during integrated experiment; 9-11 and 10-11 tested first with ¼" EFM exit aperture (S/N ~ 10 at max), 3-03 tested last with ½" exit aperture (S/N ~ 100 at max). Lower left – Raw response for the two bolometers with highest measured S/N. Conversion from grating angle to GHz has been made assuming nominal EFM design for both data sets. Lower right – Same data as shown in lower left after applying theoretical EFM relative flux and grating efficiency models. Also, a -30 GHz shift has been applied to bolo 3-03 data as required to achieve consistency with cryogenic response.

Amongst myriad lessons learned from this demonstration effort, we identify the following key conclusions:

- There is a clear systematic shift in the conversion from grating angle to emission frequency in the data set collected with the artificial planet. Because the shift is consistent amongst all three detectors probed over two separate integrated tests, we suspect a mechanical vs. procedural error. The EFM was designed under the assumption it would only be used horizontally, but it was at an angle of ~45˚ from the ground during these tests. We conclude from qualitative observations made of the system during testing that the likelihood of sag in the grating mechanism seems high. Only a small post and set screw couple the worm gear to the mounting rod; the weight of the grating clearly taxed this junction to if not past its limit of rigidity. By eye this strain appeared to increase as we dialed in greater grating angles. Given the orientation of the device, sag would indeed account for the direction of the shift. Whether or not this phenomenon is fully responsible for the 2.5˚ (30 GHz) shift seen in the data should be assessed through an independent experiment.

- During our first integrated test, two different bolometers (9-11 and 10-11) measured the modulated signal simultaneously. This is best explained as beam defocus at the EFM exit aperture, just as expected given that it was placed 14cm behind the true focal plane of the AP. While it is interesting that the two curves (bolos 9-11 and 10-11) have almost identical absolute values for detector response, these values are difficult to decouple from individual bolometer properties and tuning parameters and therefore do not necessarily imply anything about absolute flux. This same argument also undermines our ability to directly compare optical coupling efficiency in the integrated vs. cryogenic configurations – we illuminated different bolometers on different days with different system settings. However, we can comment that in both phases we measured S/N near the middle of the band exceeded 100 in the frequency domain over 10 seconds of integration. Based on the theoretical predictions, this measured S/N is approximately an order of magnitude below that expected under the ideal conditions assumed in Sec. 3.3.1. But assuming there is a mechanical resolution to the shift in emission frequency described in the previous paragraph, we conclude the experimental S/N is sufficient to

meet our calibration goals and the integrated technique is therefore a viable future approach for mapping relative spectral response across the focal plane.

Having realized apparent success with the integrated *staring* mode technique, we explored the possibility of even greater experimental efficiency and collected a set of data in *scanning* mode. Lifting the gondola off the ground and approximately aligning it on a 410 GHz target detector using the azimuth/elevation go-to pointing commands, we then executed a series of scans during which we noted a scan-synchronous rise and fall of peaks at the EFM chop frequency in the real-time FFT for several bolometers. We used an azimuth slew rate of 0.1˚/sec, azimuth throw of 4˚, elevation throw of 1˚, and elevation steps of 4' performed after each azimuth scan (15 total elevation steps). The monchromator grating angle was held constant for 15 scans, and then stepped to the next angle while the gondola reset back down 1˚ in elevation to repeat the procedure. A total of 5 grating settings were used (spanning 27˚ – 33˚), and the entire experiment took about an hour. From the results of the staring mode experiment we anticipate that the scanning results will again miss half the band since the initial grating setting was 27˚. Nevertheless, proof of concept would be a valuable outcome in itself and data analysis is in progress.

4.7 Polarization modulation efficiency

In this and the next two sections we discuss the experiments and preliminary results associated with the polarization performance of the instrument. The modulation efficiency (PME) of a polarimeter is a measure of how effectively it preserves the polarization fraction of incident light between entrance aperture and detector. The instrument will likely induce rotation and/or 'depolarization' along this path due to absorption, reflections, diffraction and/or refraction in and around the various optical elements. Determining this value empirically requires illuminating the focal plane with a polarized input signal, rotating the input polarization vector, recording the signal measured at the focal plane at each input polarization angle, and then plotting detector response vs. input angle. Reading the maximum (I_{max}) and minimum (I_{min}) signal from this plot, modulation efficiency is calculated as

$$PME = \frac{I_{\max} - I_{\min}}{I_{\max} + I_{\min}}. \tag{4.3}$$

A schematic of the experiment is shown in Fig. 4.25, along with an example of the plot that would be expected for a system with 90.5% PME.

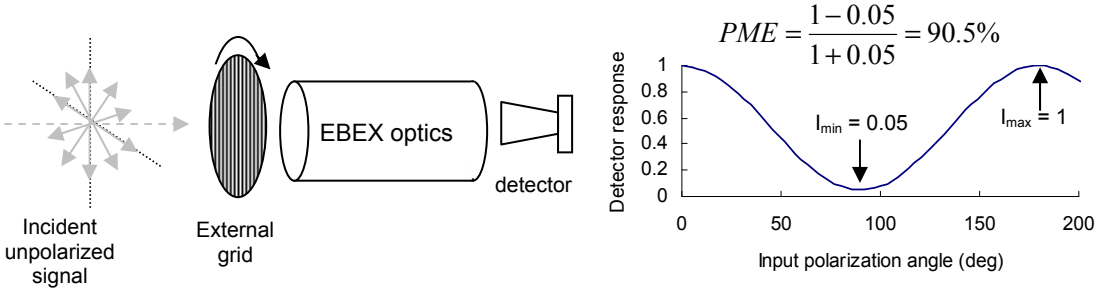

Figure 4.25: Conceptual illustration of polarization modulation efficiency.

A detailed mathematical treatise on polarimetry as applied to MAXIPOL (but almost comprehensively applicable here) can be referenced in [41] and [45]. Systematic polarization effects specific to EBEX are addressed in [48]. Over the next three sections we will discuss polarization and our experimental results assuming the most basic mathematical approach and temporarily overlooking second-order effects. For example, using the Stokes vector and Mueller matrix formalisms, we describe our PME experiment as

$$\vec{S}_{out} = \hat{\mathrm{M}}_{\mathrm{int}} \cdot \hat{\mathrm{M}}_{hwp} \cdot \hat{\mathrm{M}}_{ext} \cdot \vec{S}_{in} \tag{4.4}$$

where $\vec{S}_{in}$ is the Stokes vector of the unpolarized input signal, $\vec{S}_{out}$ represents the state of light after passing the internal grid, $\hat{\mathrm{M}}_{ext}$ is the Mueller matrix (MM) of the external polarizing grid, $\hat{\mathrm{M}}_{hwp}$ is the HWP MM, and $\hat{\mathrm{M}}_{\mathrm{int}}$ is the internal grid. Assuming the simplest form available for these elements and using the angle convention depicted in Fig 4.26, we have:

$$\begin{bmatrix} I_{out} \\ Q_{out} \\ U_{out} \\ 0 \end{bmatrix} = \frac{1}{2}\begin{bmatrix} 1 & \cos 2\psi & \sin 2\psi & 0 \\ \cos 2\psi & \cos^2 2\psi & \cos 2\psi \sin 2\psi & 0 \\ \sin 2\psi & \cos 2\psi \sin 2\psi & \sin^2 2\psi & 0 \\ 0 & 0 & 0 & 0 \end{bmatrix} \cdot \begin{bmatrix} 1 & 0 & 0 & 0 \\ 0 & \cos 4\phi & \sin 4\phi & 0 \\ 0 & \sin 4\phi & -\cos 4\phi & 0 \\ 0 & 0 & 0 & -1 \end{bmatrix} \cdot$$

$$\frac{1}{2}\begin{bmatrix} 1 & \cos 2\theta & \sin 2\theta & 0 \\ \cos 2\theta & \cos^2 2\theta & \cos 2\theta \sin 2\theta & 0 \\ \sin 2\theta & \cos 2\theta \sin 2\theta & \sin^2 2\theta & 0 \\ 0 & 0 & 0 & 0 \end{bmatrix} \cdot \begin{bmatrix} 1 \\ 0 \\ 0 \\ 0 \end{bmatrix}. \qquad (4.5)$$

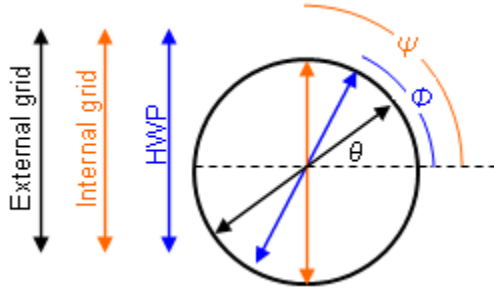

Figure 4.26: Angle convention used in Eq. 4.5. Double-arrowed lines represent transmission axes for the grids and o (or e) axis for the HWP.

Since the internal grid is static and for this experiment we hold the HWP stationary, we can choose for convenience in this demonstrative exercise $\Phi = \Psi = 0^\circ$. With these assumptions, equation 4.5 simplifies to

$$\begin{bmatrix} I_{out} \\ Q_{out} \\ U_{out} \\ 0 \end{bmatrix} = \frac{1}{4}\begin{bmatrix} 1 & 1 & 0 & 0 \\ 1 & 1 & 0 & 0 \\ 0 & 0 & 0 & 0 \\ 0 & 0 & 0 & 0 \end{bmatrix} \cdot \begin{bmatrix} 1 & 0 & 0 & 0 \\ 0 & 1 & 0 & 0 \\ 0 & 0 & -1 & 0 \\ 0 & 0 & 0 & -1 \end{bmatrix} \cdot \begin{bmatrix} 1 & \cos 2\theta & \sin 2\theta & 0 \\ \cos 2\theta & \cos^2 2\theta & \cos 2\theta \sin 2\theta & 0 \\ \sin 2\theta & \cos 2\theta \sin 2\theta & \sin^2 2\theta & 0 \\ 0 & 0 & 0 & 0 \end{bmatrix} \cdot \begin{bmatrix} 1 \\ 0 \\ 0 \\ 0 \end{bmatrix}$$

and we are left with the following form which our quantity of interest, $I_{out} \sim cos2\theta$:

$$\begin{bmatrix} I_{out} \\ Q_{out} \\ U_{out} \\ 0 \end{bmatrix} = \frac{1}{4} \cdot \begin{bmatrix} 1+\cos 2\theta \\ 1+\cos 2\theta \\ 0 \\ 0 \end{bmatrix}. \qquad (4.6)$$

To test for this value empirically, we used the hardware and set-up illustrated in Figure 4.27. We again covered the cryostat with our aluminum window mask. The external grid is inherited from MAXIPOL and known to polarize light passing through it at 96.6% [41]. It resides in a mounting ring which has a stepped feature on the bottom with OD just under 4", allowing us to seat it snuggly into the mask aperture. In an effort to minimize leakage of unpolarized modulated signal, we fitted the underside of the mounting ring with a barrier of ¼"-thick eccosorb LS-14.

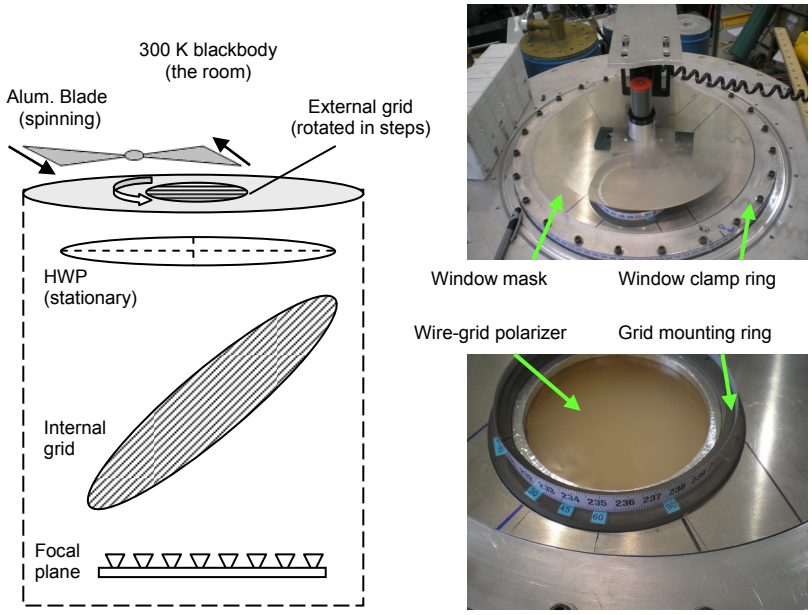

Figure 4.27: Polarization modulation efficiency experiment, conceptual design (left) and implementation (right). The wire-grid polarizer (lower right) was built for MAXIPOL by Buckbee-Mears with electroformed 0.0002 inch diameter gold wires on 0.0015 inch thick Mylar film at 250 lines per inch [46].

We first aligned the mask (and hence grid) over the 150 GHz wafer, orienting it approximately parallel to the axis of the internal grid. The orientation of the internal grid was determined during assembly and marked on the outside of the cryostat (likely accurate to ~ ± 2˚, but inconsequential to our results here which depend only on relative response as a function of relative external grid angle). With the chopper blade spinning and the HWP resting at an arbitrary position, we moved the external grid 190˚ in 5˚ increments. Viewing the FFT in real-time using kst (integrated over 10 seconds of bolometer TOD), we chose a representative bolometer and recorded the magnitude of the peak at the known chopper frequency for each step.

This procedure was repeated for the other two wafers. The data were saved electronically and we recorded the timestamp corresponding to each external grid angle in order to facilitate a post-test analysis of multiple detectors.

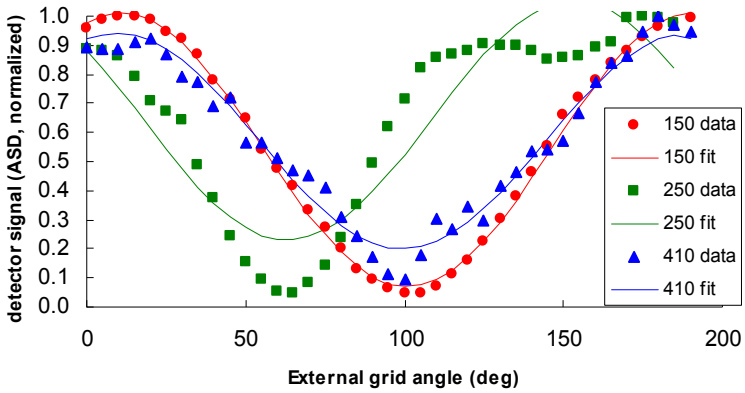

band	from data	from fit
150 GHz	94%	90%
250 GHz	93%	66%
410 GHz	85%	67%

Figure 4.28: Polarization modulation efficiency. Preliminary results from hand-written data recorded in real-time for one representative bolometer on each wafer. The data are normalized, fits are proportional to *cos(2θ)*.

Figure 4.28 displays both the real-time data points recorded from kst and a *cos(2θ)* fit for our representative bolometer on each wafer. From these results we have calculated PME in two different ways: (1) using I_{min} and I_{max} directly from the individual data points which have the lowest and highest values on the plot, and (2) taking I_{min} and I_{max} from the minimum and maximum values derived from the fit parameters. For the 250 and 410 GHz bolometers, it comes as no surprise that there is a large discrepancy between these two methods since the raw data clearly deviates from the expected *cos(2θ)* shape. We are more inclined to accept the result derived directly from the data, but suspect even these values likely come with significant uncertainty as a result of the unanticipated scatter in the 410GHz plot and odd plateau evident in the 250 GHz data. We have yet to identify a physical model explaining the plateau. We initially hypothesized that the HWP might have unexpectedly moved when the external grid was oriented at around 100˚ since on several other occasions we observed it slipping into what we assumed were magnetic potential wells adjacent to its current position. However, we repeated the experiment in its entirety immediately after finishing the first round of data collection and came up with almost identical results. As for the 410 GHz data, the cryogenic fridge cycle expired

shortly before executing this test so the temperature of the focal plane may have been changing and thus responsible for the seemingly random noise seen here (which is not present for the other two wafers).

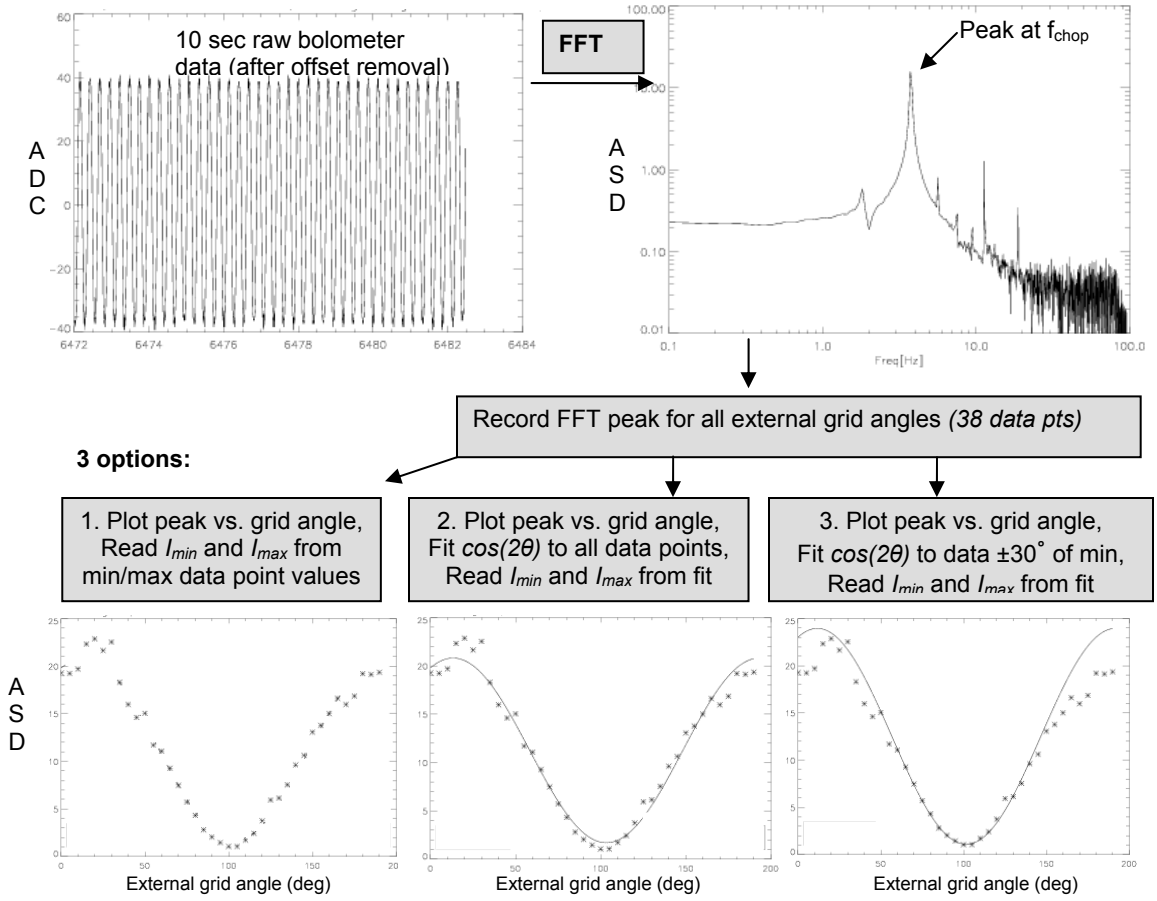

Figure 4.29: Polarization modulation efficiency analysis pipeline.

In an effort to gain a stronger statistical lever arm on the instrument's true performance, we have developed a pipeline to process the electronic data for all the detectors in operation at the time of the experiment. Fig. 4.29 highlights the key steps in the procedure, which are detailed in [46]. Sagiv has compiled results for the 150 GHz wafer after analyzing a total of 42 bolometers. In addition to calculating PME with the two techniques described in the previous paragraph, he has employed a third approach by calculating the fit using only the data points lying within 30˚ of I_{min} (in external grid angle), excluding the pervasively anomalous points near I_{max}. His results are

summarized in the left panel of Fig. 4.30, from which we make the preliminary conclusion that $PME_{150} = 93 \pm 2\%$.

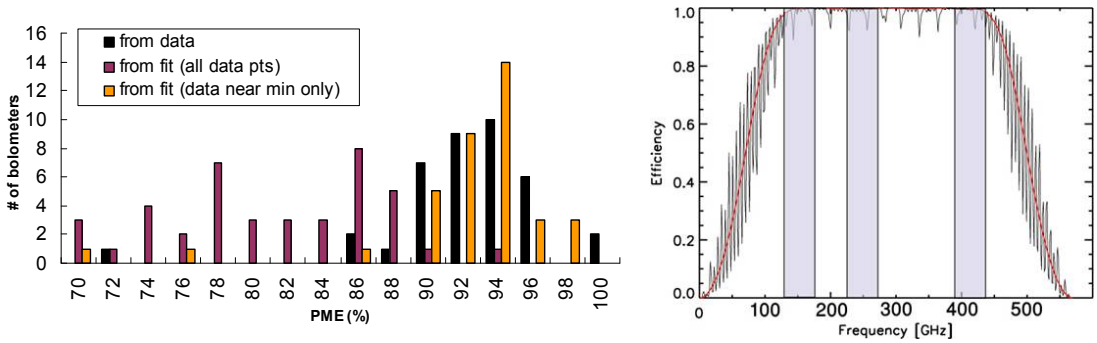

Figure 4.30: Left – Cumulative preliminary results for 150 GHz PME derived separately from each of three options described in Fig. 4.29. Right – Theoretically predicted PME as a function of frequency based on AHWP simulations (result: PME ≥ 98% at all in-band ν) [45].

As stated in Chapter 3, our science goals require PME > 90% and simulations predict efficiency > 98% across all bands as depicted in the right panel of Fig. 4.30. Our measurement of ~ 93% PME is near the minimum criterion and below expectations. However, strong evidence suggests that this should be interpreted only as a lower limit: when viewing all the TOD on a single plot, we see a significant change in mean ADC level between maximum and minimum response. The presence of this trend implies differential detector response at different external grid angles. More specifically, response decreases with increased optical load, which means the data points collected near maximum are artificially lowered. This leads directly to calculating lower than true PME.

Another potential contributor is leakage of unpolarized signal into the timestream: if modulated signal bypasses the external grid and is measured by the bolometers, this will generate a baseline response at f_{chop} independent of external grid angle and lower our calculated PME. We anticipated this possibility and attempted to explore it experimentally in Ft Sumner. We first recorded the FFT peak with the external grid at an arbitrary angle using our normal procedure. We then sealed the external grid mounting ring to the window mask with aluminum tape, and did the same around the edge of the window mask itself, taping it down to the cryostat window clamp ring. Observing the FFT peak again in this configuration, we expected to see a drop in the magnitude of the peak if leakage were present. There was no detectable change. However, this

does not mean there was absolutely no leakage. It simply means we noticed no difference in the FFT peak at f_{chop} while viewing the signal in real-time. A more robust approach is available and discussed below.

We conclude that a lower limit on PME has been measured for the 150 GHz band and conclusions regarding the other channels will come after the completion of an ongoing analysis effort. The discrepancy between measurement (~ 93%) and prediction (> 98%) may be fully explained by differential bolometer response at high optical load, unpolarized leakage, or possibly a combination of these two effects. It also may be the case that the true PME was < 98%; the predictions were derived considering polarization modulation as a function of an AR-coated AHWP only. In Ft Sumner we had no AR-coating on any of the optics, which we hypothesize increased the possibility of polarized systematics due to differential transmission and reflection. The field lens seems a likely spot for the most significant effect since it presents a large curved surface offset at an angle from the axis of the beams. This element (and others) may introduce polarization rotation which would alter the polarization vector for some fraction of light incident on the HWP, thereby allowing some fraction of the modulated signal to leak through to the focal plane. This would artificially raise I_{min} and reduce our calculated PME. If this model is correct, we would expect to see the most impact on the 150 GHz data since these beams are largest and therefore intercept a relatively larger fraction of the field lens (relative to the higher frequency channels). Unfortunately, our data at 250 and 410 GHz appear anomalous given the fact they deviate so significantly from the expected functional form (as shown in Fig. 4.28). Therefore, although we plan to proceed with analyzing the current data set in these bands, it seems improbable that the results will reveal our predicted direct relationship between frequency and PME.

Future iterations of the experiment - after implementing some suggestions for improvement as listed below – should produce more comprehensively reliable data with which we should be able to more accurately explore our hypothesis. In the meantime, we intend to repeat our simulations for the case of non-AR-coated optics, aiming to quantify the impact AR-coating has on polarization response within the instrument. Listed here are lessons learned and recommendations for the future:

- Differential bolometer response must be either prevented experimentally or accounted for in data analysis. The latter approach has been demonstrated by the MAXIPOL team, details of

which are captured in [41]. Prevention may be accomplished by reducing the magnitude of the chopped load – instead an aluminum blade vs. the background room ($\Delta T \sim 285$ K), we could provide a 273 K background load by mounting a polystyrene cooler filled with eccosorb and ice water, modulated by a room temperature eccosorb-covered chopper blade inserted between the cooler and the window ($\Delta T \sim 27$ K). In the current configuration with the 4"-wide MAXIPOL grid nested in an aluminum window mask, the majority of beams at any given time are actually filled by the 300 K blackbody load provided by the eccosorb-covered underside of the mask. Therefore, to make a 273 K background load truly fill the entire background - and also to improve experimental efficiency (i.e., probe all wafers simultaneously) - we need to eliminate the mask. This means implementing an approximately window-filling external grid. We have constructed such a grid (see Sec. 4.9) but preferred to use the MAXIPOL grid in Ft Sumner because of its known polarizing efficiency. Since external grid efficiency is an important quantity to back-out during analysis, we would have to make an empirical determination of the efficiency of our window-filling polarizer. This could be accomplished using a procedure similar to the one employed by the MAXIPOL team in calibrating their polarizers, as described in [41]. The technique requires two identical polarizers; we have plenty of material left over from constructing our first grid, so a second one should present no new technical challenges. Employing a window-filling grid also demands a window-filling chopper. As mentioned previously, we constructed such a device for optical efficiency testing but abandoned it after motor failure prevent $f_{chop} > 25$ Hz. For PME and every cryogenic experiment other than optical efficiency, we require f_{chop} no greater than ~ 12 Hz. Therefore, we expect that our big chopper blade could be implemented almost immediately, pending slight modifications suggested in Sec. 4.2 to improve rotational stability as well as adapting it to match the angle of the future external grid mount.

- Mounting the external grid parallel to the window (and hence the HWP) may have caused spurious reflections that could have introduced error into all of our polarization data (Sec. 4.7 – 4.9). Although further thought is required to assess the impact this effect may have had on the preliminary results presented in this thesis, for the future we should fabricate new mounting hardware to ensure the external grid is positioned at an angle. This will presumably take the form cylinder coupled to the outer edge of the cryostat window (the

window clamp ring) where the top of the cylinder is cut off at an angle. The appropriate angle remains to be determined, but will be driven primarily by the goal of deflecting any possible reflections out of the beam path and onto the interior of the cylinder where they are absorbed (interior should be lined with eccosorb HR-10 or other absorbing material).

- A different method should be used to determine the magnitude of unpolarized leakage, which we will call the *baseline*. Instead of letting light through the external grid and looking for a change in the FFT peak after taping around the edges, we should entirely cover the external grid with an aluminum plate, run the chopper above it as done during normal operation, and look for any signal at all in the bolometer data. The covered grid should be rotated around 360° to identify if the baseline varies with angle. This should provide a more robust and accurate measurement of the baseline.

- In Ft Sumner we rotated the external grid a total of only ~ 190°. As seen in Fig. 4.28, our data over this span were inconsistent the expected functional form dictated by the experiment, which leaves us with unanswered – and perhaps unanswerable - questions. For the future we recommend rotating the external grid a full 360° to maximize the amount of information gathered. Data collected over the second 180° of rotation should be identical to the first 180°; differences imply anomalies in the experimental procedure or the instrument which would be critical to identify and impossible to discover without a full 360° of data.

- We manipulated the orientation of the external grid manually in Ft Sumner, making each 5° step by reaching under the chopper blade and rotating the grid by hand. While we calculated the angular error at each point at < 2°, the process could be greatly enhanced by automation. This could be accomplished with a stepper motor and gear, coupled to the external grid mounting ring which would be fitted with gear around the outer edge (a gear with OD ~ 15" if the window-filling grid is implemented).

- We have not fully explored the consequences of analyzing the data in the frequency domain with the pipeline described in Fig. 4.29. There may be errors introduced using this technique that could be avoided by working only in the time domain. An algorithm should be developed to extract the peak-to-peak magnitude of the chopped signal directly from the time

domain instead of reading I_{max} and I_{min} from peaks in the FFT which may be more susceptible to systematic error (e.g., potentially more power lost in the wings of the peak at I_{max} than I_{min}).

- PME can be assessed with an entirely different experimental approach – spinning the HWP while holding the external grid stationary. This experiment is identical to one of the tests used for probing polarization rotation, and is sketched in the rightmost panel of Fig. 4.37. The resultant data is shown in Fig. 4.39, which reveals peaks at f_{chop}, $f_{pol,low}$, and $f_{pol,high}$. The latter two peaks occur at $f_{chop} - 4f_{hwp}$ and represent the polarized signal. An algorithm exists to extract PME from the relative magnitude of these polarization peaks vs. the peak at f_{chop}. Work is in progress to apply this algorithm to the data collected in Ft Sumner. The results of that analysis may dictate whether to employ this approach in lieu of or in addition to stepping the external grid with stationary HWP. We recommend executing both – having independent results from two experiments provides a useful consistency check.

4.8 Instrumental Polarization

Instrumental polarization (IP) is the transformation of unpolarized to polarized light caused by the telescope, or equivalently, mixing total intensity into Q and U. This phenomenon is common to all telescopes and is depicted schematically in Fig. 4.31.

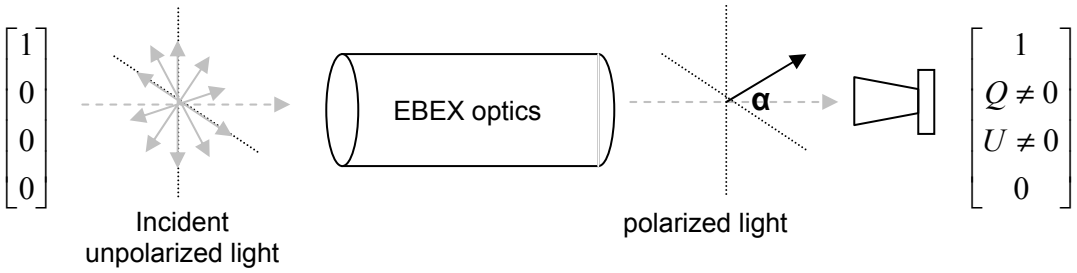

Figure 4.31: Conceptual illustration of instrumental polarization. Bookends represent the effect in terms of Stokes parameters.

Although all our optical elements likely contribute to IP, only the portion generated sky-side of the HWP is pertinent. IP originating between the HWP and focal plane will be excluded from the signal at $4f_{hwp}$ and therefore filtered out in the analysis pipeline. Theory and practical

experience indicate that the warm mirrors, cryostat window, and field lens will be the most significant contributors, with the field lens AR coating topping the list at somewhere between 0.5% and 4% depending on the actual coating applied (which remains to be determined, but was uncoated in this campaign) [47]. As shown in Table 3.1, there is no criterion for the magnitude of the effect itself, but whatever that magnitude is, simulations predict that we must know it to better than 0.05%. This benchmark requires illuminating the instrument with a source known to be polarized at < 0.05%. The only modulated emission source available to us and known to satisfy this criteria is the CMB dipole (< 0.01% polarized), which will serve as our primary calibrator for IP [47].

Though we plan to use a determination of IP from flight data in the final analysis pipeline, a ground-based assessment is useful as an early comparison to theory and as a consistency check on flight-based results. The proposed techniques are sketched in Fig. 4.32. In Ft Sumner we only executed the cryogenic experiment. As in previous tests, we provided a large modulated input signal by chopping the room with an aluminum blade mounted above a window mask with 4" aperture which is fully occulted by the blade. We expect the inherent polarization of this input signal to be small. However, we did not independently measure its polarized properties (nor are aware of a method available to do so), and for the present analysis simply assume it is fully unpolarized.

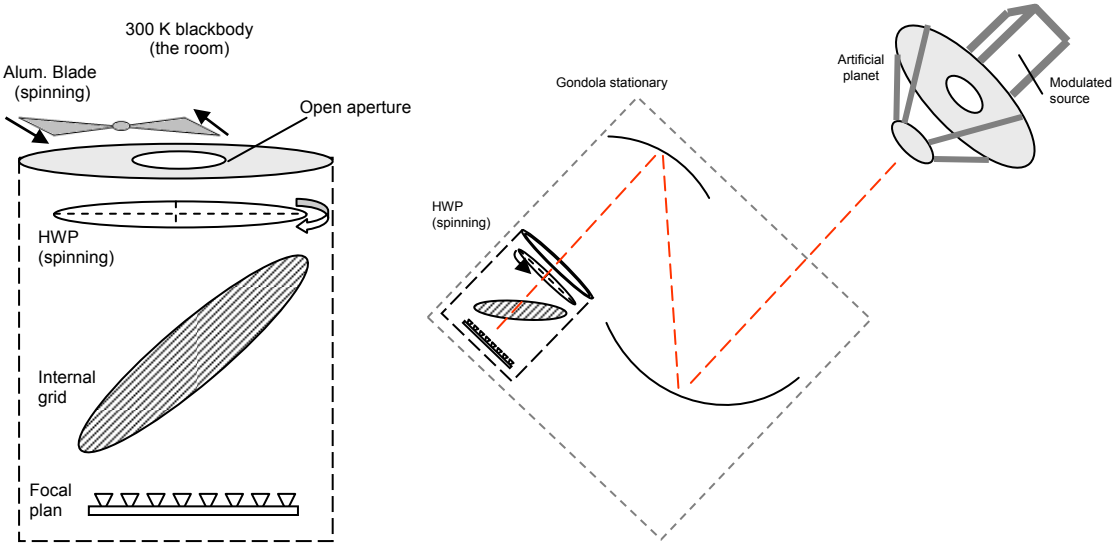

Figure 4.32: Conceptual designs for instrumental polarization cryogenic (left) and integrated (right) experiments.

Three sets of data were recorded, one with the mask aperture centered over each wafer. We collected bolometer and HWP encoder TOD spanning one minute during each test, and the HWP was rotated at a constant rate of ~1.1 Hz throughout the experiment. Extracting IP requires that we probe signal strength at two different frequencies: the unpolarized signal at f_{chop} which we will call I_0, and the polarized signal at one of two sidebands, $f_{pol} = (f_{chop} \pm 4f_{hwp})$, which we call I_p. Instrumental polarization is then a unitless quantity calculated as

$$IP = \frac{I_p}{I_0 + I_p}. \tag{4.7}$$

Observing the FFT in real-time, we aimed to maximize S/N in the lower frequency polarized sideband by adjusting f_{chop} such that $f_{pol,low}$ resided in a quiet portion of the frequency domain, unoccupied by other peaks. We therefore used $f_{chop} \sim 11.9$ Hz, giving $f_{pol} = 11.9 \pm 4.4 \sim$ 7.5 and 16.3 Hz. Fig. 4.33 shows an example of one second of bolometer TOD after removing a DC offset – notice that the 11.9 Hz chopper signal is clearly dominant, but the HWP template at 2.2 Hz is also evident. Taking the FFT over ~ 43 seconds for computational efficiency (2^{13} samples), we see the largest peak at f_{chop} as expected, along with other peaks at $2f_{hwp}$, $4f_{hwp}$ and f_{pol}. For a coarse preliminary estimate of IP we use Eq. 4.7, simply taking the maximum value of the peak at f_{chop} as I_0 and the peak at $f_{pol,low}$ as I_p. In panels 3 through 6 of Fig. 4.33 it seems apparent that there is more power in the wings of the f_{chop} peak than for $f_{pol,low}$, which will likely bias our IP results to lower than their true values. A more sophisticated and likely more accurate approach may be to lock in on the signals at f_{chop} and $f_{pol,low}$ and determine IP through a comparison of peak-to-peak magnitudes in the time domain. This technique should eliminate the error we presume is introduced by the difference in widths between the two peaks in the frequency domain.

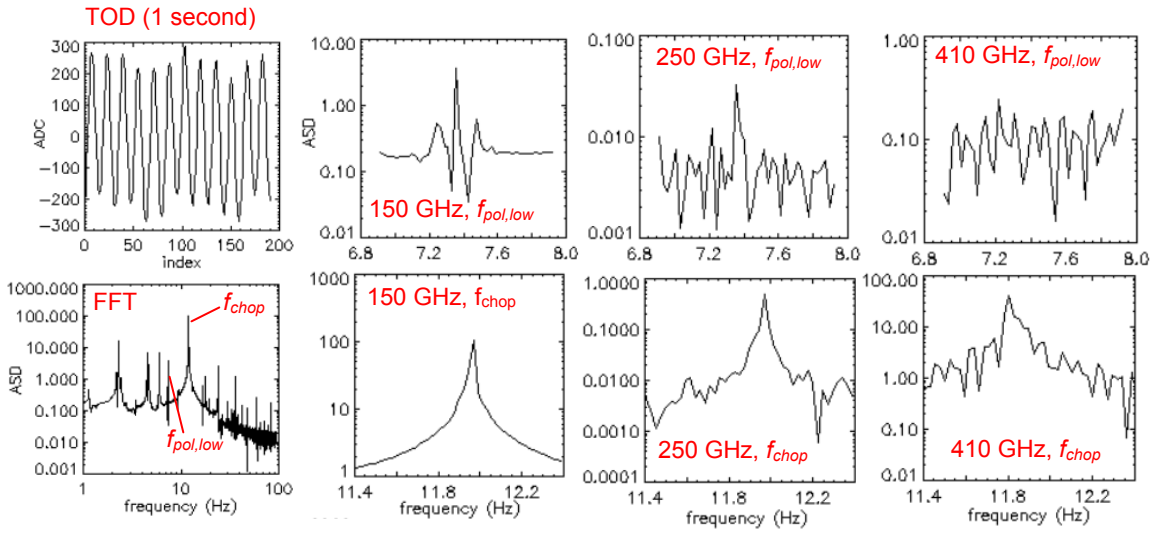

Figure 4.33: Instrumental polarization analysis pipeline. Example bolometer TOD and FFT on left, other panels are representative examples of peak at f_{chop} and $f_{pol,low}$ which we use to calculate IP.

A total of 67 bolometers were successfully read out during the experiment: 35, 20, and 12 on the 150, 250 and 410 GHz wafers, respectively. Fig. 4.34 summarizes our preliminary results, which imply IP with 1σ uncertainties of 6.7 ± 1.4 % (150 GHz), 4.7 ± 1.7 % (250 GHz), and 1.5 ± 0.5 % (410 GHz).

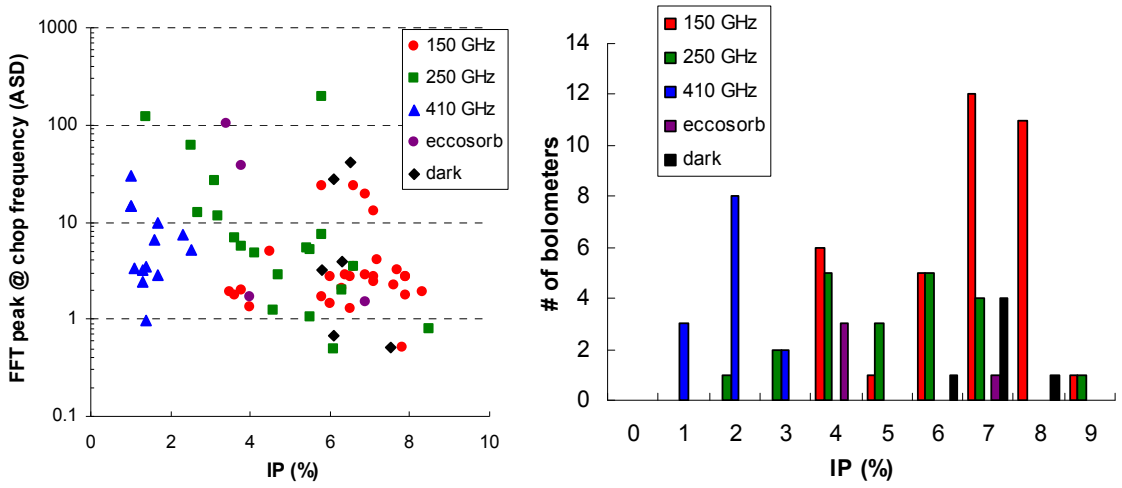

Figure 4.34: Preliminary assessment of instrumental polarization. Left – points labeled by band are all bolometers open to light; eccosorb and dark detectors are approximately evenly distributed between 150 and 250 GHz wafers. Right – Histogram of preliminary results by band and bolometer classification.

Since we expect IP ~ 4 % from a non-AR-coated field lens alone, our results at 150 and 250 GHz seem plausible. The value of 1.5 % at 410 GHz is unexpectedly low. However, it is unclear whether the simulations used to predict IP explored each band independently. It is possible that the prediction applies only to the 150 GHz channel and further work is required to examine the effect at higher frequencies. Regardless of analytical expectations, we have empirical evidence indicating that IP varies by band. This trend is consistent with our hypothesis stated in the previous section – the magnitude of polarized systematics caused by the non-AR-coated field lens should be directly correlated with beam size (maximum for 150, minimum for 410). Again, simulations should be revisited, now including the presence of uncoated optics. In addition to these suggestions and the recommendation to pursue a pipeline based on analysis in the time domain instead of frequency domain, we note the following concerns and proposals for future improvement:

- In the top panel we see that the ¾ of all bolometers had an ASD peak at the chopper frequency of less than 10. This is lower than expected given the magnitude of the chopped optical load, implying bolometer saturation and/or non-linearity. This conclusion is corroborated by the data from the eccosorb-plugged data points, whose average peak at f_{chop} is significantly higher than for those open to light. If we consider only the eccosorb bolometers, we would conclude a mean IP closer to 4% in the 150 GHz channel.

- In the 250 GHz data there seems to be a correlation between signal and IP – the higher the FFT peak at f_{chop}, the lower the IP. This inverse relationship between S/N and IP is consistent with the eccosorb results which may mean it is also related to saturation or non-linearity.

- For the future we must assess the angle of IP for each bolometer in addition to magnitude. This requires absolute encoding of HWP angle, referenced to a known coordinate system (e.g., cryostat coordinates). With this capability implemented, we will bin the polarized bolometer signal in HWP angle and extract IP angle from the phase of this plot. This technique has already been developed and demonstrated as reported in Sec. 4.9 for assessing differential polarization rotation.

4.9 Polarization Rotation

We define polarization rotation (PR) as the angular amount by which the orientation of polarized light incident on the primary mirror is altered as it traverses the optical system and is eventually measured by bolometers in the focal plane. This effect is shown schematically in Fig. 4.35 and is one which is particularly crucial to characterize in pursuit of our science goals – residual PR in the analysis pipeline can lead directly to E-B mixing and contamination of the inflationary B-mode signal derived from flight data. Although both *absolute* and *differential* PR will ultimately be determined with statistical analyses performed on the E- and B- mode maps made with flight data [47], we wish to make a preliminary assessment of differential PR with a suite of experiments applied during both cryogenic and integrated phases. We were unable to examine absolute PR during the NA campaign since this effort requires absolute encoding of HWP angle and we have yet to implement this capability.

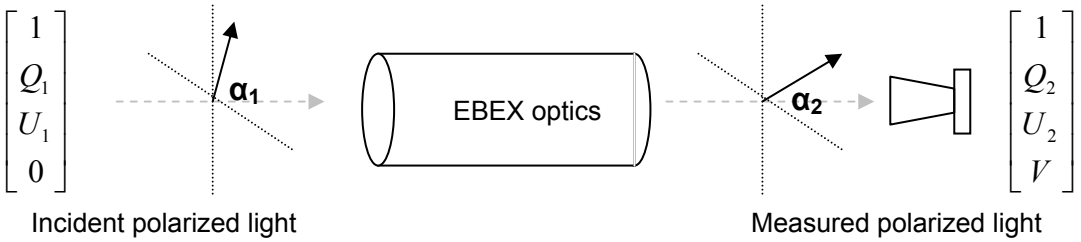

Figure 4.35: Conceptual illustration of polarization rotation. Bookends are Stokes parameter description of the phenomenon ($\alpha_1 \neq \alpha_2$).

The magnitude and orientation of this effect can be predicted as a function of focal plane position using our optical model of the EBEX optics [48]. PR arising downstream of the AHWP can be ignored as it will be approximately constant over time and therefore filtered out of the polarized signal of interest at $4f_{hwp}$. Having derived from our optical model the cumulative Mueller matrix (MM) for the elements sky-side of the AHWP,

$$MM = \begin{bmatrix} II & QI & UI & VI \\ IQ & QQ & UQ & VQ \\ IU & QU & UU & VU \\ IV & QV & UV & VV \end{bmatrix},$$

we can calculate PR as $PR = \frac{1}{2}\frac{QU}{QQ}$. In reference [49], Muckenhirn performs a Code V simulation with which he probes PR at each point over a 2 cm x 2 cm grid covering the entire EBEX focal plane. His results are plotted in Fig. 4.36, from which he derived an analytical expression for PR as a function of angle in the focal plane as projected on the sky:

$$PR(x, y) = [B \cdot y + A] \cdot x \ \ (deg) \tag{4.8}$$

where A = -1.67, B = 0.0067, with x and y correlating to azimuth and elevation, respectively. It is important to note that the coordinate system assumed in these simulations is inconsistent with our standard cryostat coordinates as defined in Fig. 4.1; everywhere else in this document we define the x-axis as corresponding to elevation on the sky, and the y-axis corresponds to azimuth. As Eq. 4.8 indicates and Fig 4.35 illustrates, we expect PR to vary by ~ 10˚ from one edge of the focal plane to the other along the azimuthal axis. In discussing empirical results throughout the remainder of this section we will assume B = 0 since it contributes only ~ 0.02° of rotation over the field of view associated with the three wafers installed during the NA campaign.

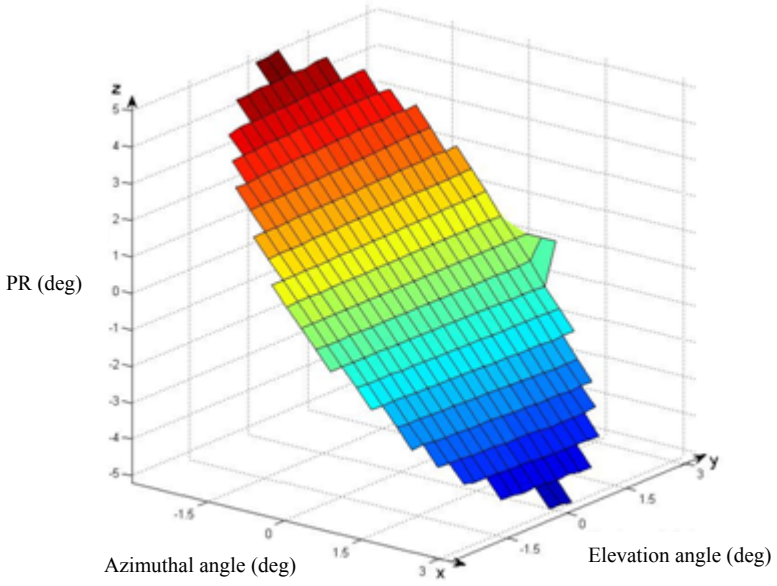

Figure 4.36: Predicted polarization rotation in the EBEX instrument as a function of focal plane position, derived from Code V simulation using a Mueller matrix model of the optical elements sky-side of the HWP [48,49].

4.9.1 Cryogenic Experiments

We have identified three separate experiments, each of which should generate a separate and independent assessment of PR inside the cryostat. Simulations indicate that PR in the EBEX telescope is generated almost entirely by reflections off the mirrors, therefore we expect to measure little or no differential rotation in these experiments which probe the cryostat alone. Each test diagramed in Fig. 4.37 requires a polarized input signal, which we accomplished using the same MAXIPOL external grid employed in the PME and IP experiments. We summarize each technique below, in ascending order of analytical complexity.

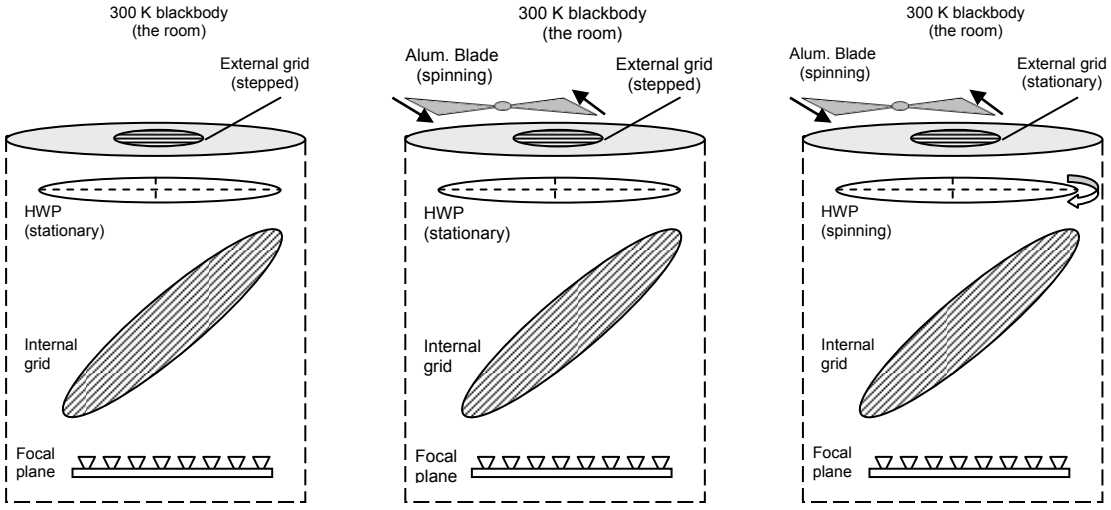

Figure 4.37: Three experiments proposed to investigate instrumental polarization in the EBEX cryostat. A 4th option – *DC input/spinning HWP* would also be effective but has not yet been attempted.

DC input/stationary HWP approach (Fig. 4.37, left): With the HWP set at an arbitrary position we rotated the HWP in 5˚ steps, recording by hand the ADC for a single representative bolometer at each step. We then plot detector response (a DC signal at each step) as a function of external grid angle, knowing the result should be a sinusoid. Fitting the data accordingly for all operational bolometers and extracting phase from the fit parameters, we could then map differential phase as a function of position in the focal plane. If a linear relationship emerges from this plot as expected, we can then immediately extract values for the coefficients *A* and *B* in Eq. 4.7. This procedure requires saving the bolometer and timestamp data electronically, and recording the index or timestamp range corresponding to each external grid orientation. In Ft

Sumner we performed this test and collected hand-written data for a single bolometer on each wafer, but failed to record timestamps or save the TOD electronically. Lesson learned:

- Record timestamps and save all data electronically during every experiment, regardless of whether or not any intent for future analysis exists at the time of execution.

Modulated input/stationary HWP approach (Fig. 4.37, middle): The experimental method here is identical to that used for PME (Sec. 4.6). We in fact analyze the same data set. In both cases the pipeline requires that we plot bolometer response (FFT peak at f_{chop}) as a function of external grid angle, and then fit the data to a *cos(2θ)* function. In attempting to extract PR, we determine the phase of the resultant sinusoid from the fit parameters as sketched in the left panel of Fig. 4.38. We then examine these values for multiple bolometers, mapping differential phase as a function of position in the focal plane. As mentioned in Sec. 4.6 we have thus far only analyzed the 150 GHz wafer, and in Fig. 4.38 we plot a preliminary assessment of rotation as function of bolometer position in the focal plane. Although we anticipated HWP phase would be independent of bolometer position, there is a clear trend implying a correlation between phase and position. Since the trend appears nominally linear, we have fit the data to a line – the slope of the best fit line is 8.3°/° (units = *degrees* of HWP phase per *degree* in the focal plane). Multiplying this value by 2 gives us the relationship in terms of differential polarization rotation, 16.6°/°. Not only is this result inconsistent with our expected DPR of ~0°/°, but it exceeds our expected DPR for the entire telescope by a factor of 10.

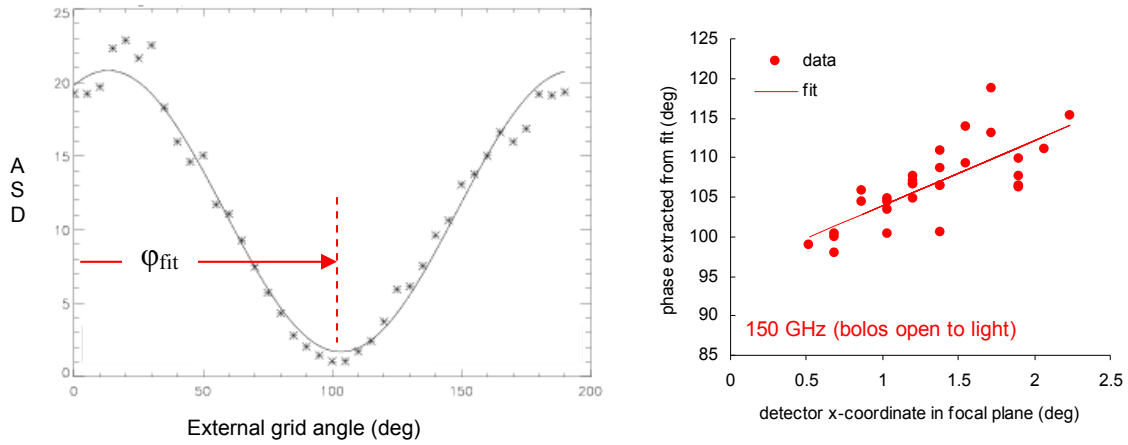

Figure 4.38: Preliminary assessment of differential PR in the 150 GHz band as a function of bolometer position in the focal plane. Left – Extracting phase based on minimum value of our *cos(2θ)* fit. Right – Preliminary results; slope of the best fit line is 8.3°/°.

Work is in progress to analyze the data at 250 and 410 GHZ, and further effort will be devoted to identifying any error introduced by our current pipeline. However, if we assume these preliminary results for 150 GHz are free of significant error from our analytical procedure, we have yet further indication of unexpected and significant polarized systematic effects in the 150 GHz band. We saw and discussed this phenomenon first in Sec. 4.7 where we calculated lower than expected PME, and then again in Sec. 4.8 where we found higher than expected IP. The trend seen in Fig. 4.38 is qualitatively consistent with our hypothesis of unanticipated PR and IP generated by the field lens and other non-AR-coated optical elements inside the cryostat.

Modulated input/spinning HWP approach: (Fig. 4.37, right) As the name suggests, with this technique we provide a modulated input signal at f_{chop} while simultaneously spinning the HWP at f_{hwp}. We collected one minute of data with the grid at each of four different orientations (relative to the x-axis in cryostat coordinates): 0˚, 45˚, 90˚ and 135˚. Changing the grid angle was done solely as a procedural check, a topic which will be revisited later in the section. For the ensuing discussion, the term *data* means a single minute of TOD collected with the external grid positioned at a single orientation. When observing this data in the frequency domain, many peaks are seen (Fig. 4.39). For this experiment we're interested only in the polarized sidebands of the modulated input signal, located at $f_{pol} = f_{chop} \pm 4f_{hwp}$.

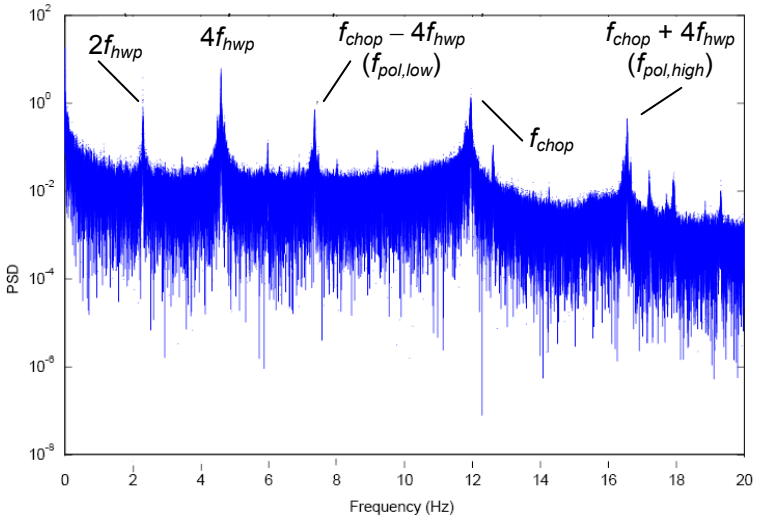

Figure 4.39: FFT from one minute of data collected during *modulated input/spinning HWP* polarization rotation experiment.

The ensuing analytical procedure is detailed in [58] and summarized here. The first step Klein takes is to isolate the polarized signal – this is done by converting the raw bolometer TOD into the frequency domain (FFT) and applying a bandpass filter about f_{chop}. Then transforming back into the time domain and normalizing, we use this vector as a lock-in reference signal, multiplying it by the whole raw data stream. Transforming back to the frequency domain, the polarized signal is now at $\pm 4f_{hwp}$. We apply a bandpass filter about $\pm 4f_{hwp}$ and transform back to the time domain where we then bin bolometer response in HWP angle. For the detectors with sufficient S/N and as anticipated, this result reveals clear evidence of a sinusoid with four periods spanning 360˚ of HWP angle.

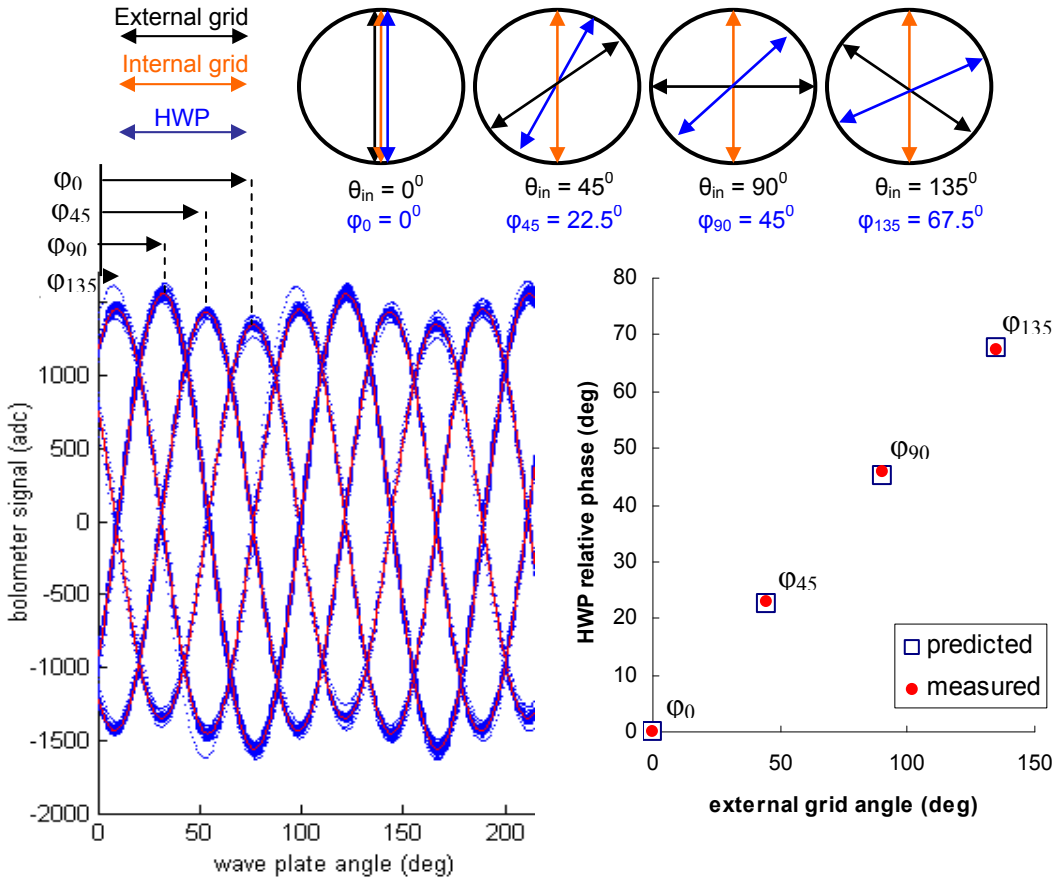

Figure 4.40: Top – Conceptual design of the four trials performed in this experiment, as if from top-down view into the cryostat. In each trial the HWP angle pictured is the angle at which bolometer signal will be maximized. Note that HWP angle is always ½ the external grid angle. Lower left – Blue dots represent bolometer data binned in HWP angle after filtering in frequency domain to leave only the signal at $f_{pol,low}$. Solid red curve is best-fit sinusoid. Four sets of data are shown corresponding to θ_{in} = 0˚, 45˚, 90˚, and 135˚ (measured relative to cryostat x-axis). Right – final step of analysis procedural check; knowing $\Delta\varphi$ should be ½$\Delta\theta_{in}$, we plot φ vs. θ_{in} and find that our measurements are consistent with expectations to within 1˚ at all points (note that this is a relative measurement: φ_0 is defined as zero by convention).

At this point we fit a $4f_{hwp}$ sinusoid to the binned data and perform our procedural check – for a single detector, we separately process the one minute of data taken at each of the four external grid orientations (θ_{in} = 0˚, 45˚, 90˚, and 135˚, relative to the grid axis of the internal polarizing grid). As diagramed in Fig. 4.40, the HWP angle at which the bolometer response will be maximized differs by *half* the angle by which the external grid is rotated, or $\Delta\phi = \Delta\theta_{in}/2$. Plotting φ (i.e., the phase of the sinusoidal fit) against θ_{in}, we not only verify that our analytical procedure produces the expected result, but we discover how accurately we were able to orient

our external grid (which was done by hand in Ft Sumner). An example of this analysis is shown in Fig. 4.40, which implies that in the latter 3 trials (θ_{in} = 45˚, 90˚, and 135˚) we positioned the external grid to within 1˚ of its intended orientation relative to θ_{in} = 0˚. With similar results obtained for each of the other two wafers, we claim confidence in the pipeline and proceed to analyze the rest of the data.

We have processed TOD from all 60 bolometers that were functional on the day these experiments were performed. In Fig. 4.41 we plot phase as a function of focal plane position. While the data at 250 and 410 GHz appear by eye to be consistent with expectations (negligible cryogenic DPR), there is a clear trend in the 150 GHz plot. We have calculated a linear fit to these data which gives a slope of 3.3°/°. To convert this slope into differential PR, we must multiply by 2 which gives DPR = 6.6°/°. This result qualitatively agrees with the trend identified in the 150 GHz *modulated input/stationary HWP* data. Although the best-fit slope in Fig. 4.38 is 8.3°/° and here we find 6.6°/°, both values deviate significantly from the expected 0°/° and provide further support of our hypothesis regarding an unanticipated level of PR and IP in the uncoated field lens and other cryogenic optics.

The fact we see a strong correlation between PR and bolometer position in the 150 GHz data and none in the other two wafers seems to contradict our model – we would expect the effect to be more subtle at 250 and even less at 410 GHz, but not zero. We could argue that the effect may be present but unidentifiable due to the smaller sample sizes, slightly greater variance, and lesser angular extent in the focal plane probed in the higher frequency channels. More data in these bands would offer greater statistical confidence and should be available after executing this experiment in the future with more operational detectors.

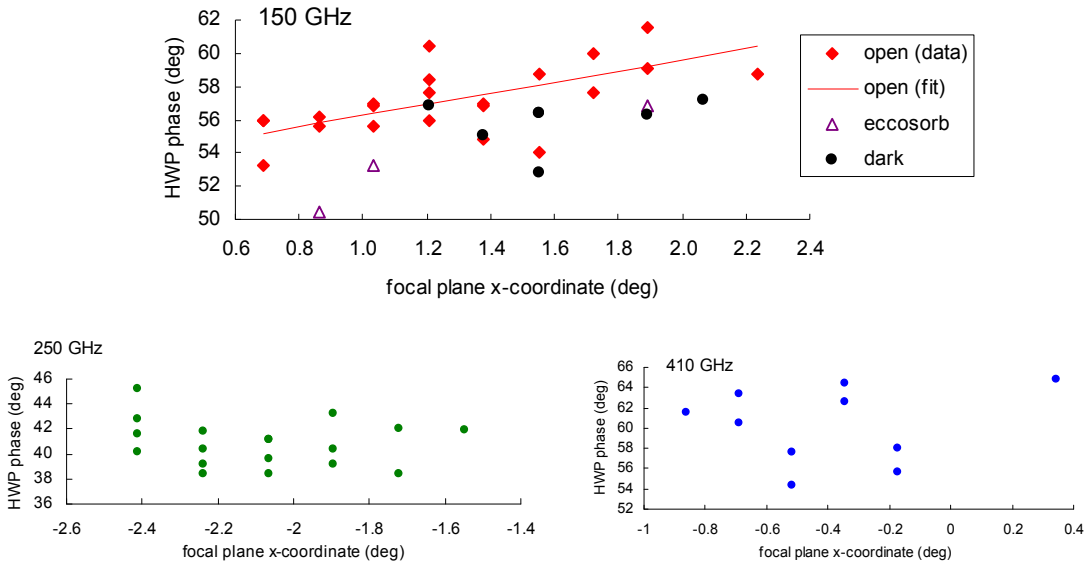

Figure 4.41: Preliminary results, differential polarization rotation as a function of bolometer position in the focal plane from *modulated input/spinning HWP* technique. HWP phase values shown on the y-axes are arbitrary. Data points in 250 and 410 GHz plots are all from bolometers open to light.

Since we have simulations indicating PR will vary as a function of frequency and we have yet to make an experimental assessment of this effect (see Sec. 4.9.3), we have refrained from plotting all three wafers together on the same set of axes. By eye we can see that the average HWP phase in the 150 and 410 GHz plots of Fig. 4.41 appear similar (~ 58°) while the 250 GHz average phase is more like 42°. Without more information this comparison carries little meaning, but such inter-band analysis will be an important product of future iterations of this experiment. This will be particularly true once we have implemented an absolute HWP encoder, since results derived using this approach should be consistent with direct testing of PR spectral dependence as described in Sec. 4.9.3.

4.9.2 Integrated Experiments

We performed a trio of integrated tests with a fully polarized, modulated signal generated at the artificial planet. Since the signal now traverses the entire optical system including the mirrors, we can directly compare results of these experiments with the PR model derived from simulations and captured in Eq. 4.8. The techniques are discussed below. In all three cases, the modulated

AP signal was polarized by mounting the MAXIPOL grid within the center aperture of the AP primary as pictured in Fig. 4.42.

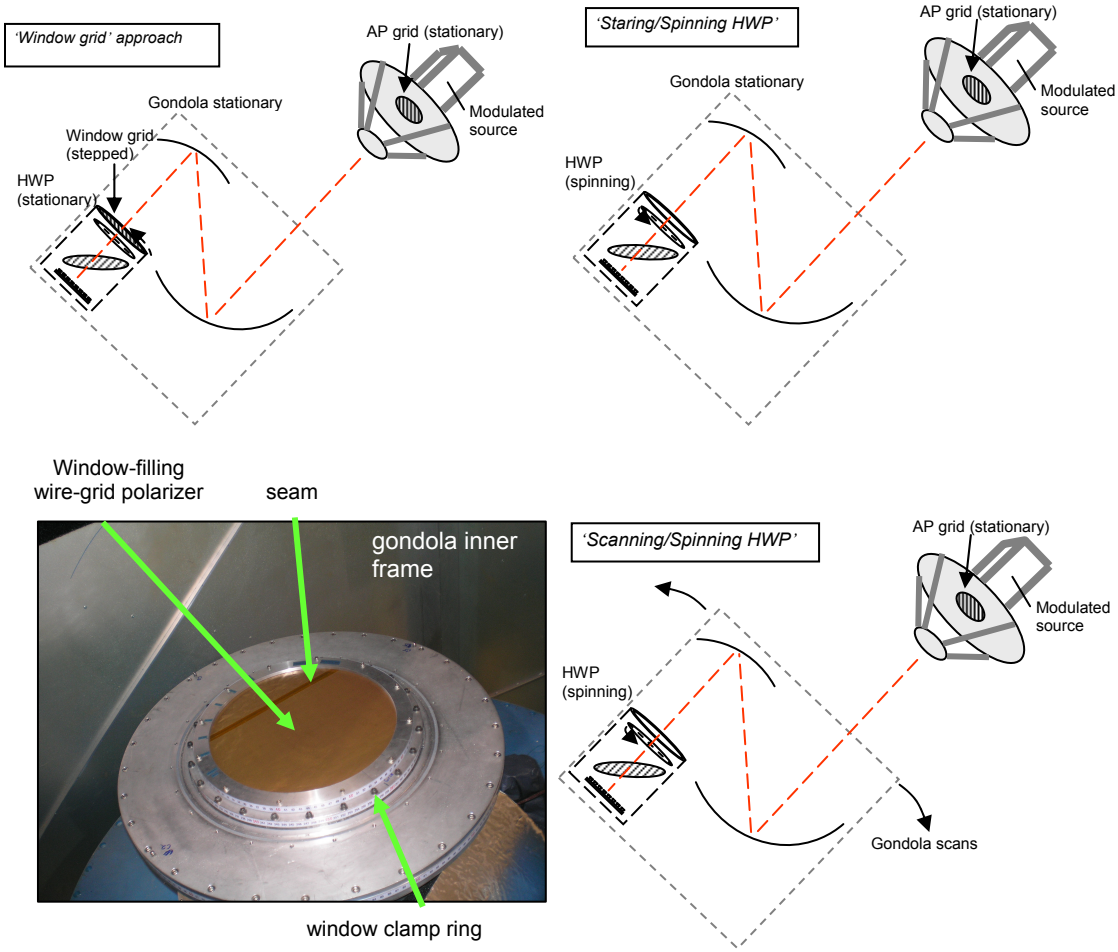

Figure 4.42: Three experiments to investigate PR in the fully integrated telescope.

Window Grid approach: (Fig. 4.42, upper left) This technique was the first of the three integrated experiments executed in Ft Sumner – it offers an opportunity for quick-look results since we simply write down the data in a notebook (although in future iterations the data should be saved for further analysis). We mounted a polarizer at the cryostat window, held the HWP stationary at an arbitrary position, rotated the window grid in steps and plotted bolometer response as a function of grid angle. Since it is the input polarization angle we are varying - the HWP remains stationary - we can directly read differential PR from phase offsets measured between different bolometers.

We constructed a circular polarizing grid from sheets of kapton with copper traces at 50 μm wide and with 50 μm center-to-center spacing. Aiming to span the full 13.5"-diameter cryostat window with this device, we had to splice two pieces together because the raw material came in 9" x 13" sheets. We placed the seam as far off-center as possible, as shown in Fig. 4.42. The two pieces are held with kapton tape and measuring through a microscope we have verified that the grid lines are aligned to better than 0.5˚ between pieces. The resultant spliced sheet was then tensioned between two aluminum rings and glued in place with Epoxy 907.

The grid was seated in the cryostat window's clamp ring with a step on the underside of it to facilitate rotational movement without lateral slippage. We stepped the grid manually, which required an individual be standing on the gondola's inner frame throughout the experiment. We performed this test three times. In our first attempt we used the EFM with ½" exit aperture and aluminum plate in place of a diffraction grating. Because the AP was in point-source configuration, we probed only two bolometers and had to move the gondola to re-align on the second detector between data sets. Aiming to measure the largest DPR possible, we chose the available bolometers with maximum separation along the cryostat's y-axis. We used 410 GHz bolometers 3-09 and 8-02, which are separated by 1.9˚ along this axis. In both cases we stepped the window grid a total of ~ 135˚ in 5˚ increments, and then made higher resolution measurements about angles where we identified the maxima and minima. To these data we fit a $cos^3(\theta_{grid})$ function, since this is the form expected for an experiment in which the modulated signal traverses three polarizing grids. The fits are consistent with the data as shown in Fig. 4.43, and the relative phase difference between the two detectors is 3.2˚. Given that Δx = 1.9˚ for these bolometers, Eq. 4.8 predicts $PR = 1.6 \cdot 1.9^0 = 3.2^0$. Therefore, our measurement agrees precisely with the predicted value.

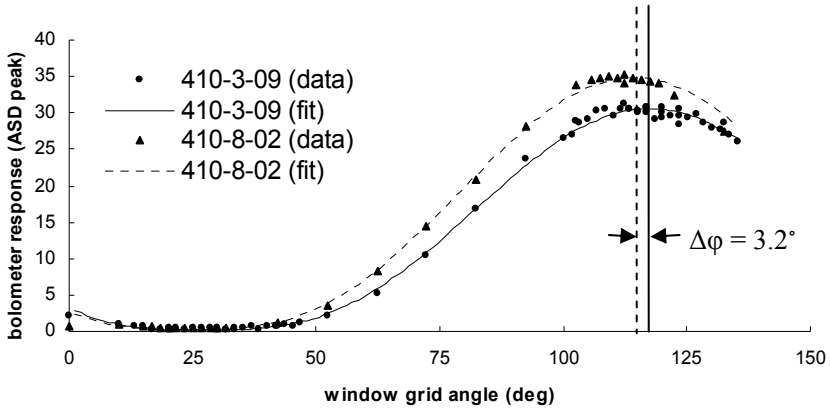

Figure 4.43: Data and best fit $cos^3(\theta_{grid})$ function from *window grid* PR experiment, trial #1 (410 GHz wafer).

We attempted the experiment once more, this time using the 250 GHz wafer and employing the AP in its *extended source* configuration as sketched in Fig. 4.44. This was done to investigate the possibility of collecting data over a whole wafer simultaneously. The approach would hypothetically offer a significant time-savings advantage primarily because of eliminating the need for re-aligning the gondola on different bolometers. During this test we rotated the window grid a total of 190˚ and recorded by hand the FFT peak at f_{chop} for bolometers 250-6-03 and 250-11-09 ($\Delta x = 1.6$˚). The measurements are shown in the right panel of Fig. 4.44 and reveal a significant divergence from the data collected with the point source approach which were accurately fit with a cos^3 function as seen in Fig. 4.43. Though we are unable to produce a fit or make a reliable assessment of relative phase offset, with the data alone and by eye we see evidence for an offset that seems consistent with expectations.

A physical origin for the steep rise to the left of the peak and the much shallower tail seen to the right of the peak requires further contemplation. Our preliminary and qualitative hypothesis centers around aberrations resulting from performing the experiment with the AP in its extended source configuration – because we aimed to probe detectors on opposite edges of the wafer and for this test we nominally aligned the gondola with the center of the wafer, the beams of the two bolometers plotted in Fig. 4.44 likely traversed the AP at an angle off-axis by ~ 1°. More detailed simulations are required to assess whether or not this hypothesis has merit.

It is also possible that the unexpected shape in Fig 4.44 is unrelated to the AP configuration or experimental procedure but is instead due to a real systematic effect in the 250

GHz band which didn't exist in the 410 GHz band. While we have yet to derive a specific model to account for this particular phenomenon, earlier results indicate a correlation between frequency band and the magnitude of polarized systematics. Further modeling and simulations should be performed to search for an explanation that rectifies the data plotted in both Fig. 4.43 and 4.44.

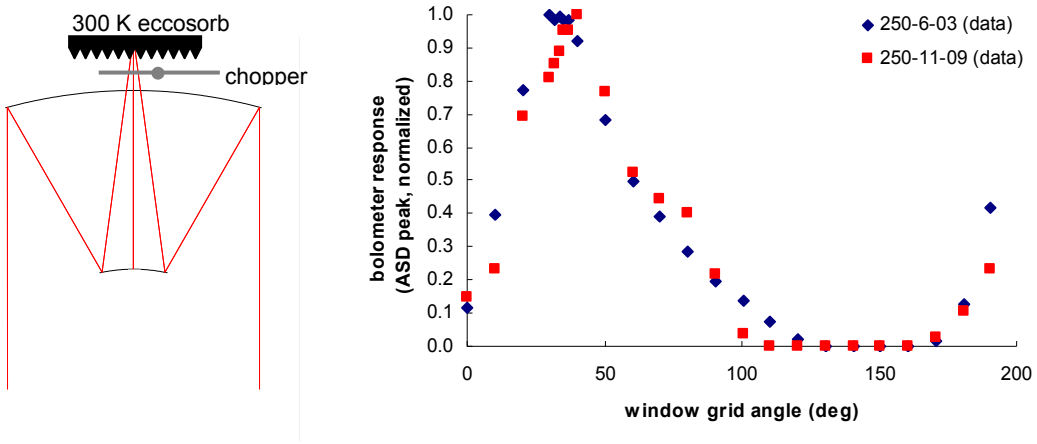

Figure 4.44: Left – Schematic of artificial planet in *extended source* configuration; chopper blade occults entire central aperture of AP primary mirror, providing an image of modulated signal across ~2˚ in the EBEX focal plane. Right – *Window grid* experimental data, trial #2 (250 GHz wafer).

Staring/Spinning HWP approach (Fig. 4.42, upper right): This experiment is identical to the cryogenic *modulated input/spinning HWP* approach, except test now includes contributions from the primary and secondary mirrors. For this test we again used the AP in extended source mode as described in the previous subsection and illustrated in the left panel of Fig. 4.44. We collected two independent sets of data, in both cases aligning the gondola by hand on the ground to approximately the center of the 250 GHz wafer FOV. In both trials we had f_{hwp} ~ 1.2 Hz, f_{chop} ~ 11.5 Hz, and therefore $f_{pol,low}$ ~ 6.7 Hz. f_{chop} and $f_{pol,low}$ peaks were evident in the 10-second FFT display for many 250 GHz bolometers spanning virtually the entire angular extent of the wafer. These data sets have not yet been analyzed, but will be investigated using the same procedure described for the modulated input/spinning HWP experiment above. We must however also note that during these tests we did not take separate data sets with varying input polarization vectors (i.e., AP external grid position angles) as necessary to facilitate a pipeline procedural check. Having successfully demonstrated the check on our cryogenic data sets we now realize its value and recommend implementing this step in all future PR experiments employing a spinning HWP.

Scanning/Spinning HWP approach (Fig. 4.42, lower left): This technique is identical to the previous one except that data is collected while scanning the gondola. It presumably offers greater efficiency – a single data set could be gathered covering all bolometers on all wafers in less than an hour – but at the cost of increased analytical complexity as it involves deconvolving the beams (and perhaps bolometer time constants as well). In Ft Sumner we executed the following experiment: with the extended AP source in place, we aligned the gondola in elevation on the 410 GHz wafer. The gondola was then commanded to make 10 scans at each of 3 different elevations separated by 0.5˚ with an azimuth throw of 4˚ for each scan. We then increased the gondola elevation by ~ 2˚ to align with the elevation plane of the 150 and 250 GHz bolometers and repeated this procedure, this time using a 6˚ azimuth throw in an attempt to sweep across the full FOV covered by these two wafers. Again we witnessed peaks at f_{chop} and f_{pol} in the real-time FFT for several bolometers. We have yet to analyze this data set but at this point anticipate that the gain in experimental efficiency is marginal in light of the greater analytical challenges inherent to this technique, and recommend the staring approach as a baseline for future implementation.

4.9.3 Polarization Rotation as a Function of Frequency

As stated in this section's introduction, simulations predict that PR in the instrument will vary as a function of frequency. The model derived from these simulations is depicted in Fig. 4.45 and indicates that the magnitude of this effect differs in each band. The y-axis of this plot refers to differential HWP phase ($\Delta\varphi_{hwp}$); as we have discussed and used earlier, $\Delta PR = 2 \cdot \Delta\varphi_{hwp}$. Therefore the plot implies that PR could vary by 14˚ from one edge of the 150 GHz band to the other, and almost 18˚ across the 410 GHz band [45]. It is important to note that the simulations include only the AHWP and assume that the spectrum of the input signal is flat. The results of our experiment will include effects from all cryogenic optical elements, and the input signal spectrum is that of the Ebert-Fastie monochromator which we expect to be far from flat (see Fig. 3.9). Therefore, a direct comparison between measurements and currently available predictions is unwarranted. The simulations should be re-run after amending the code to allow for an EFM-like input spectrum, and if possible, include the rest of the uncoated optical elements as well.

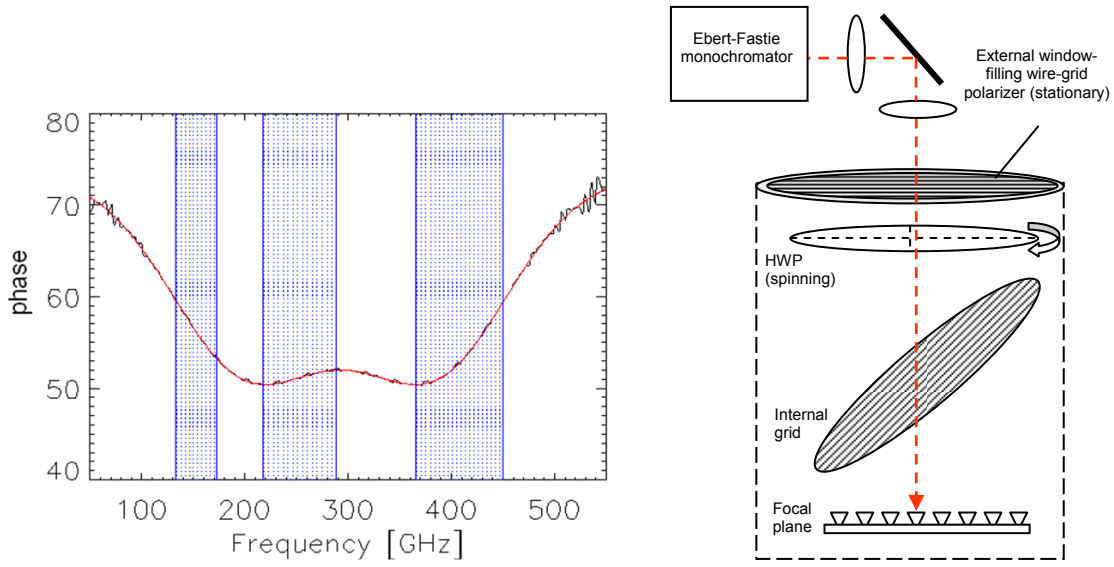

Figure 4.45: Left – Polarization rotation as a function of frequency, PR(ν), due to AHWP properties as predicted by simulations [45]. Right – Conceptual design, PR(ν) experiment implemented in Ft Sumner.

The right panel of Fig. 4.45 shows our experimental design – we collected one set of data for one bolometer in each band, performing this PR(ν) test immediately following the relative spectral response experiment (since the EFM was already properly aligned with a target bolometer). With the HWP rotating continuously, we integrated for 2 minutes at each monochromator setting. We stepped the grating through the band 7 consecutive times with the external grid's transmission axis set at different angles relative to the cryostat x-axis: 0˚, 30˚, 45˚, 60˚, 90˚, 120˚, and 150˚. Again, PR(ν) can be fully assessed at any particular grid angle; varying the orientation simply provides a procedural check. The pipeline used to analyze these data is identical to what was described above for the cryogenic *modulated input/spinning HWP* experiment. In Fig. 4.47 we plot an example of our procedural check at 410 GHz, which show consistency between measurements and predictions.

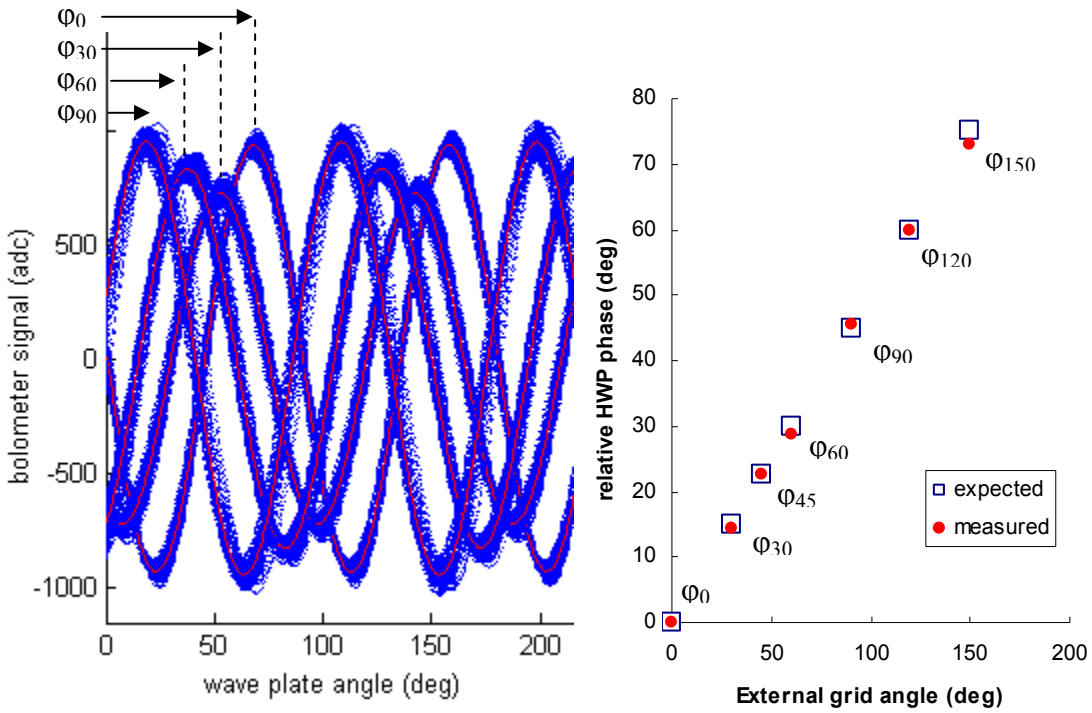

Figure 4.46: Analysis procedural check for PR(ν) experiment (example shown is with 410 GHz data). Left – φ_{30} represents relative HWP phase angle when input polarization angle (i.e., external grid orientation) θ_{in} = 30˚. Data (blue) and fit (red) only plotted for 4 of 7 total θ_{in} to avoid overcrowding plot. Right – Relative HWP phase (φ) as function of θ_{in}, results similar to those found in Fig. 4.40.

We have yet to assess the 150 and 250 GHz channels, but have analyzed all of the available 410 GHz data and plot PR(ν) for 4 of the 7 input polarization angles. The other three data sets were excluded due to anomalous features appearing in at least one of the five 2-minute integrations. A leading hypothesis for the cause of these anomalies is dropped packets – we noted several instances of packet loss while viewing the TOD in real-time and these seem to correlate well with the affected data sets. Preliminary results are plotted in Fig. 4.47 and imply the absence of any correlation between PR and frequency. While we can't make a direct comparison with the model depicted in Fig. 4.45, this result is somewhat surprising considering that the model predicts $\Delta\varphi_{hwp} \sim 6°$ over the frequency range tested. A valid comparison requires new simulations, but to first-order we would expect our measurement of $\Delta\varphi_{hwp}$ to *exceed* that predicted in Fig. 4.45 considering the nature of the difference between flat and EFM input spectra. Analysis of the 150 and 250 GHz data sets is under way, the results of which should help clarify our understanding of the 410 GHz measurements.

Given the consistency between measurements and predictions seen in our procedural check, we have little reason to suspect major problems with the analysis pipeline and are therefore inclined to search for a physical origin to these unexpected results. The lack of correlation between frequency and PR could be yet another manifestation of unanticipated PR and IP in the instrument due to lack of AR-coating on the cryogenic optics. However, it is also possible that certain aspects of the experimental procedure contributed to this result: (1) the EFM exit aperture was set to ¾" in an effort to maximize S/N but this would have also produced atypically wide window functions which may have effectively washed out any underlying spectrally-selective response, and (2) our lever arm on the effect was reduced due to the narrow range of grating angles (and hence frequencies) that were used (28˚-32˚ instead of the 24˚ – 36˚ probed during the spectral response campaign). The narrow grating range was implemented to save time. Since we measured high S/N and realize that only 3 or 4 external grid angles are necessary to facilitate the procedural check, we recommend using a smaller monochromator exit aperture, lesser integration time, more grating settings, and fewer external grid positions.

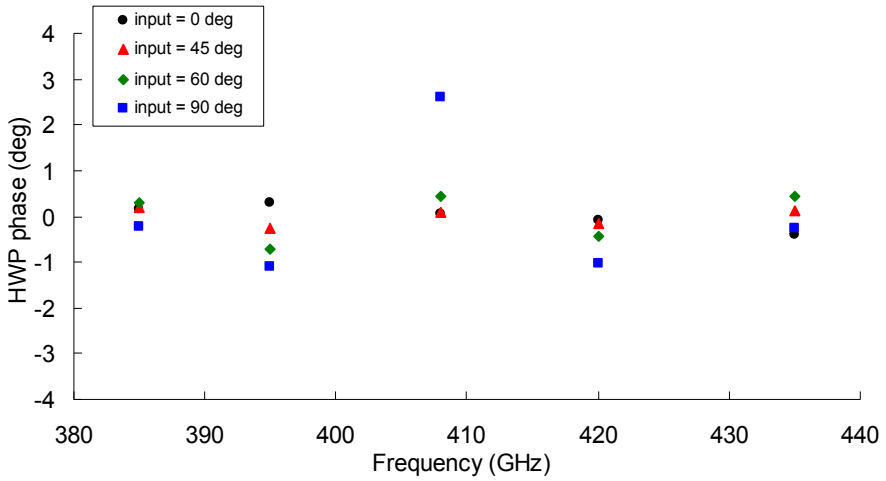

Figure 4.47: Preliminary experimental results for PR(ν) in one bolometer at 410 GHz.

4.10 Far Sidelobe Response

In Sec. 4.4 we discussed mapping the on-axis antenna response, or main beam. While the telescope is designed for maximum gain within this main beam and to first-order we presume zero sensitivity at large angles from this axis, we know from experience and modeling that the

instrument's far sidelobe response will be finite and non-zero. This is due primarily to diffraction around the primary mirror and reflections associated with the baffles, but in principle can be caused by light scattering off any gondola surface that then finds its way to the focal plane. If the far sidelobe sensitivity exceeds a certain threshold and during flight is scanned across a bright astronomical source (Sun, moon, Galaxy, etc.), a non-negligible scan-synchronous signal could leak into the bolometer TOD. Unaccounted for, this signal will be interpreted as originating on-axis, thereby causing us to overestimate sky brightness in the main beam pointing direction. This could then propagate through the analysis pipeline as an overestimate of the dust signal (in the case of far sidelobe contamination in the 410 GHz band, for example), which would introduce error in our foreground subtraction and ultimately in our CMB maps. The effect may be amplified for the case of polarization – far sidelobe contamination from a polarized off-axis source (and/or inherent polarization in the far sidelobe response itself) could represent an even greater fraction of the signal we're after since E-modes lie an order of magnitude below the temperature signal but B-modes are at least another order of magnitude below that.

The qualitative argument outlined in the previous paragraph is quantified by Milligan in ref. [50]. Based on a GRASP8 model of EBEX, assuming our nominal CMB scan strategy and extrapolating astronomical emission characteristics (brightness/polarization) to the EBEX bands from WMAP observations, he concludes that the Galaxy is the greatest potential source of spurious scan-synchronous polarized signal. He also investigates two different baffling strategies – reflective and absorptive – determining absorptive baffles to be superior for far sidelobe suppression. Taking a worst case scenario of reflective baffling where the most egregious possible polarized far sidelobe falls on the galactic center, he calculates that the signal from sidelobe B-mode contamination will be equal to the inflationary B-mode signal assuming $r = 0.02$ if the far sidelobe sensitivity exceeds -85 dB of the main beam response. Even though we employed absorptive baffles for the NA flight which theoretically completely nullify sidelobe sensitivity, we retain -85 dB as the threshold to which we must determine (or exclude) far sidelobe response.

An experimental determination of response level spanning almost 9 orders of magnitude requires a powerful mm-wave emission source. We procured a 127-150 GHz tunable Gunn oscillator from J. E. Carlstrom, Inc., capable of producing monochromatic flux between 7 and 21 mW dependent on frequency. Seeking to optimize output power with an emission frequency as close to the center of the 150 GHz band as possible, we tuned the device to 145 GHz which generates 15 mW according to the test data. A WR-6 pyramidal horn coupled to the oscillator

generates a polarized f/8.8 beam (~7˚ FWHM). We modulated the source mechanically, inserting a chopper blade in front of the horn. Both the chopper and source were mounted inside an eccosorb-lined aluminum box to prevent modulated signal leakage (see Fig. 4.48) and placed on a standard camera tripod for azimuth and elevation control.

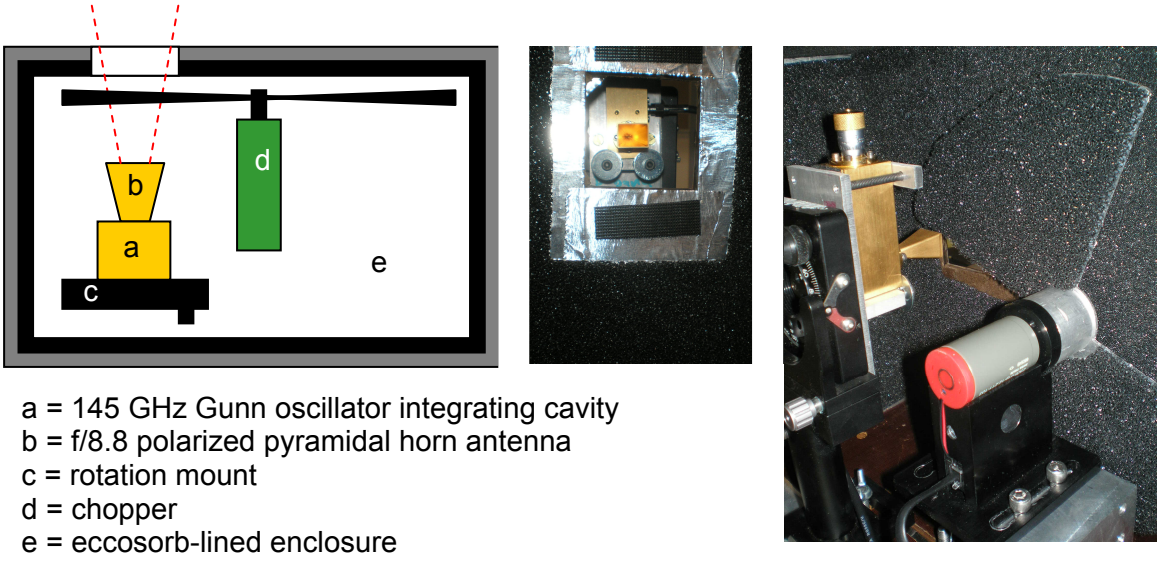

Figure 4.48: Left – Modulated high-power mm-wave source used for far sidelobe experiment. Middle photo – Front view of exterior, source visible through enclosure aperture. Right photo – Interior view of enclosure (back panel temporarily removed).

Given the gondola's lower elevation limit and our desire to overfill the primary mirror with the oscillator beam as much as possible to best simulate a far field source, we placed the source on a mechanical boom lift and positioned it relative to EBEX according to the layout shown in Fig. 4.49.

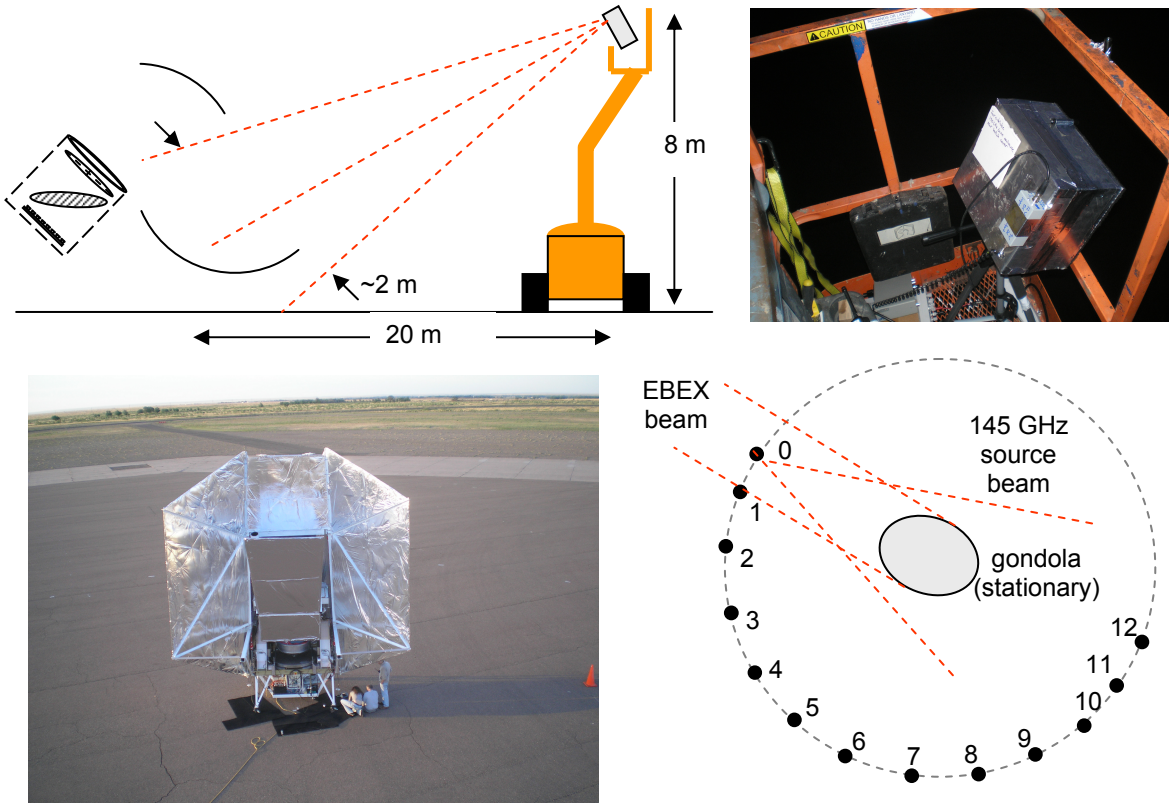

Figure 4.49: Far sidelobe experiment as implemented on the launch pad at CSBF, Ft Sumner. Top left – Gunn oscillator source points down at gondola, f/8.8 oscillator beam overfills primary mirror by a factor of ~2. Top right – Source on tripod in cherry picker basket. Bottom left – Gondola on launch pad as viewed from cherry picker basket. Bottom right – Positions of source during collection of azimuth cut data.

The first of two far sidelobe tests performed in Ft Sumner occurred the morning of 20 May 09. For both tests the AHWP was stationary and at an arbitrary position angle. We roughly aligned the oscillator beam with the primary mirror using a pen laser mounted on the source enclosure. Then turning the source and chopper on, we immediately saw a large modulated signal at the chop frequency and more accurately aligned the system by adjusting both the gondola (elevation only) and source (azimuth and elevation) to maximize this signal. Throughout this test the polarization axis of the Gunn oscillator beam was roughly set at perpendicular to the ground and we did not attempt to adjust it for further gain during the alignment procedure. At this stage the source must be attenuated since 15 mW at 145 GHz saturates the 150 GHz (and perhaps all) detectors despite imperfect beam coupling. Weeks earlier we tested various candidate materials using for their mm-wave attenuation properties with the artificial planet. We tried various types and thicknesses of foam, paper, wood and cardboard, occulting the entire

modulated AP beam with the test article and measuring the corresponding reduction in bolometer signal. Cardboard was deemed the preferred material, providing a consistent 4x decrease in the FFT peak at f_{chop} with each additional piece.

As usual we identified a representative 150 GHz bolometer and observed a peak-to-peak signal in the time domain of 650 ADC at gondola elevation = 21.5˚ with 54 dB of attenuation (9 pieces of cardboard, assuming a factor of 4 attenuation per piece). We then stepped the gondola through the available elevation range, recording by hand the time domain peak-to-peak at each position. At 23.5˚ elevation we removed 4 of the 9 attenuators and measured 7 ADC peak-to-peak. At 25.5˚ (4˚ from on-axis), the remaining 5 pieces were removed and beyond this point the signal quickly faded into the noise. After completing the elevation cut, we moved the gondola back down to 21.5˚ elevation and executed an azimuth cut. This involved driving the lift in a semicircle around the gondola, making 13 stops along the way where this we recorded the FFT peak at f_{chop} ~ 5 Hz. The results of both cuts are plotted in Fig. 4.50. One obvious feature is the stronger rejection floor in the azimuth cut, caused simply by recording peaks in the FFT instead of working in the time domain (higher S/N in the frequency domain). The elevation cut data is on file and could be processed in the frequency domain if deemed necessary. However, we conclude from these results that far sidelobe rejection indeed meets or exceeds the -85 dB benchmark.

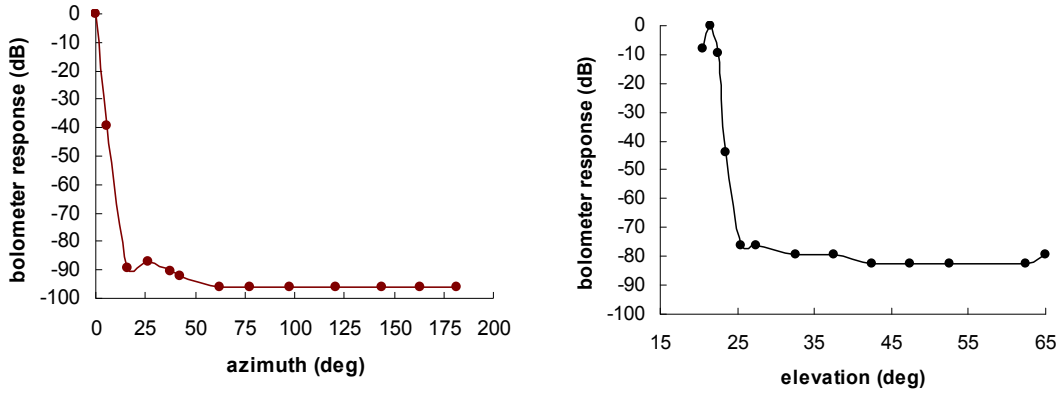

Figure 4.50: Experimental results from low resolution, unpolarized far sidelobe experiment. Left - Azimuth cut, response drops to < -85 dB at ~ 15˚ from main beam. Right - Elevation cut, response drops to < -80 dB at ~ 5˚ from main beam.

A second test was performed on 28 May 09 where we followed a similar procedure but this time collected data points at higher angular resolution in the vicinity of the main beam. In

this iteration we also took two data points at location – one with the oscillator's polarization angle nominally parallel to the telescope's (arbitrary) polarization axis, and the other with the oscillator's polarization vector perpendicular to the telescope. We hereafter refer to the parallel orientation as 'co-polar', and the perpendicular orientation as 'cross-polar'. The co-polar position was determined during the initial alignment process as the source rotation angle which maximized signal in the frequency domain of our target bolometer, which proved to be 225 ASD/√Hz with12 cardboard attenuators in place (at elevation = 17.9˚). Results of the subsequent azimuth and elevation cuts are shown in Fig. 4.51. With higher resolution we were able to more accurately identify the angle at which response drops below our -85 dB benchmark: approximately 5˚ off-axis in the elevation cut and 12˚ in the azimuth cut. As expected, the cross-polar response is consistently measured below the co-polar response. But the separation varies significantly as a function of angle. Since we have neither a quantitative determination of the oscillator's true polarization fraction nor a prediction for the polarized sensitivity of the full gondola, we simply conclude that the polarization data reveal nothing new or alarming about the telescope's far sidelobe response.

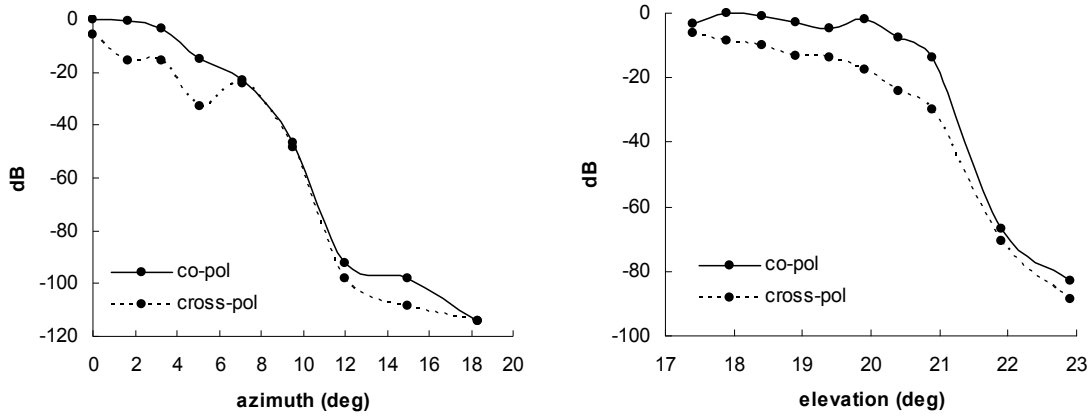

Figure 4.51: Results from high resolution far sidelobe experiment. Left - Azimuth cut, response drops to < -90 dB at ~ 12˚ from main beam. Right - Elevation cut, response drops to < -80 dB at ~ 5˚ from the main beam. Both data sets are nominally consistent with low-resolution results shown in Fig. 4.50.

Although the primary outcome of these tests is reasonable confidence that far sidelobe response meets specifications (as expected given the use of absorptive baffles), we also learned that this experiment leaves room for significant improvement. Here are the most obvious issues and opportunities to be considered in preparation for LDB:

- Near the end of the 28 May test, we moved the gondola -2˚ in azimuth from the presumed on-axis position and discovered that the signal increased by a factor of ~ 200 (16 attenuators required at this position vs. 12 at the position labeled 0°). Furthermore, we had only 9 attenuators in place for maximum signal at the supposed on-axis position during the 20 May test. These insights imply bolometer non-linearity, but also hint that we missed the true on-axis position with our alignment strategy and/or didn't fully understand the cardboard's mm-wave attenuation properties. It was also true that stacking up to 16 pieces of cardboard in series was awkward at best, likely introducing variable effects due to gaps, sag, and other coupling anomalies. While we don't think this information necessarily undermines our conclusions, it does suggest consideration of some key hardware and procedural upgrades: pending financial resources, a devoted micrometer-based mechanical mm-wave attenuator should be installed between the oscillator cavity and horn antenna to ensure full control (and knowledge) of attenuation level throughout the experiment. Also, we overestimated the reliability of the laser alignment and in future attempts should more thoroughly probe azimuth space in the search for maximum bolometer response.

- Insufficient preparation and avoidable scheduling inefficiencies limited the breadth and depth of sidelobe data acquired during the Ft Sumner campaign. The telescope was typically rolled out of the high bay at ~2 am, bolometer tuning and baffle installation delayed the onset of data acquisition until ~5 am, and increasing wind speed forced the cessation of operations between 7 and 8 am. 2-3 hours over two nights proved woefully short of the time truly required to perform a comprehensive sidelobe investigation. If executed again in Palestine prior to LDB, the process should begin much earlier (as early as allowed by wind conditions) and more effort should be devoted to pre-rollout gondola preparation. With these measures the window for data collection could probably be doubled.

- Again pending financial considerations, purchasing a frequency doubler (installed between the oscillator cavity and horn) would allow the determination of sidelobe

response in a second spectral band: 127-144 x 2 = 254 – 288 GHz, well within the 250 GHz channel.

5 Preparing for LDB

5.1 North American Test Flight

The first EBEX test flight occurred 11 Jun 2009. The telescope was launched from Ft Sumner, NM and terminated near Lake Havasu City, NV after ~10 hours at a float altitude of ~118,000 ft. Fig. 5.1 includes a diagram of the flight path and photo of the telescope shortly before launch. This marked the first time TES bolometers were used in a non-terrestrial environment as well as the first balloon-borne application of a SMB for HWP rotation. Bolometer TOD observed in real-time through the telemetry link showed a persistent sinusoidal signal at the expected HWP template frequency, implying qualitatively that both systems were in operation throughout the flight. Analysis of the flight data is under way, including an effort to extract useful calibration results from a Saturn scan (beam mapping) and a CMB dipole scan (absolute flux response, instrumental polarization).

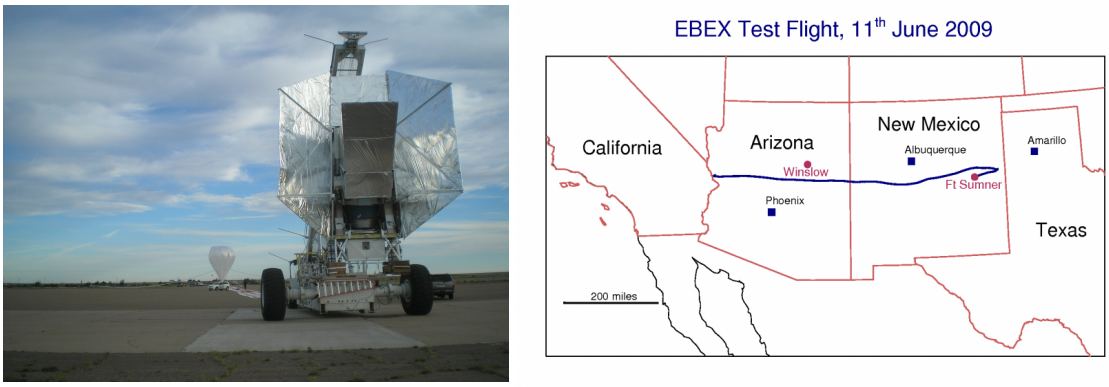

Figure 5.1: Left - EBEX on launch pad in Ft Sumner just prior to North American test flight. Right – Ground trace of flight path.

With Jupiter and Mars both excluded by our ± 45˚ anti-sun pointing constraint, Saturn was the brightest astronomical point source available for in-flight beam mapping. Our baseline scan strategy included small positive elevation steps after each azimuth scan to follow the object as it rose in the sky, meant to ensure all beams would densely sample Saturn in both azimuth and

elevation to facilitate the generation of high resolution 2-D beam maps. After elevation control was disabled at launch, we implemented a modified calibrator scan with a 5˚ azimuth throw and 1˚/sec slew rate.

Our original plan to identify the Saturn signal in real-time and perform a 'quick-look' beam analysis was predicated on applying a digital low-pass filter to the real-time TOD with a cutoff below $2f_{HWP}$ to eliminate the dominant HWP template signal. However, we realized shortly before flight that assuming 8' beams and a 1˚/sec slew rate, each beam crossing will generate a spike in the timestream lasting just 133 ms. This is equivalent to a single period of a 7.5 Hz signal. Not only is this nearly coincident with the $4f_{HWP}$ (~8 Hz) signal, but applying a low-pass filter at $< 2f_{HWP}$ (~4 Hz) excludes the planet signal with the template. Therefore, without a real-time template removal capability, we observed the bolometer timestream by eye in an attempt to identify planet crossings above the HWP signal. None were observed. A post-fight template removal code is complete and will be used in a forthcoming attempt to characterize the beams from flight data.

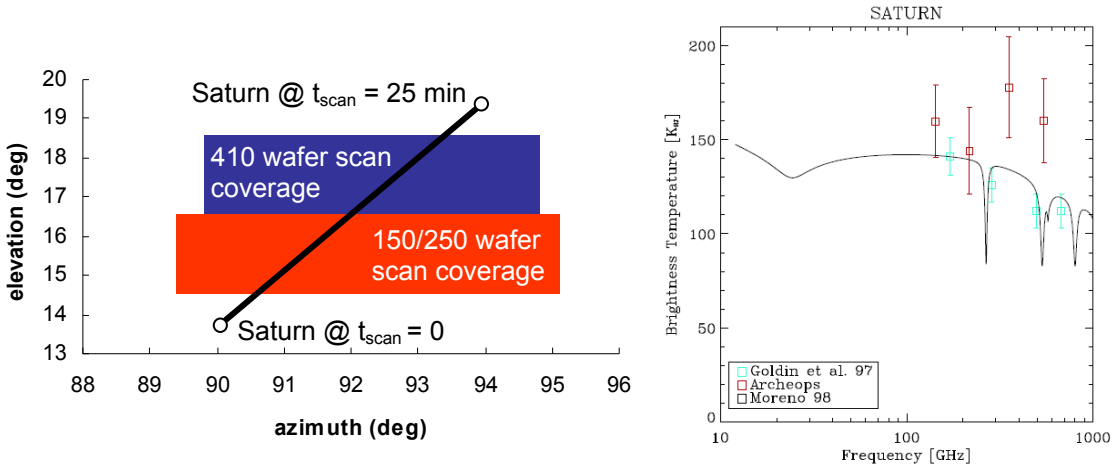

Figure 5.2: Left – EBEX NA test flight Saturn scan coverage assuming best-case scenario (i.e., scan centered at 16.5˚ elevation,0 92˚ azimuth). Analysis to determine true pointing is under way. Right - Saturn mm-wave flux measurements (data points) and theoretical model (solid line) from [51].

The Saturn scan was initiated at UTC 19:32 and terminated at 19:57, over which time the planet drifted in elevation from ~ 14˚ to 19˚ and in azimuth between ~ 90˚ and 94˚. If we assume an ideal scenario where the observations were initiated with the active focal plane centered at 16.5˚ elevation and 92˚ azimuth, the left panel of Fig. 5.2 gives a portrayal of the scan in terms of

focal plan coverage. Given Saturn's ~0.2˚/min drift in elevation and assuming 8' Gaussian beams on each wafer, the planet should cross within each detector's FWHM approximately 6 times. However, our confidence in absolute pointing accuracy at this time was marginal, and we must await further analysis to determine how closely the actual scan resembled the ideal case assumed here. Also, preliminary results from ground-based beam mapping imply the possibility that our beams were wider than 8'. If true, each beam would record more than 6 planet crossings. However, wider beams also have an impact on S/N, as we detail below. The right panel of Fig. 5.2 shows observational data and a model of mm-wave flux across the EBEX spectrum.

Though our flight data have not yet been analyzed, we present here an order of magnitude estimate of anticipated results from the planet scan. We take the approximate mean of Moreno's model and the Archeops data to assume band-averaged brightness temperatures of 150, 140, and 160 K for the 150, 250, and 410 GHz bands, respectively. Accounting for beam dilution (angular diameter = 17") and assuming the mean optical efficiency for each wafer as reported in Sec. 4.1, we calculate the effective signal in thermodynamic units at ~10 mK (150 GHz), 1 mK (250 GHz), and 1 mK (410 GHz). Besides optical efficiency, the input with perhaps greatest uncertainty is the detector noise level; although we have no definitive analysis of in-flight bolometer noise at this point, an early ground-based investigation indicates it may be at a factor of ~2 above expectations. Hence we will assume for this exercise a noise level of twice our canonical values of $NET_{150,250,410}$ = 193, 399, 3077 μK/√Hz. Therefore, during a single beam crossing we would predict S/N measured in bolometers at 150, 250, and 410 GHz of ~ 10, 0.5, and 0.05, respectively. Integrating over multiple crossings could increase these by a factor of 2 or 3.

However, if we consider the possibility that our preliminary ground-based beam mapping results are robust, the prospects for detecting Saturn may be more dire. Assuming the mean FWHM derived for each channel in Sec. 4.4 (52', 27', and 18' for 150, 250 and 410 GHz, respectively), the planet signal would be further diluted by factors of ~ 70, 20, and 10 compared to the values used above assuming 8' beams. Inserting these numbers into our calculations, the expected signal remains highest in the 150 GHz channel but drops to S/N < 0.2. So although the outlook appears bleak as predicted by these first-order calculations, we have adopted values for a number of values based on marginal quantitative evidence and have made several assumptions rooted in very preliminary results from ground-based testing with limited sample sizes.

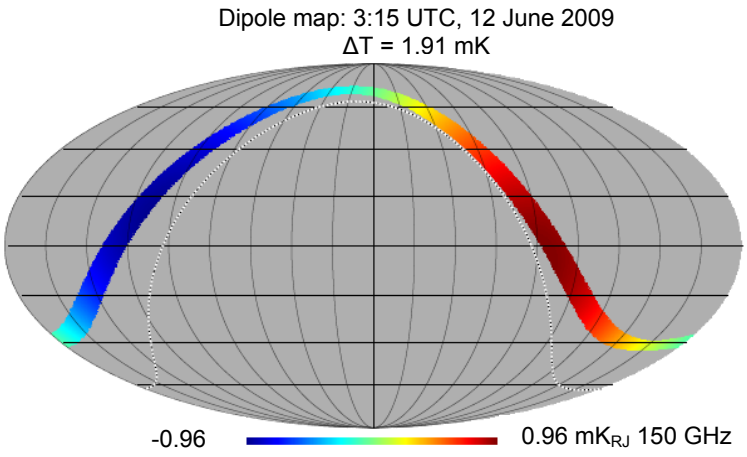

Figure 5.3: Simulated NA test flight CMB dipole scan coverage (Credit: Sam Leach, SISSA)

For the CMB dipole scan, the gondola was rotated in azimuth at 15˚/sec for 23 minutes beginning at UTC 2:53 and ending at 3:16. Given the orientation of the sky and the gondola's elevation angle, we expect the dipole to be a sinusoidal signal with a period of 24 seconds ($f \sim 40$ mHz) and amplitude of ~ 2 mK (at 150 GHz) as illustrated in Fig. 5.3. We can again make a rough assessment of anticipated results, subscribing to the same assumptions listed above which are applicable to this calculation (optical efficiency and bolometer noise). With 23 minutes of integration and an optical efficiency of ~5%, we expect S/N ~ 10 in the 150 GHz channel. However, this result almost certainly includes an optimistic value for bolometer noise; at 40 mHz, the signal will likely reside below the 1/f knee for which currently have no quantitative assessment but anticipate at around 100 mHz. Hence, the effective noise level may be equivalent to or perhaps even exceed the dipole signal. Barring a gross underestimate of optical efficiency or overestimate of noise, the prospect of extracting the dipole signal in any channel seemingly represents a significant analytical challenge.

5.2 Ebert-Fastie Monochromator: Future Work

5.2.1 Modified Design Concept

As chronicled in Sec. 4.5, the manual optical alignment procedure required to execute the cryogenic relative spectral response experiment is an inexact and time-consuming endeavor.

Even using the most optimistic assumptions calibrating the entire focal plane would likely take on the order of 200 hours. This almost certainly renders the cryogenic approach unreasonable given the probable LDB pre-flight campaign schedule. Hence we must consider (a) speeding up both the alignment and data collection procedures through automation, (b) assuming consistent spectral response across many neighboring bolometers and only calibrate one or a few per wafer, and/or (c) abandoning the cryogenic version of the experiment entirely.

Given the Ft Sumner experience, we propose a combination of these 3 options. Pending a definitive criterion on spectral response calibration, option (b) seems nominally supported by results presented in section 4.5 which show relatively consistent spectral response curves across four different 410 GHz bolometers at locations spanning virtually the entire spatial extent of the wafer. As for option (c), we recommend designating the integrated technique as our new baseline plan - assuming the gondola in 'staring' mode, we estimate that the entire focal plane could be calibrated in ~20 hours (easily accomplished during a single fridge cycle). This could drop to ~15 hours in the scanning mode, but the additional anticipated analytical complexity associated with this approach probably outweighs the marginal temporal gain. We also hesitate to entirely eliminate the cryogenic approach due to the apparent (and heretofore unresolved) 30 GHz shift seen in the Ft Sumner data. If the campaign schedule allows, initial results for at least one detector per wafer should be determined with an upgraded cryogenic apparatus before probing the full focal planes with the EFM on AP. A judicious insertion of stepper motors and/or linear actuators (grating, fold mirror, translation stage, etc.) could greatly enhance the sophistication and efficiency of the cryostat-based experiment.

As stated previously, the integrated EFM apparatus used in Ft Sumner was assembled on a short timeline and far from optimized. Although the experiment seemed to deliver sufficient S/N, only the 410 GHz wafer was tested and making an effort to upgrade the system would seem prudent to ensure success across all bands during future implementation. Amongst several possible ways identified to improve the experiment, one stands out: move the EFM exit aperture forward 14 cm to coincide with the focal point of the AP. Based on the analysis summarized in Fig. 4.18, with this single design modification we would expect to reduce beam dilution (and potentially increase S/N) by a factor of ~20. However, this assumes retaining the 1300 K laboratory blackbody as the warm load which is only possible with a modified mechanical design or by procuring a more compact blackbody source. While the latter would be preferred for simplicity, a very preliminary conceptual design using only the currently available hardware is provided in Fig. 5.4.

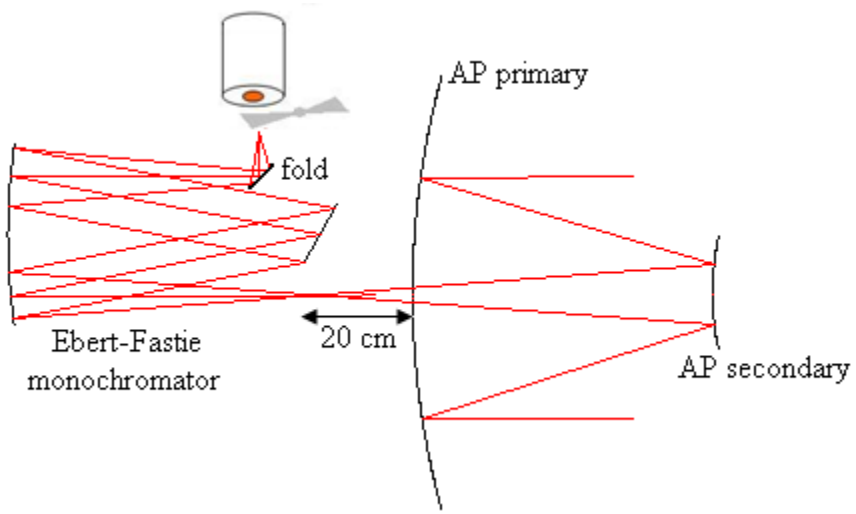

Figure 5.4: Preliminary conceptual design for upgraded EFM on AP. Fold mirror added just inside entrance aperture allows blackbody source to be rotated 90˚ from previous configuration. This change allows EFM exit aperture to coincide with AP focal plane at 20 cm behind primary mirror.

5.2.2 Relative Flux Calibration

The EFM relative flux model is a critical ingredient for making an accurate determination of relative spectral response for the LDB instrument, but our current model is largely theoretical and relies heavily on assumptions about grating efficiency which are far from robust. One option for rectifying the situation is to make more rigorous and reliable theoretical predictions. Given the simplicity of our monochromator, we assume grating efficiency is the dominant source of uncertainty in our current model. Sophisticated (and expensive) software packages are commercially available for predicting diffraction grating efficiency to high accuracy, including PC Grate and GSolver amongst others. We would of course also have to assume we know the emission characteristics of our modulated source to high accuracy. Given the fact we rely on a laboratory blackbody source with a temperature reading provided by the control unit (and any uncertainty introduced by imperfect knowledge of the cold load will be subdominant), it seems that the uncertainty contributed by this part of the apparatus would be primarily due to alignment issues which we suspect could be well-controlled with minimal effort. The idea requires further thought, but perhaps we could justify employing a relative flux model derived through an exclusively theoretical approach.

A second option – stand-alone or complimentary to the first - is to measure the emission spectrum empirically. This requires directing the monochromator beam onto a mm-wave detector

with flat spectral response, thereby isolating relative flux as a function of frequency. An effort to erect such a detector began in the spring of 2007. After a year we abandoned the initial plan to use a 4.2 K Haller-Beeman bolometer once it was conclusively determined that its performance was woefully insufficient for our intended experiment. Our present plan centers around using a single MAXIPOL bolometer mounted inside a reconfigured MAXIPOL cryostat.

The MAXIMA/MAXIPOL NTD-Ge bolometers are coupled to a 4mm diameter spiderweb absorber and were nominally operated at ~100mK with an adiabatic demagnetization refrigerator (ADR) [28]. After inspecting the interior of the MAXIPOL cryostat we favored the idea of coupling our bolometer to the 300 mK ^{3}He fridge instead of attempting to revive the ADR. Before committing to this approach we made an estimate of expected performance at 300 mK using the following assumptions and design parameters:

- *Bolometer properties*: $\Delta = 14.4$ K, $R_o = 120\ \Omega$, $G_{300mK} = 630$ pW/K [41].
- *Optical filtering*: 100% rejection above 540 GHz with MAXIPOL 18 cm^{-1} filter on the 4 K shell and a 55 cm^{-1} filter on 77 K shell (we tentatively plan to install an additional 16 cm^{-1} filter on the 4K shell, but exclude it in the present analysis).
- *Optical coupling*: the bolometer is mounted at the exit aperture of an f/1.7 Winston cone and housed within a reflective, cylindrical integrating cavity.

With these parameters we predict the bolometer to operate at $R_{bolo} \sim 120\text{k}\Omega$ with $dR/dT \sim 1\ \Omega/\mu\text{K}$ and be photon-noise limited with $NEP \sim 1 \times 10^{-14}$ W/$\sqrt{\text{Hz}}$. Assuming the mean expected monochromator efficiency of 50% and 30% optical efficiency for the detector system (cryostat window to bolometer), and ideal coupling between the two, we expect S/N ≥ 100 in one second of integration across all bands. If we further assume another order of magnitude loss between predictions and measurements as seen in Ft Sumner, we still expect S/N > 10.

The integrating cavity is a critical component for ensuring frequency-independent response. The literature recommends a many-λ deep, reflective, cylindrical cavity to achieve this goal [52]. Ours is made of copper and at ½" long is > 5λ deep across wavelengths of interest. The second most important component regarding frequency response is the 300 K window – depending on choice of material and thickness the window could effectively act as an etalon, introducing frequency selection through constructive and destructive interference

from reflection at the two surfaces. We will suppress this effect by using a 40 μm thick (< 15λ at our shortest wavelength of interest) polypropylene window, the same one used in the last MAXIPOL flight. Fig. 5.5 depicts our current conceptual design for the experiment; the EFM beam is coupled to the MAXIPOL bolometer using the same optical elements – two UHMWPE lenses plus a 45˚ fold mirror - employed in the cryogenic tests performed in Ft Sumner.

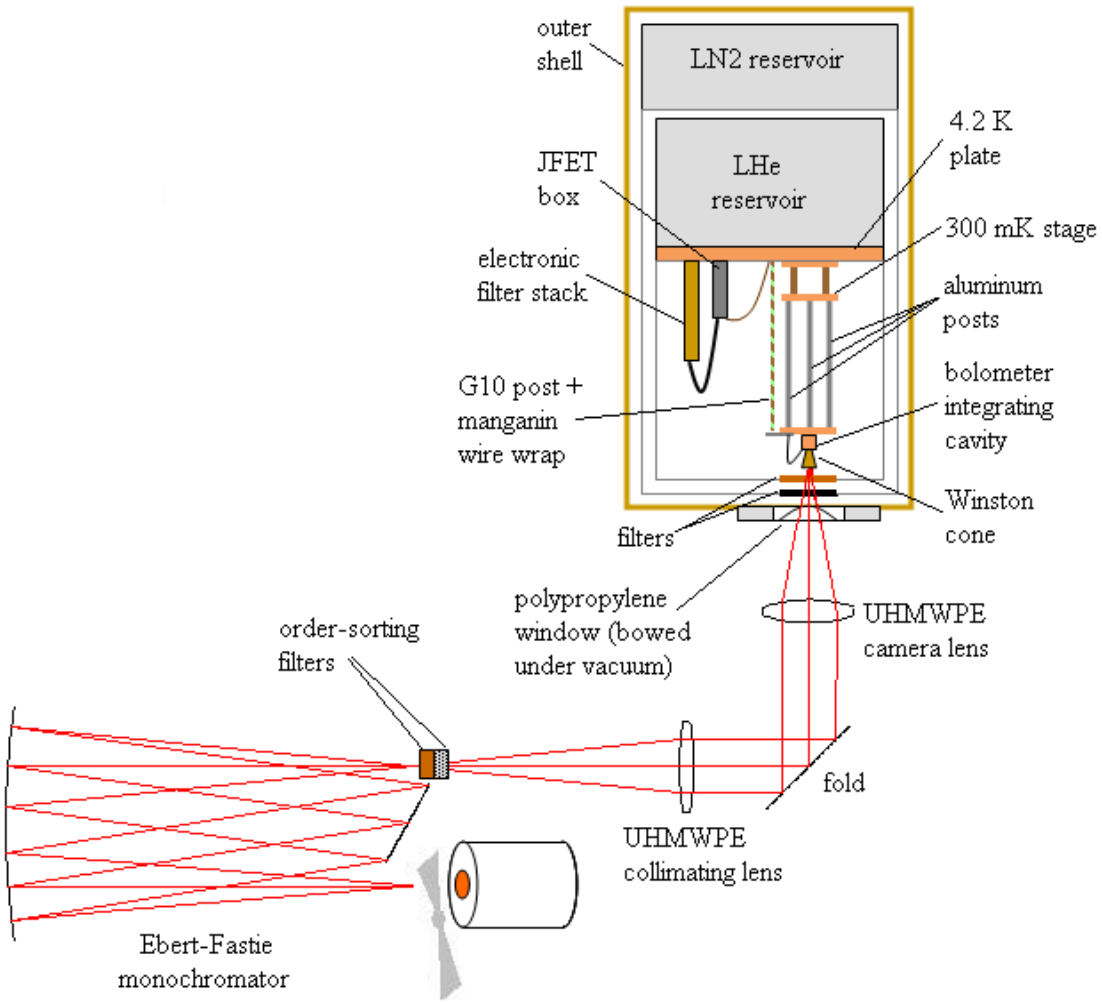

Figure 5.5: Conceptual drawing of the proposed EFM flux calibration experiment using the MAXIPOL cryostat.

We have removed a significant portion of the cryostat's internal components including the entire cryogenic optical system. We also replaced the MAXIPOL readout electronics with a simplified system since we will only be operating a single detector. As shown in the circuit

diagram in Fig. 5.6, we employ dual JFETs and a function generator to AC bias the bolometer. A lock-in amplifier will be used to extract the modulated EFM signal as a function of grating angle.

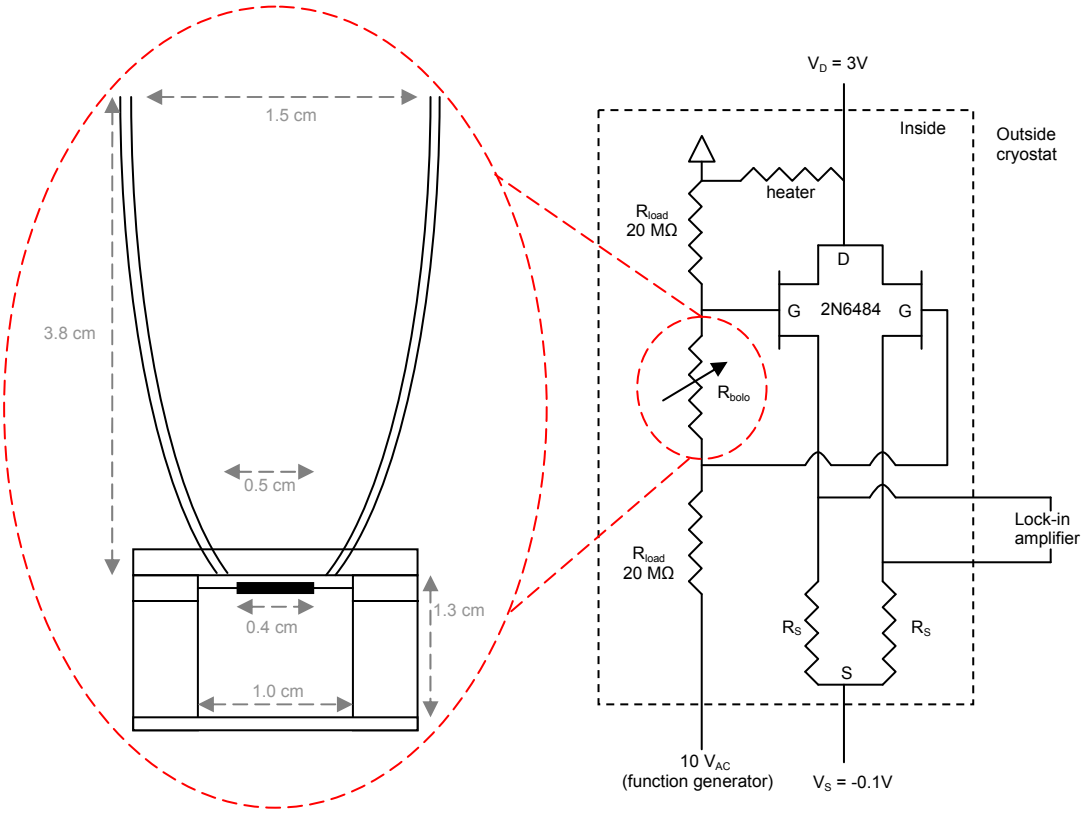

Figure 5.6: Key components of optical and electrical design for EFM flux calibration. Left - MAXIPOL bolometer (0.4 cm wide) mounted with Winston cone (above bolo) and integrating cavity (below bolo). Right: - Bias and readout circuit.

The most significant design challenge was spanning the distance between the 300 mK stage and the window – we need to place the Winston cone (and hence bolometer) within 3 inches of the window to avoid clipping the beam. This is accomplished with three solid aluminum posts, each 3/8" in diameter and ~13" long, which also serve as a thermal link between the bolometer platform and ^{3}He fridge. The only direct link between the 4.2 K cold plate and 300 mK stage are 6 readout wires leading from the filter stacks to the bolometer circuit. To minimize thermal load on the ^{3}He stage while trying to mitigate microphonic noise, we use 0.003" diameter manganin wire wrapped around a G10 tube (OD = 0.25", wall thickness = 0.0625") that is rigidly attached to the cold plate at one end and the bolometer platform at the other. Given the aforementioned dimensions, materials, and distances as shown in Fig. 5.5, we calculate the

combined thermal load on the 300 mK stage at < 10 μW (~ 9 μW from the G10 post, ~0.1 μW from the wiring). This is well within the allowable load according to the ^{3}He fridge specifications which predict over 3 days hold time under 106 μW with a condensation point at 4.2 K. Given that we anticipate completing the experiment in much less than 3 days, these data also imply that pumping on the LHe reservoir to achieve a condensation temperature of 2 K as originally planned should be unnecessary.

We have made a successful end-to-end test of the readout system at room temperature and atmospheric pressure. During our initial attempt to evacuate the cryostat we discovered a leak at the electrical feed-through flange. The indium seal on this flange is currently under repair and the experiment will proceed as planned once the leak has been fixed.

5.3 In-Flight Calibration

To this point we have focused exclusively on ground-based calibration except for a brief discussion in Sec. 5.1 regarding the NA test flight. However, our final determination of systematic effects will critically depend on data collected in-flight during the LDB mission. As Table 3.1 indicates, 7 of the 12 line items can be studied using flight data. For at least 5 of these 7, calibration derived from flight data will be the result we ultimately use in the final data analysis pipeline (far sidelobe response and bolometer time constants are typically measured more effectively on the ground).

For a more detailed discussion of the IP, DPR and APR experiments beyond the bullet statements found in Table 3.1, see reference [47]. Reference [53] provides a thorough explanation on determining time constants from glitches as demonstrated by Archeops; EBEX will likely employ a similar routine. Jupiter will serve as our primary calibrator for in-flight beam mapping; at an angular diameter of ~30” and average brightness temperature across our bands of 180 K, it will be a ~1 K point source (5x brighter than Saturn). Reference [52] states that Jupiter will also serve as our primary source for characterizing absolute flux response in the 410 GHz band. However, past observations (Fig. 5.7) indicate potential complications with this approach in light of our ±5% calibration criterion as they imply the planet’s flux is known to no greater accuracy than 10% over this portion of the electromagnetic spectrum.

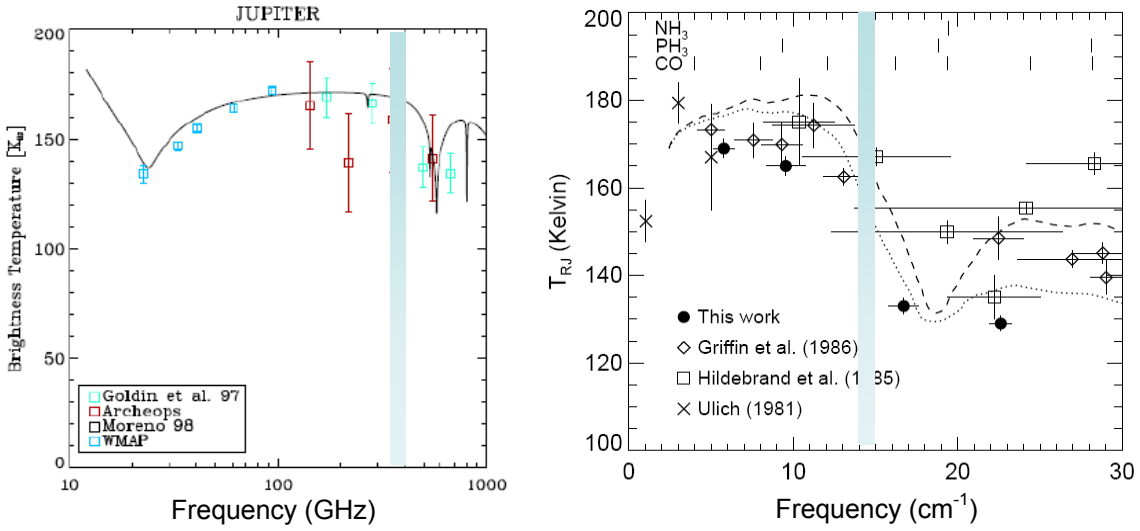

Figure 5.7: Jupiter mm- and sub-mm brightness temperature, data (points) and theory (lines). Left – Taken from [51], Archeops 345 GHz data is closest to EBEX 410 GHz band (shaded in blue) and indicates 15 % uncertainty (159 ± 24 K). Right – From [54]; solid and dashed lines represent two different atmospheric models which vary by ~10% at ~410 GHz. Both models are in turn calibrated on Mars, which varies seasonally by > 10% at WMAP frequencies [55].

Table 5.1 is an abridged historical record of sources used for balloon-borne mm-wave absolute flux response calibration. While 5% uncertainty has been attained repeatedly above λ = 1 mm using the dipole signal [56], no balloon-borne experiment to date has achieved this level of accuracy at frequencies above 300 GHz. The most promising candidate appears to be the Galaxy, scanned repeatedly and orthogonal to the plane by Archeops. The bolometer response from these scans was binned in latitude at -30˚ < l < 30˚ and calibrated with FIRAS maps after extrapolating the FIRAS spectra to Archeops frequencies. However, FIRAS spectra exist at 2-100 cm^{-1} which spans the entire Archeops (and EBEX) spectral range, so extrapolation would seem unnecessary. Individual FIRAS pixels reportedly measured the galactic plane at S/N ~ 50. If accurate, this 2% inherent uncertainty represents less than half the total 5% error budget and the galactic plane should hence be considered our primary target for EBEX absolute flux calibration (pending a deeper investigation of the FIRAS data).

Table 5.1: Recent historical precedent for balloon-borne mm-wave absolute flux calibration. EBEX calibration benchmark is ±5% in all bands.

Experiment	Frequency (GHz)	Calibrator	Comparator	Uncertainty
MAXIMA-I [59]	150 & 240	CMB dipole	COBE-FIRAS	4%
	420	Jupiter	Goldin '97 [54]	12%
Archeops [51,58]	143	CMB dipole	WMAP	4%
	217	CMB dipole	WMAP	8%
	353	Galactic plane	COBE-FIRAS	6%
	545	Galactic plane	COBE-FIRAS	6%
BOOMERanG [32]	145	TT spectrum	WMAP	2%
	245	TT spectrum	WMAP	5%
	345	TT spectrum	WMAP	9%

References

[1] E. Komatsu, J. Dunkley, M.R. Nolta, C.L. Bennett, B. Gold, G. Hinshaw, N. Jarosik, D. Larson, M. Limon, L. Page, D.N. Spergel, M. Halpern, R.S. Hill, A. Kogut, S.S. Meyer, G.S. Tucker, J.L. Weiland, E. Wollack, and E.L. Wright. Five-Year Wilkinson Microwave Anisotropy Probe Observations: Cosmological Interpretation. *Ap. J. Supp. Ser.*, 180:330-376, February 2009.

[2] M. Tegmark, D. Eisenstein, M. Strauss, D. Weinberg, M. Blanton, J. Frieman, M. Fukugita, J. Gunn, A. Hamilton, G. Knapp, R. Nichol, J. Ostriker, N. Padmanabhan, W. Percival, D. Schlegel, D. Schneider, R. Scoccimarro, U. Seljak, H. Seo, M. Swanson, A.Szalay, M. Vogeley, J. Yoo, I. Zehavi, K. Abazajian, S. Anderson, J, Annis, N, Bahcall, B. Bassett, A. Berlind, J. Brinkmannm, T. Budavari, F. Castander, A. Connolly, I. Csabai, M. Doi, D. Finkbeiner, B. Gillespie, K. Glazeborrk, G. Hennessy, D. Hogg, Z. Ivezic, B. Jain, D. Johnston, S. Kent, D. Lamb, B. Lee, H. Lin, J. Loveday, R. Lupton, J. Munn, K. Pan, C. Park, J. Peoples, J. Pier, A. Popoe, M. Richmond, C. Rockosi, R. Scranton, R. Sheth, A. Stebbins, C. Stoughton, I. Szapudi, D. Tucker, D. Vanden Berk, B. Yanny, and D. York. Cosmological Constraints from the SDSS Luminous Red Galaxies. *Phys Rev. D*., 74:123507, 2006.

[3] A. H. Guth. Inflationary universe: a possible solution to the horizon and flatness problems, *Phys. Rev. D*., 23:347-356, January 1981.

[4] A. D. Linde. A New Inflationary Universe Scenario: A Possible Solution of the Horizon, Flatness, Homogeneity, Isotropy and Primordial Monopole Problems. *Phys. Lett*., B108:389-393, 1982.

[5] A. Albrecht and P. J. Steinhardt. Cosmology for grand unified theories with radiatively induced symmetry breaking. *Phys. Rev. Lett*., 48:1220-1223, 1982.

[6] K. Sato. First-order phase transition of a vacuum and the expansion of the Universe. *MNRAS*, 195:467-479, May 1981.

[7] A. A. Starobinsky. Dynamic of Phase Transition in the New Inflationary Universe Scenario and Generation of Perturbations. *Phys. Lett.,* B117:175-178, 1982.

[8] A. A. Starobinsky. The Perturbation Spectrum Evolving from a Nonsingular Initially De-Sitter Cosmology and the Microwave Background Anisotropy. *Soviet Astronomy Letters*, r:302, June 1983.

[9] V. A. Rubakov, M. V. Sazhin, and A. V. Veryaskin. Graviton creation in the inflationary universe and the grand unification scale. *Phys. Lett. B*., 115:189-192, September 1982.

[10] L. P. Grishchuk. Amplification of gravitational waves in an isotropic universe. *Sov. Phys. JETP*, 40:409-415, 1975.

[11] L. F. Abbott and M. B. Wise. Constraints on generalized inflationary cosmologies. Nuclear *Physics B,* 244:541-548, October 1984.

[12] A. A. Penzias and R.W. Wilson. A Measurement of Excess Antenna Temperature at 4080 Mc/s. *Ap. J*., 142:419-421, July 1965.

[13] D. J. Fixsen, E.S. Cheng, J.M. Gales, J.C. Mather, R.A. Shafer, and E.L. Wright. The Cosmic Microwave Background Spectrum from the Full COBE FIRAS Data Set. *Ap. J.*, 473:576-587, December 1996.

[14] W. Hu and M. White. A CMB Polarization Primer. *New Astronomy*, 2:323-344, 1997. astro-ph/9706147

[15] M. Zaldarriaga and U. Seljak. All-sky analysis of polarization in the microwave background. *Phys. Rev. D.*, 55:1830-1840, 1997.

[16] U. Seljak. Measuring Polarization in the Cosmic Microwave Background. *Ap. J.*, 482:6-16, June 1997. Astro-ph/9608131.

[17] M. Zaldarriaga and U. Seljak. Gravitational lensing effect on cosmic microwave background polarization. *Phys. Rev. D.*, 58:23003, July 1998.

[18] D.N. Spergel, L. Verde, V. Peiris, E. Komatsu, M. R. Nolta, C. L. Bennett, M. Halpern, G. Hinshaw, N. Jarosik, A. Kogut, M. Limon, S. S. Meyer, L. Page, G. S. Tucker, J. L. Weiland, E. Wollack, and E. L. Wright. First-Year Wilkinson Microwave Anisotropy Probe (WMAP) Observations: Determination of Cosmological Parameters. *Ap. J. Suppl.*, 148:175-194, September 2003.

[19] M. Tegmark, M. Strauss, M. Blanton, K. Abazajian, S. Dodelson, H. Sandvik, X. Wang, D. Weinberg, I. Zehavi, N. Bahcall, F. Hoyle, D. Schlegel, R. Scoccimarro, M Vogeley, A. Berlind, T. Budavari, A. Connolly, D. Eisenstein, D. Finkbeiner, J. Frieman, J. Gunn, L. Hui, B. Jain, D. Johnston, S. Kent, H. Lin, R. Nakajima, R. Nichol, J. Ostriker, A. Pope, R. Scranton, U. Seljak, R. Sheth, A. Stebbins, A. Szalay, I. Szapudi, Y. Xu. Cosmological parameters from SDSS and WMAP. *ArXiv Astrophysics e-prints,* October 2003. Astro-ph/0310723.

[20] J. Bock, S. Church, M. Devlin, G. Hinshaw, A. Lange, A. Lee, L. Page, B. Partridge, J. Ruhl, M. Tegmark, P. Timbie, R. Weiss, B. Weinstein, and M. Zaldarriaga. Task force on cosmic microwave background research, 2006.

[21] L. Page, G. Hinshaw, E. Komatsu, M. R. Nolta, D. N. Spergel, C. L. Bennett, C. Barnes, R. Bean, O. Dore, J. Dunkley, M. Halpern, R. S. Hill, N. Jarosik, A. Kogut, M. Limon, S. S. Meyer, N. Odegard, H. V. Peiris, G. S. Tucker, L. Verde, J. L. Weiland, E. Wollack, and E. L. Wright. Three-Year Wilkinson Microwave Anisotropy Probe (WMAP) Observations: Polarization Analysis. *ArXiv Astrophysics e-prints*, March 2006.

[22] R. H. Hildebrand, J. A. Davidson, J. L. Dotson, C. D. Dowell, G. Novak, and J. E. Vaillancourt. A Primer on Far-Infrared Polarimetry. *Proc. Ast. Soc. Pac.*, 112:1215-1235, September, 200.

[23] T. J. Jones, D. Klebe. A simple infrared polarimeter. *Proc. Ast. Soc. Pac.*, 100:1158-116, September 1988.

[24] S. R. Platt, R. H. Hildebrand, R. J. Pernic, J. A. Davidson, and G. Novak. 100-micron array polarimetry from the Kuiper Airborne Observatory – Instrumentation, techniques, and first results. *Proc. Ast. Soc. Pac.*, 103:1193-1210, November 1991.

[25] B.R. Johnson, M.E. Abroe, P. Ade, J. Bock, J. Borrill, J.S. Collins, P. Ferreira, S. Hanany, A. H. Jaffe, T. Jones, A. T. Lee, L. Levinson, T. Matsumura, B. Rabii, T. Renbarger, P.L. Richards, G.F. Smoot, R. Stompor, H. T. Tran, and C. D. Winant. MAXIPOL: a balloon-borne experiment for measuring the polarization anisotropy of the cosmic microwave background radiation. *New Astronomy Review*, 47:1067-1075, December 2003. astro-ph/0308259.

[26] S. Hanany, J. Hubmayr, B. R. Johnson, T. Matsumura, P. Oxley, and M. Thibodeau. Millimeter-wave achromatic half-wave plate. *Appl. Opt*., 44:4666-4670, August 2005.

[27] J. R. Hull, S. Hanany, T. Matsumura, B. Johnson, and T. Jones. Characterization of a high-temperature superconducting bearing for use in a cosmic microwave background polarimeter. *Superconductor Science Technology*, 18:1, February 2005.

[28] S. Hanany, T. Matsumura, B. Johnson, T. Jones, J. R. Hull, and K. B. Ma. A cosmic microwave background radiation polarimeter using superconducting bearings. *IEEE Transactions on Applied Superconductivity,* 13:2128-2133, June 2003

[29] A. T. Lee, P. L. Richards, S. W. Nam, B. Cabrera, and K. D. Irwin. A Superconducting Bolometer with Strong Electrothermal Feedback. *Appl. Phys*. *Lett*., 69:1801-1803, September 1996.

[30] S. Lee, J. M. Gildemeister, W. Holmes, A. T. Lee, P. L. Richards. Voltage-Biased Superconducting Transition-Edge Bolometers with Strong Electrothermal Feedback Operated at 370 mK. *Appl. Opt*., 37: 3391-3397, June 1998.

[31] J. Hubmayr, F. Aubin, E. Bissonnette, M. Dobbs, S. Hanany, A. T. Lee, K. MacDermid, X. Meng, I. Sagiv, G. Smecher. Design and characterization of TES bolometers and SQUID readout electronics for a balloon-borne application. *Millimeter and Submillimeter Detectors and Instrumentation for Astronomy IV* Proceedings of SPIE, Vol 7020 eds. W. D. Duncan, W. S. Holland, S. Withington, J. Zmuidzinas 2008, arXiv:astro-ph/0908.1997.

[32] S. Masi, P. Ade, J. Bock, J. Bond, J. Borrill, A. Boscaleri, P. Cabella, C. Contaldi, B. Crill, P. de Bernardis, G. De Gasperis, A. de Oliveira-Costa, G. De Troia, G. Di Stefano, O. Ehlers, E. Hivon, V. Hristov, A. Iacoangeli, A. Jaffe, W. Jones, T. Kisner, A. Lange, C. MacTavish, C. Marini-Bettolo, P. Mason, P. Mauskopf, T. Montroy, F. Nati, L. Nati, P. Natoli, C. Netterfield, E. Pascale, E. Piacentini, D. Pogosyan, G. Polenta, S. Prunet, S. Ricciardi, G. Romeo, J. Ruhl, P. Sanitini, M. Tegmark, E. Trobet, M. Venziani, and N. Vittorio. Instrument, Method, Brightness and Polarization Maps form the 2003 flight of BOOMERanG. July 2005, astro-ph/0507509

[33] W. Fastie. A Small Plane Grating Monochromator. *Journal of the Optical Society of America*, 42:9:641-647.

[34] W. Fastie. Image Forming Properties of the Ebert Monochromator. *Journal of the Optical Society of America*, 42:9:647-651.

[35] C. Winnewisser, F. Lewen, J. Weinziert, H. Helm. Transmission features of frequency-selective components in the far infrared determined by terahertz time-domain spectroscopy. *Appl. Opt*., 38:18:3961-3967, 20 June 1999.

[36] A. Roberts, M. L. von Bibra, H-P. Gemund, and E. Kreysa. Thick grids with circular apertures: a comparison of theoretical and experimental performance. *Intl. Journ. Of Infrared and Millimeter Waves*, 15:3:505-517, 1994.

[37] K. M. van Vliet. Noise limitations in sold state photodetectors. *Appl. Opt*., 6:7:1145-1169, 1967.

[38] E. G. Loewen, M. Neviere, and D. Maystre. Grating efficiency theory as it applies to blazed and holographic gratings. *Appl. Opt*., 16:10:2711-2721.

[39] P. S. Kildal, E. Olsen, and J. A. Aas. Losses, Sidelobes, and Cross polarization caused by feed-support struts in reflector antennas: Design Curves. *IEEE Trans. On Ant. And Prop.*, 36:2:182-190, February 1988.

[40] E. Hecht. *Optics*. 1987.

[41] B. Johnson. MAXIPOL: A balloon-borne cosmic microwave background polarimeter. *PhD dissertation*, August 2004.

[42] J. Hubmayr. *PhD dissertation*. In progress, September 2009.

[43] J. W. Lamb. Miscellaneous data on materials for millimeter and submillimetre optics. *International Journal of Infrared and Millimeter Waves*., 17:12:1997-2034,1996

[44] C. Bao, EBEX North American test flight ground-based beam mapping, *EBEX internal memo*, in progress, September 2009.

[45] T. Matsumura. A Cosmic Microwave Background Radiation Polarimeter Using Superconducting Magnetic Bearings. *PhD dissertation*, September 2006.

[46] I. Sagiv. Analyzing EBEX polarization modulation efficiency. *EBEX internal memo*, in progress, September 2009.

[47] The E and B Experiment, proposal, April 2007.

[48] M. Milligan. Mueller Matrix Representations of Rotations in Observed Polarization Angle. *EBEX internal memo*, January 2009.

[49] C. Muckenhirn, S. Hanany, M. Milligan, D. Polsgrove. Polarization Rotation in the EBEX Optics. *Senior thesis*, May 2009.

[50] M. Milligan and A. Aboobaker.. EBEX Sidelobe Sensitivity. *EBEX internal memo*, May 2007.

[51] F.-X. Desert, J. F. Macias-Peres, F. Mayet, G. Giardino, C. Renault, J. Aumont, A. Benoit, J. Ph. Bernard, N. Pnthieu, and M. Tristram. Submillimetre point sources from the Archeops experiment: Very Cold Clumps in the Galactic Plane. *A&A*, February 2008. astro-ph/0801.4502v1

[52] D.A. Harper, R.H. Hildebrand, R. Stiening, and R. Winston. Heat trap: an optimized far infrared field optics system. *Appl. Opt*., 15:1:53-60, January 1976.

[53] J. F. Macias-Perez,….D. Yvon. Archeops in-flight performance, data processing, and map making. *A&A*, 467:1313-1344, 2007.

[54] A.B. Goldin, M.S. Kowitt, E.S. Cheng, D.A. Cottingham, D.J. Fixsen, C.A. Inman, S.S. Meyer, J.L. Puchalla, J.E. Ruhl, and R.F. Silverberg. Whole Disk Observations of Jupiter, Saturn and Mars in Millimeter/Submillimeter Bands. *Ap. J. Lett*., 488:L161-L164, 20 October 1997.

[55] R.S. Hill, J. L. Weiland, N. Odergard, E. Wollack, G. Hinshaw, D. Larson, C. L. Bennett, M. Halpern, L. Page, J. Dunkley, B. Gold, N. Jarosik, A. Kogut, M. Limon, M. R. Nolta, D. N. Spergel, G. S. Tucker, and E. L. Wright. Five-Year Wilkinson Microwave Anisotropy Probe (WMAP) Observations: Beam Maps and Window Functions. *Ap. J. S*., 180:246-264, 2009.

[56] B.Cappellini, D. Maino, G. Albetti, P. Platania, R. Paladini, A. Mennella, R. Bersanlli. Optimized in-flight absolute calibration for extended CMB surveys. *A & A*, 409:375-385, October 2003.

[57] D. Polsgrove, K. Zilic, J. Hubmayr. EBEX Microstrips: Theory, Fabrication and Results. *EBEX internal memo*, August 2008.

[58] J. Klein. Analyzing EBEX polarization rotation from ground-based calibration data. *EBEX internal memo*, in progress, September 2009.

[59] S. Hanany, P. Ade, A. Balbi, J. Bock, J. Borrill, A. Boscaleri, P. de Bernardis, P. G. Ferreira, V. V. Hristov, A. H. Jaffe, A. E. Lange, A. T. Lee, P. D. Mauskopf, C. B. Netterfield, S. Oh, E. Pascale, B. Rabii, P. L. Richards, G. F. Smoot, R. Stmpor, C. D. Winant, J. H. P. Wu. MAXIMA-I: A Measurement of the Cosmic Microwave Background Anisotropy on Angular Scales of 10' to 5˚. *Ap. J.*, 545:L5, 2000.

[60] H. Tran. EBEX Optics Introduction. *EBEX internal memo*.

[61] kst. http://kst.kde.org/.

[62] H. Johnson and M. Graham. *High-Speed Digital Design. A Handbook of Black Magic*. Prentice Hall, 1993.

Appendix A

EBEX Microstrips

We describe this subcomponent is detail because of its novelty and history of in-house development. Though contrived to meet demands unique to EBEX our microstrip design represents a significant improvement on existing *cold wiring* technologies and offers the potential for general application in a variety of cryogenic environments.

A.1 Motivation

Electrical communication between the TES bolometers and SQUIDs requires wiring with special thermal and electrical properties. Therefore we set out to develop a new wiring scheme with the goal of minimizing two primary characteristics: thermal conductance and inductance. Since the wiring must traverse a path between the ~300 mK (bolometers) and 4.2 K (SQUIDs), we sought materials and a design to more effectively mitigate load on the sub-Kelvin stages (a critical objective when requiring a 14-day hold time). Inductance in the wiring is mostly a function of geometry and adds to the inherent inductance of the system, potentially acting as a voltage divider on the SQUIDs and causing bolometer instability (as demonstrated with the conventional wiring). Therefore we will refer to the inductance of the cold wiring as *parasitic* inductance, or L_{para}. Our secondary objectives included achieving electrical crosstalk of < 1% between neighboring wires, which presents a peculiar challenge given the pre-existing geometric constraints inside the EBEX cryostat. A final consideration was fabrication feasibility as we endeavored to execute all aspects of research, development and manufacturing in-house.

A.2 Design

Assuming the current digital frequency multiplexing scheme (DfMUX), we anticipate needing 128 wire pairs (64 per focal plane) for reading out the full complement of 1,400+ bolometers during the LDB mission. With this sum in mind and considering the goals described in the previous section, we conducted a trade study of candidate wiring geometries.

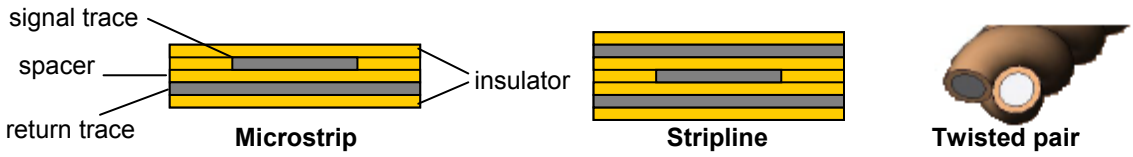

Figure A.1: Conceptual designs of 3 options considered in cold wiring trade study.

The three wiring options initially considered were the twisted pair, stripline, and microstrip, each illustrated in Fig. A.1. Though by far the easiest to make, previous experience with twisted pairs showed large parasitic inductance so this approach was eliminated early in the decision-making process (assuming a viable manufacturing procedure could be found for one or both of the other options). Striplines are expected to offer superior inductance mitigation but demand more material per unit length than microstrips, which correlates directly with higher thermal conductivity and fabrication complexity. The fabrication and thermal advantages of the microstrip were deemed more important than the marginal improvement on L_{para} expected of the stripline, hence microstrips were designated as the baseline plan. Further consideration including cryostat constraints determined the optimal microstrip configuration to include 8 *line pairs* per *unit*. The fully populated EBEX focal planes will thus require a total of 16 units; 8 serving the horizontal (H) focal plane that need to be ~27" long, and 8 for the vertical (V) focal plane at ~ 40" long. A set of analytical equations allows us to calculate the expected thermal conductance, parasitic inductance, and electrical crosstalk assuming our nominal design parameters as depicted in Fig. A.2.

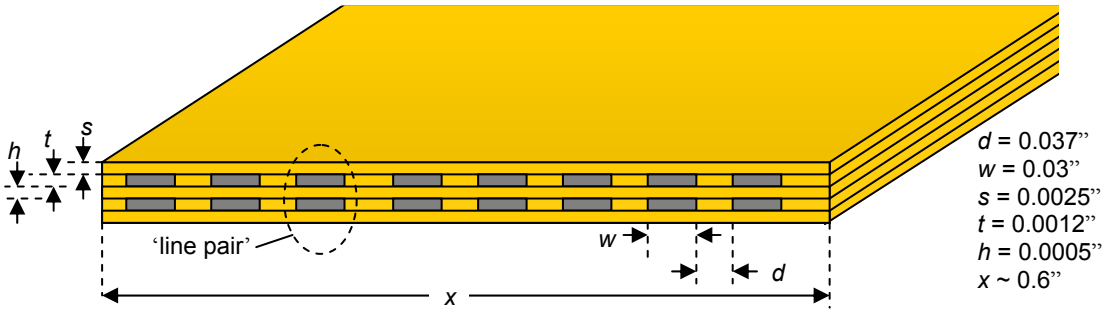

Figure A.2: Conceptual EBEX microstrip design. Yellow material (insulator and spacer) is kapton, grey material (wiring) is NbTi.

Thermal Conductance: Several different temperature stages are unavoidably thermally linked by the cold wiring inside the EBEX cryostat, each of which has a maximum thermal load tolerance. From low to high T, the stages (and maximum load) are ~250 mK (3 μW), ~400 mK (30 μW), ~1 K (200 μW), and 4.2 K where the cold wiring contribution is negligible compared to other inputs. With little room for adjusting the microstrip geometry due to physical constraints inside the cryostat, materials become a critical factor in achieving our thermal benchmarks. We insist the wires be superconducting at ≤ 4.2 K in order to eliminate additional thermal load due to electrical power dissipation. With a critical temperature (T_C) of 9 K and low thermal conductivity (0.03 x $T^{1.8}$ W/mK) in comparison to other metals with similar T_C, NbTi was chosen for the wiring. Kapton HN tape and film were chosen to serve as the insulator and spacer based on their similarly attractive thermal properties [k = 6.5 x 10^{-3} x T (W/mK)] and strong heritage of use in the cryogenic community

A large wire width to height ratio is optimal for minimizing parasitic inductance, but NbTi wire is only available commercially in cylindrical shape. We purchased cylindrical copper-cladded NbTi wire and had it flattened, specifying a width/height ratio of 40 (the copper cladding is necessary for soldering at the ends). After receiving the flattened wire, we measured width/height = .030"/.0012" = 25. Using these wire dimensions, the kapton dimensions as shown in Fig. A.2, and assuming the presence of 16 total microstrips as required for LDB gives total cross-sectional areas of 3.2 x 10^{-6} m^2 and 3.4 x 10^{-5} m^2 for NbTi and kapton, respectively. Including their reported thermal conductivities and the design distances between temperature stages inside the cryostat, we calculate the following expected thermal loads (per stage): 0.5 μW (250 mK), 7.2 μW (400 mK), and 38.5 μW (1 K). Each value represents approximately 20% of the maximum load, theoretically indicating the microstrip design satisfies our thermal constraints.

Parasitic Inductance: Johnson and Graham provide the following equations to predict inductance [62]:

$$w_{eff} = w + \frac{1.25t}{\pi}\left[1 + \ln\left(\frac{2h}{t}\right)\right] \tag{A.1}$$

$$L\left(\frac{nH}{inch}\right) = \frac{3.194\times10^{-8}}{\frac{w_{eff}}{h} + 1.393 + 0.667\ln\left(\frac{w_{eff}}{h} + 1.444\right)} \tag{A.2}$$

Using the dimensions listed in Fig. A.1, we find L = 0.5 nH/in or a total of 13.5 nH for a 27”-long H-plane unit. For comparison and to highlight the significance of this value, the original EBEX cold-wiring (based on the current industry standard) had a measured parasitic inductance over the same length of 133 nH. The original wiring, which we will call the *hybrid* geometry, consisted of two distinct parts - 20” of microstrip made with tin-soldered copper wires (L = 1.5 nH/in, measured) with a 5”-long section of twisted-pair NbTi in the middle for thermal isolation (L = 20 nH/in, measured). Our new all-NbTi microstrip therefore offers a theoretical order of magnitude improvement over the hybrid geometry.

Electrical Crosstalk: This term describes the coupling of signals between neighboring wires, a phenomenon that could problematically impact detector data read out (and ultimately science results) if not controlled to < 1%. Johnson and Graham offer the following formula to estimate this effect:

$$Crosstalk = \frac{K}{1+\left(\frac{d}{h}\right)^2} \tag{A.3}$$

where K is a geometrical factor reasonably assumed to be 1 in our case. Using *d* and *h* from Fig. A.2, the anticipated cross-talk is ~0.02%, well below the benchmark of 1%.

A.3 Fabrication

The manufacturing procedure is an entirely manual undertaking. From start to finish, a single unit currently takes ~3 hours to produce. This can be greatly reduced with multiple people performing steps in parallel, and could be further expedited if at some point demand were to warrant the capitol investment required to mechanize and automate the process.

The flattened copper-cladded NbTi wire is taken from its spool and cut into 16 pieces (8 signal traces, 8 return traces) of proper length (27” for the H focal plane or 40” for V). To minimize thermal conductivity, we must remove the copper cladding over the entire length except for ~1/2” at each end left behind for soldering. We dip each end in melted wax, then submerge the entire wire in a 70/30 solution of nitric acid. The acid eats away the copper everywhere except for at the ends where it is unable to penetrate the wax.

The first 8 wires are then aligned parallel to each other and at the proper spacing using a custom-built aluminum jig (see Fig. A.3). We discovered that the wires refuse to lay flat unless

forced to by other means, so we apply a thin layer of spray adhesive in 3 spots (both ends and one near the center) before laying the wires down. A 1-inch wide strip of kapton HN tape with acrylic adhesive is then rolled over top of the 8 wires, sticky side down. When pulled up, the wires stick to the tape (not the jig), maintaining their alignment and spacing. This first 'sub-strip' is placed to the side and the process is repeated with the other 8 wires.

With both sub-strips completed, one of them is laid on the bench with wires/adhesive side up. Experience revealed that the perimeter must be held down with masking tape to prevent rippling. Next, the 1.5"-wide kapton *spacer* is laid down, sticking to the kapton tape adhesive around and between the wires. Masking tape is again applied to prevent rippling, this time around the perimeter of the spacer material. The final and most challenging step is laying the second sub-strip (wires/acrylic facing down) on top of the spacer, making sure to align the wires of the 2nd sub-strip with those of the 1st sub-strip below.

The completed unit is removed from the bench and masking tape with a razor blade. Scissors are used to trim the unit to its final width of ~ 0.6" as necessary to accommodate its space allowance inside the cryostat. Finally, a blunt object (e.g., the end of a Sharpie marker as pictured in Fig. A.3) is pressed down over the length of each line pair in an attempt to eliminate remaining bubbles or rippling. This is done to minimize the separation between signal and return traces (h). h is directly related to parasitic inductance and a noticeable reduction in L was observed after adding this step to the procedure.

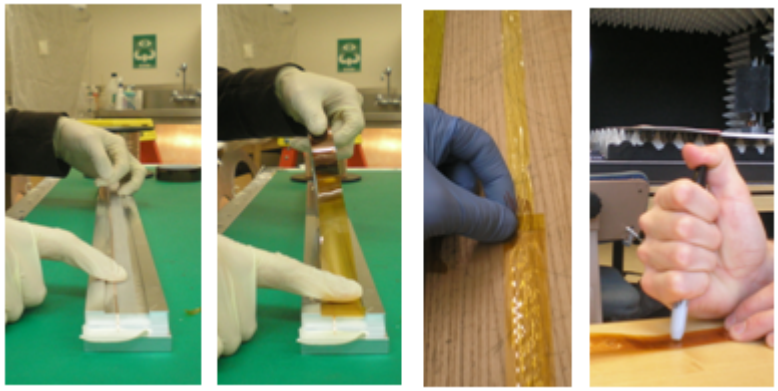

Figure A.3: Selected steps in microstrip fabrication procedure. From left to right: Laying wires on aluminum jig to aid alignment, kapton tape applied to wires aligned on jig, fastening *sub-strip* to workbench, compressing line pairs to minimize h (lower $L_{parasitic}$).

A.4 Characterization

Cryogenic Cycling: Since the microstrips will have to endure repeated cryogenic cycling when in the EBEX cryostat, we cryogenically cycled several test units to probe the effects of temperature on physical survival. In the first test we dunked microstrips directly into liquid nitrogen, which consistently caused the kapton layers to delaminate catastrophically. Direct exposure to the LN_2 plus near-instantaneous change from 300K to 77K were concluded as primary reasons for the failure and motivated minor design modifications, but caused little genuine concern as this test represents a significant departure from the actual cycling mode the microstrips will be expected to withstand (300K to 4.2K over several days). Another 300-77K cycle was performed but on a more reasonable timescale: a unit was attached to an aluminum block which was mounted inside a small vacuum chamber with an aluminum base plate. After pumping the chamber to < 1 Torr, it was submerged LN_2 which cooled the microstrip to 77K over a period of about an hour. This test was repeated four times and the microstrip showed no evidence of structural damage.

Two units were then mounted inside a small liquid helium test dewar. They were cycled from 300K to ~ 5K three times; after each cycle the dewar was opened for inspection and at no time was there any sign of mechanical failure. Finally, several units have been installed in the EBEX cryostat since July 2008 and used as intended to electrically link the bolometers with SQUIDs. The detectors have operated nominally over 4 cycles since that time, implying no structural problems with the microstrips.

Thermal Conductance: We have not performed a dedicated experiment to measure thermal conductance, nor identified a method to extract this information from data collected with the microstrips inside the EBEX cryostat. It is difficult or impossible to arrange temperature sensors in such a way to explicitly measure thermal conductance inside the cryostat due to their mounting scheme. Within the accuracy to which we have been able to determine the total load on each temperature stage, we see no evidence of excess loading due to the inter-stage linkage provided by the microstrips beyond the predicted theoretical values. We therefore conclude they perform within expectations and satisfy our thermal requirements.

Warm Inductance: An SRS720 LCR meter is used to measure the capacitance of line pairs at room temperature. Knowing C, L can be calculated with

$$L = \frac{d^2 \mu_0 \varepsilon_0 \varepsilon_r}{C} \tag{A.3}$$

where d is the length of the unit and ε_r is the dielectric constant of the spacer material (=3.5 for kapton HN) [57]. A total of 10 units were manufactured and measured between June 2008 and March 2009, with warm inductance calculated for each line pair. The last (and best) unit produced has a measured average inductance of 1.5 nH/in, three times greater than the theoretically predicted 0.5 nH/in. Fig. A.4 recaps the measurements, presenting the data in both graphical and tabular form to best illustrate the variance observed in the 8 line pairs within each unit. The inconsistency between theory and measurements, along with the minor but non-negligible inconsistency seen amongst line pairs of the same unit, highlights a primary consequence of manual production – the assembly process is clearly more an art than a science. However, a measured inductance of 1.5 nH/in gives a total inductance of 40 nH over 27". While not an order of magnitude improvement as predicted, this nevertheless represents a 3x improvement over that measured for the hybrid design.

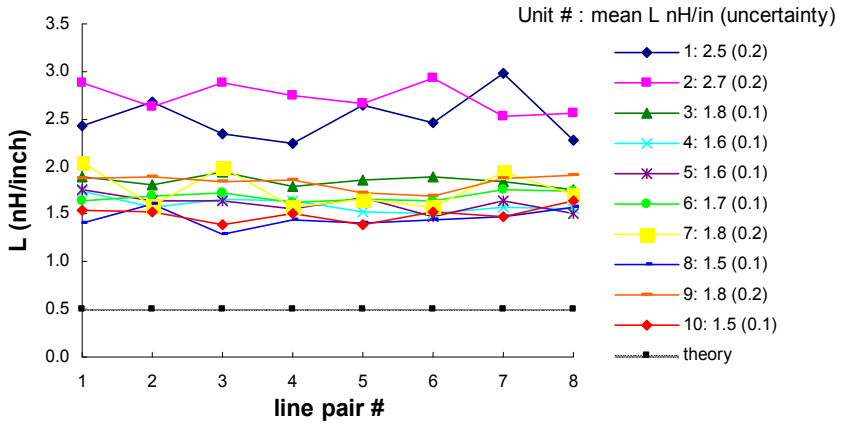

Figure A.4: Warm inductance measurements.

Cold Inductance, Test Dewar: To investigate inductance as a function of temperature and to assess performance in a more representative thermal environment, two line pairs on a single test unit were wired up inside the same liquid helium dewar used for the 5K cryogenic cycling described in the previous section. The LCR meter was used on the outside to measure capacitance at 300 K, and then again after thermalizing at 77 K and 5 K (temperatures confirmed

by SiO_2 diodes coupled to the unit). Results are shown in Table A.1 and indicate a decrease in L with T on the order of ~10% between 300 K and 5 K. Though a quantitative prediction for this behavior doesn't exist, the change happens in the expected direction – spacer contraction at low T likely decreases the trace separation (h), thereby increasing C and reducing L.

Table A.1: Cold inductance measurements, 5K test dewar. Additional inductance from wiring between interior and exterior of the cryostat has been subtracted.

	line pair #1	line pair #2
T (K)	L (nH, total)	L (nH, total)
300	53.1	64.9
77	49.8	56.2
5	49.0	55.0

Cold Inductance, EBEX Cryostat: Fig. A.5 shows the final configuration of a microstrip unit prior to being installed in the EBEX cryostat. Connectors are soldered to the copper leads at each end, one for the LC board and the other for the SQUID board. The first set of microstrips were installed in July 2008 and measured for parasitic inductance during the subsequent cryostat run.

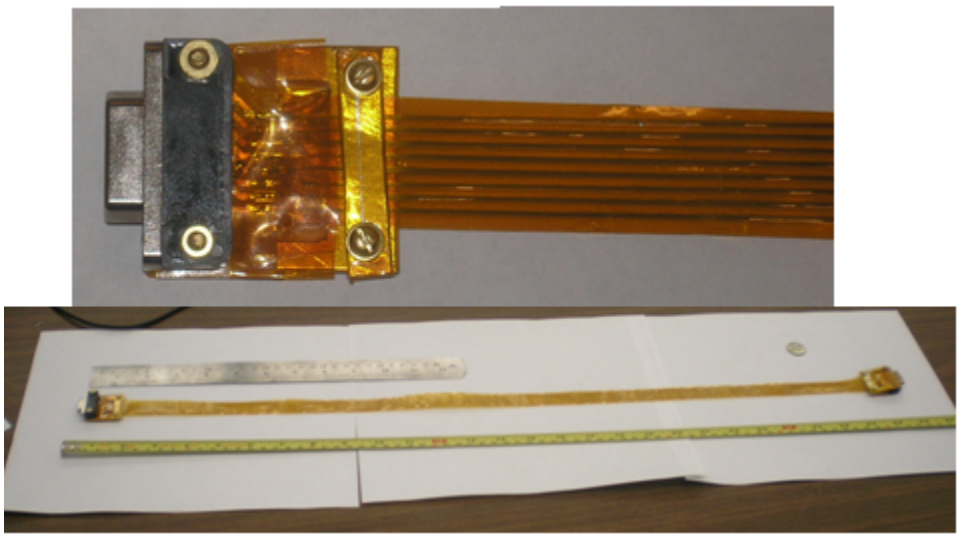

Figure A.5: Final configuration prior to installation in EBEX cryostat. End connectors are soldered to the small bit of copper sheathing exposed at each end of wires.

The measurements and analysis used to determine L_{para} in this configuration are significantly more complex than those already described [57]. Hubmayr's method uses data from bolometer DfMUX network analyses and searches for a best fit model that considers several free parameters including L_{para}. He analyzed three line pairs and reports the best-fit values (total L) are 50, 60, and 70 nH. These likely include ~15 nH contributed by other components in series with the microstrips in the circuit, and are consistent with warm measurements recorded prior to installation. These results reconfirm the same 3x improvement identified in previous experiments, this time measured in the microstrips' true operational environment.

Appendix B

The EBEX Collaboration

Shaul Hanany[1], Asad Aboobaker[1], Chaoyun Bao[1], Hannes Hubmayr[1], Terry Jones[1], Jeff Klein[1], Michael Milligan[1], Dan Polsgrove[1], Ilan Sagiv[1], Kate Raach[1], Kyle Zilic[1], Radek Stompor[2], Julian Borrill[3], Christopher Cantalupo[3], Ted Kisner[3], Federico Stivoli[3], Andrei Korotkov[4], Greg Tucker[4], Yuri Vinokurov[4], Tomotake Matsumura[5], Daniel Chapman[6], Joy Didier[6], Seth Hillbrand[6], Amber Miller[6], Britt Reichborn-Kjennerud[6], Nicolas Ponthieu[7], Julien Grain[7], Matias Zaldarriaga[8], Amit Yadav[8], Peter Ade[9], Will Grainger[9], Enzo Pascale[9], Andrew Jaffe[10], Matthieu Tristram[11], Francois Aubin[12], Matt Dobbs[12], Kevin MacDermid[12], Graeme Smecher[12], Gene Hilton[13], Kent Irwin[13], Carl Reintsema[13], Carlo Baccigalupi[14], Sam Leach[14], Brad Johnson[15], Adrian Lee[15], Xiaofan Meng[15], Huan Tran[15], Lorne Levinson[16]

[1]University of Minnesota, Twin Cities, [2]APC-Paris, [3]Berkeley Lab, [4]Brown University, [5]Cal Tech, [6]Columbia University, [7]IAS – Orsay, [8]IAS – Princeton, [9]Cardiff University, [10]Imperial College, [11]LAL – Orsay, [12]McGill University, [13]NIST, [14]SISSA – Trieste, [15]University of California, Berkeley, [16] Weizmann Institute of Science